# LAWRENCE TECHNOLOGICAL UNIVERSITY

A. Leon Linton Department of Mechanical Engineering

**Optimization of Process Parameters on a Selective Laser Sintering System for Improved Part Quality**

Presented in partial fulfillment of the requirements for the degree of

**Doctor of Engineering in Manufacturing Systems (DEMS)**

by

**Abass Maitham Jabber Al-Enzi**

**DEMS Committee**

Dr. James A. Mynderse, Academic Advisor, Mechanical Engineering
Dr. Chris Riedel, Mechanical Engineering
Dr. Vernon Fernandez, Mechanical Engineering
Dr. Nabih Jaber, Electrical and Computer Engineering

**December 19, 2017**

LAWRENCE TECHNOLOGICAL UNIVERSITY

A. Leon Linton Department of Mechanical Engineering

**Optimization of Process Parameters on a Selective Laser Sintering System for Improved Part Quality**

submitted in partial fulfillment of the requirements for the degree of

**Doctor of Engineering in Manufacturing Systems (DEMS)**

This dissertation has been reviewed and accepted by the examination committee.

| **DEMS Committee** | **Signature** |
|---|---|
| Dr. James A. Mynderse (advisor) | |
| Dr. Vernon Fernandez | |
| Dr. Nabih Jaber | |
| Dr. Chris Riedel | |

Approved by: _____ 1/4/2018
Program Director (mm/dd/yyyy)

Approved by: _____ 1/4/2018
Department Chair (mm/dd/yyyy)

ME Thesis/Dissertation Acceptance
rev. Fall 2017

# ABSTRACT

Selective Laser Sintering (SLS) is an additive manufacturing technique that uses a high power laser to sinter or melt powder, layer by layer, to build 3D shapes. However, SLS-fabricated parts may suffer from porosity, cracks, and poor surface roughness that degrade part quality. A prototype SLS system is presented for laboratory use in process parameter optimization to improve the SLS manufacturing process.

The prototype SLS system was designed and built by specifications determined previously. The first part designed and built was the laser positioning system that is used to hold the high power laser and the laser positioning system to work in the X and Y plane. The second part of the design was to calculate the laser power needed to melt the powder. Properties of powder were used to calculate the laser power. A small lens was used to focus the laser beam diameter from 4 mm to 0.42 mm on matching specifications of the prototype SLS system. The powder distribution system was the third part of the design used to distribute powder on a printing table in the X and Y plane and built by using simple components. The fourth section was the system frame, made from steel. The structure was used to contain the laser positioning system, the powder distribution system, and powder table. The fifth part was the electronic and control system: one microprocessor, four motor drivers, four stepper motors, and a heater table were used as subsystems to build the prototype SLS system. A manufacturing program was used to produce the system language and to control manufacturing parameters to create parts.

Operation of the prototype SLS system was validated against the design specifications. The validation included the laser positioning system movement, laser beam diameter, laser power, forward step, side step, system vibration, and system control. An interface

program with Arduino was used to check forward step and sidestep, and there was a small error found during the measuring process. The accelerometer was used to check vibration in the laser positioning system while running the system with different speeds. Also, a dial and indicator were used to measure runout on the thread bar of the laser positioning system in X and Y directions. Some types of sensors were used to measure laser power and laser beam diameter. These sensors cannot check high power lasers, so four filters were used to reduce the laser power. Encoder, MyRIO, and LabView programs were used to measure stepper motor speed. After the measuring process there was no deviation between speeds that fed the manufacturing program and speeds that were checked.

Finally, Response Surface Methodology was applied to build a regression model. Five variables at five levels were used in this research: forward step, side step, speed, platform temperature, and layer depth. These parameters were determined by doing some experiments in the prototype SLS system to determine which parameters will decrease or increase part defects. A total of 32 tests were used to determine mathematical models of SLS defects. A Genetic Algorithm method was used to determine the optimal solution to minimize crack width and surface roughness of the part. Results proved the manufacturing parameters affected crack width and surface roughness. The contour plot, interaction plot, and main effects plot were used to confirm and support the results.

# ACKNOWLEDGEMENTS

I would like to express my deep thankfulness to my advisor, Dr. James A. Mynderse. His personal guidance, perpetual energy, and enthusiasm encouraged me in many ways.

I want to thank Dr. Chris Riedel, Dr. Vernon Fernandez, and Dr. Nabih Jaber for serving on the Doctoral Committee.

I want to thank the support from MPG is greatly appreciated. I offer my regards to Sam Al-Ameer who supported me from the beginning of my research, and it is my pleasure to thank him. Also, I want to thank Dr. Changgong Zhou and Dr. Yawen Li for their support, time, and advice.

I want to thank my father , my moms, my sister, my brothers, my friends, HCED, my teachers in University of Technology/ Baghdad, and relatives. They are the source of my inspiration and therefore, I present this dissertation for them.

# TABLE OF CONTENTS

# LIST OF TABLES

# LIST OF FIGURES

# NOMENCLATURE

| | |
|---|---|
| $L$ | Layer thickness |
| $\theta$ | Surface angle of the surface |
| $\theta_s$ | Step angle |
| $\phi$ | Profile surface angle |
| D | Beam diameter |
| V | Scan speed |
| $\lambda$ | Conductivity coefficient |
| c | Heat capacity |
| t | Time |
| $T_l(z,t)$ | Temperature profile in a liquid |
| $T_s(z,t)$ | Temperature profile in a solid |
| $T_e$ | Environment temperature, |
| $T_0$ | Powder bed initial temperature |
| $T_{l0}(t)$ | Melting surface temperature |
| $T_w(t)$ | Surface temperature |
| $\rho$ | Density |
| $\rho_s$ | Density of a solid |
| h | Convection heat transfer coefficient |
| r1 | Beam radius |
| R | Radial distance from the center point |
| $r_0$ | Laser spot radius |

| | |
|---|---|
| $r_d$ | Radial distance |
| $R_f$ | Reflectivity of the solid |
| $\alpha$ | Absorption rate |
| $\alpha_S$ | Thermal diffusivity of the solid |
| $\alpha_l$ | Thermal diffusivity of the liquid |
| z | Vertical distance |
| $z_m(t)$ | Melting front location |
| $k_s$ | Thermal conductivity of the solid workpiece |
| u | Dummy variable for integrating |
| $L_m$ | Latent heat of melting |
| $t_m$ | Time required to initiate melting |
| $A_s$ | Absorptivity |
| $I_{abs}$ | Absorbed laser intensity |
| $I_0$ | Peak intensity |
| P | Laser power |
| I | Power density of the laser beam |
| $\delta_l(t)$ | Heat penetration depth in a liquid |
| $\delta_s(t)$ | Heat penetration depth in a solid |
| i | Gear ratio |
| PB | Shaft pitch |
| $A$ | Amplitude |
| $f$ | Frequency |
| Q | Intensity of line heat source |

# 1. INTRODUCTION

## 1.1 Additive Manufacturing

Additive manufacturing (AM) is a fabrication method that utilizes computer aided design (CAD) and specialized system hardware to build parts using layer-by-layer manufacturing. Solid freeform fabrication, digital manufacturing, direct manufacturing, or e-manufacturing are other names for AM. AM processes can create a complex 3D shape with different materials, reduced total manufacturing time, and reduced cost. Therefore, AM may enable a "third industrial revolution" [1, 2].

There are two classifications often used with AM: Rapid Prototyping (RP) and Rapid Manufacturing (RM). RP is a technique used to represent engineering patterns to check dimensions or as a model for engineers. However, these parts often lack the strength to serve. On the other hand, the parts produced by using RM can be used as final parts in mechanical or electrical systems. The quality of RM may be as good or better than parts produced by using traditional manufacturing [1, 2].

The significant difference between AM and Traditional Manufacturing (TM) that AM adds materials while TM subtracts during manufacturing processes. TM processes include cutting, machining, drilling, deep drawing, grinding, etc. This method is inherently wasteful because the process starts removing material from stock material to produce the final product. Often these basic parts are combined (or added) together to form a component or assembly through joining processes, such as fastening or welding. In contrast, parts made using AM processes consume only stock equivalent to their own mass and unused stock can be immediately used in other manufacturing processes. AM

technology can reduce total cost by reducing tooling and other costly manufacturing processes. Another advantage of this improvement is that it can produce shapes not possible with TM. This can lead to weight reduction and produce 3D complex shape [1, 2], see for example Figure 1 and Figure 2.

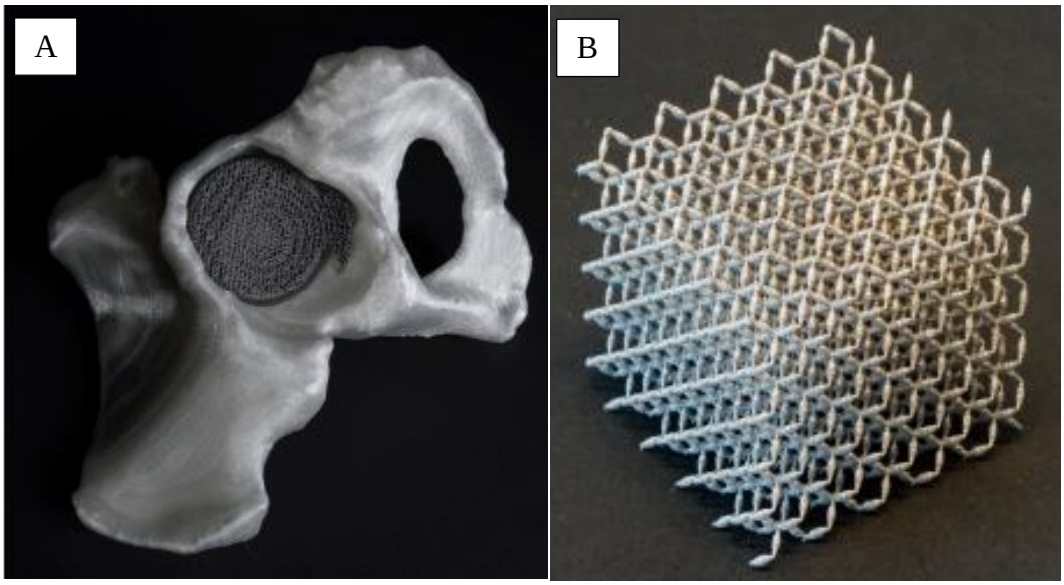


Figure 1. (A) Manufacturing patient-specific part by using SLS (B) Manufacture penta-model by using SLS technique [3]

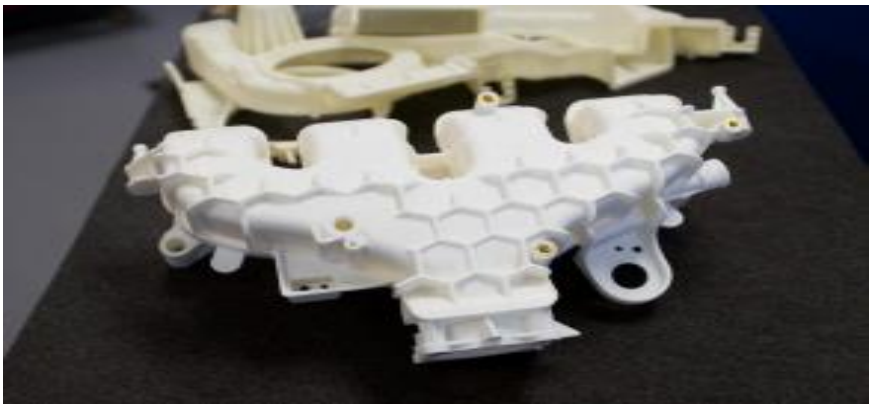

Figure 2. Complex ducting [4]

Manufacturing processes can be characterized in two ways: technological and economic. Mechanically, the manufacturing process produces parts by utilizing physical and chemical procedures. Traditional manufacturing process used to generate a 3D part has many manufacturing process steps (cutting, drilling, milling, grinding, and polishing). Figure 3 shows the process routing to achieve 3D parts. The manufacturing process often consists of a sequence of operations. Each step of the process routing conveys the raw material closer to the final part. Financially, the goal of manufacturing is to produce a 3D part with good quality. The important point of the manufacturing process is to increase the part quality and reduce a deviation that happens during manufacturing with low cost [5].

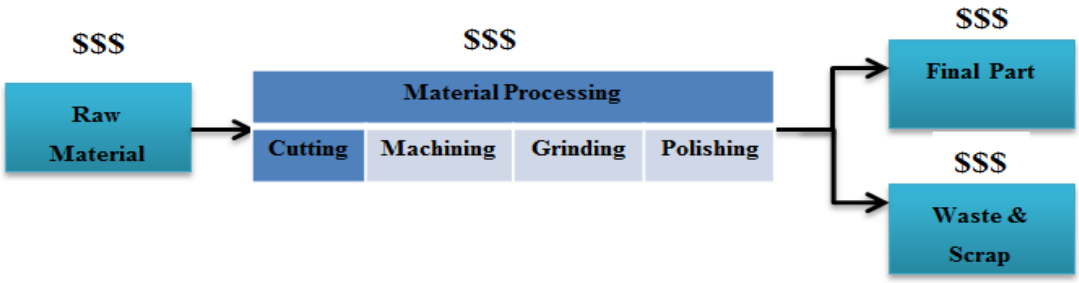


Figure 3. Technical and economic processes of manufacturing [5]

### 1.1.1 History of AM

Since the 1980s, AM started to be accessible to produce patterns. Researchers spent more than 20 years to develop the AM technique and use this method to manufacture parts in plants. The Ciraud patent in 1971 [6] used layer-by-layer method to 3D laser cladding. The Housholder patent in 1977 [7] proposed an SLS system to produce a 3D article by using a layers technique, but this work stopped due to limitations during that time, such as computer speed and high power laser. At the University of Texas at Austin

in 1986, Deckard built the first system named SLS. In 1990 Electro Optical Systems (EOS) produced a stereolithography system to provide a 3D part by using light resin [8]. Direct Metal Laser Sintering (DMLS) system was created in 1995 to produce a part by using plastic powder. In 2004 EOS GmbH started to build the SLS system. In 1997, AeroMet and MTS Systems Corp provided the Laser Additive Manufacturing (LAM) system, and this system used a high-power laser to print powdered titanium composites. In 1995, the Fraunhofer Institute for Laser Technology (ILT) in Aachen produced selective laser melting (SLM). Dr. Dieter Schwarze and Dr. Matthias Fockele worked with Dr. Wilhelm Meiners and Dr. Konrad from ILT on SLM. In 1997, Optomec built an AM system and laser system created at Sandia National Laboratories, and this system is used in 15 countries. In 2000, Fockele and Schwarze worked together with MCP HEK GmbH Germany. In 2007 MCP HEK Tooling GmbH produced advance SLM [1].

### 1.1.2 Advantages of AM Technology

AM technology is used to produce good 3D part quality regarding cost, speed, reliability, and accuracy. AM innovation, which has an intersection area with laser technology, materials science, and mechanical designing, is important in manufacturing fields to produce a simple or complex parts with fewer employees and tooling [9]. Rapid manufacturing in AM means it can produce a part regardless of the size, number, manufacturing time, and parts complexity. Therefore, AM can create emergency parts during a limited time for automotive parts, aerospace parts, submarine parts, and biomedical engineering parts. The idea of rapid is to create parts from powder, without a long time of manufacturing process or using many tools [10]. AM processes do not need many employees, equipment, and skills to produce the parts and that lead to reducing

manufacturing cost and process routing. Also, there are no side effects of AM on environments because the manufacturing process does not need chemical material like the manufacturing process in TM. Additive manufacturing does not need a die to produce parts. However, it is considered very fast to provide parts at low volume. Besides, the AM does not need tools, fixtures, machines, and dies while producing the parts. The advantages of using rapid manufacturing over conventional manufacturing processes, include [10, 11]: Reduce lead times, zero tooling costs, material flexibility, production of both simple and complex parts, high manufacturing speed, design flexibility, and non-polluting manufacturing process. Additive manufacturing disadvantages are material cost, surface roughness, shrinkage, porosity, and warping.

### 1.1.3 Types of AM

All AM types have the same concept to produce parts, but each type of AM has a particular manufacturing procedure regarding materials, handling methods, and appropriate circumstances. The ability to get metallic parts with good microstructural and mechanical properties by using AM depends on which process is used to manufacture parts. Figure 4 indicates the classifications of laser additive manufacturing, including SLS. The important AM innovation for the manufacture of metallic parts commonly has three major procedures: laser melting (LM), laser metal deposition (LMD), and laser sintering (LS) [1, 2].

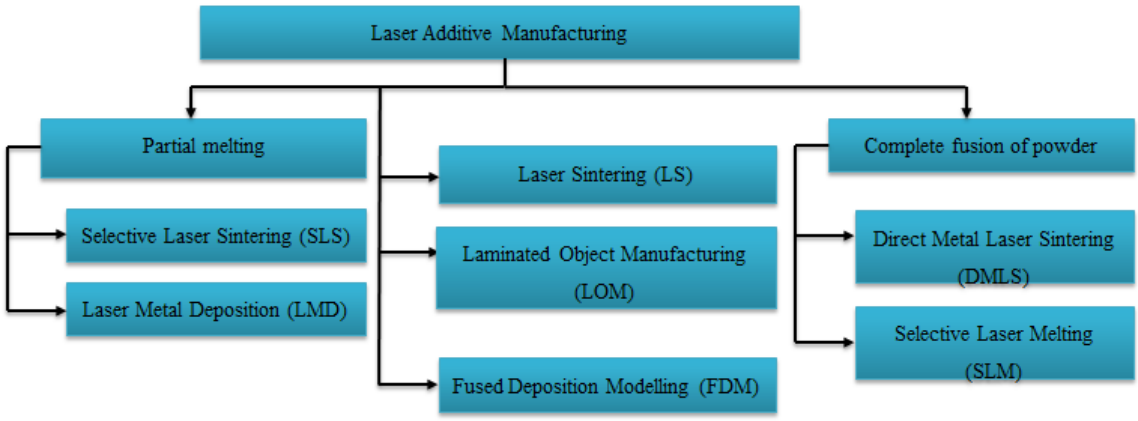


Figure 4. Laser additive manufacturing processes

#### 1.1.3.1 Laser Melting (LM)

LM has been developed to avoid a post-processing time and to create completely reliable parts with mechanical properties similar to bulk materials. The significant difference of LM is a complete melting/solidification of metallic powder. In recent years, developing laser systems helped to get full melting of the powder during the manufacturing process. The parameters that contributed to getting complete fusion are laser power, spot diameter, layer thickness, etc [12].

Simchi et al. have fused high speed steel by using full laser melting LM and SLS techniques separately. The densification rate, surface smoothness, and microstructural homogeneity of LM were better than SLS. Figure 5a shows part with full melting of powder by using LM method. The surface is smooth and does not have porosity. Figure 5b shows part without full melting of powder by using SLS method. The surface is not smooth, the grains is clear on surface, and the surface has porosity [1].

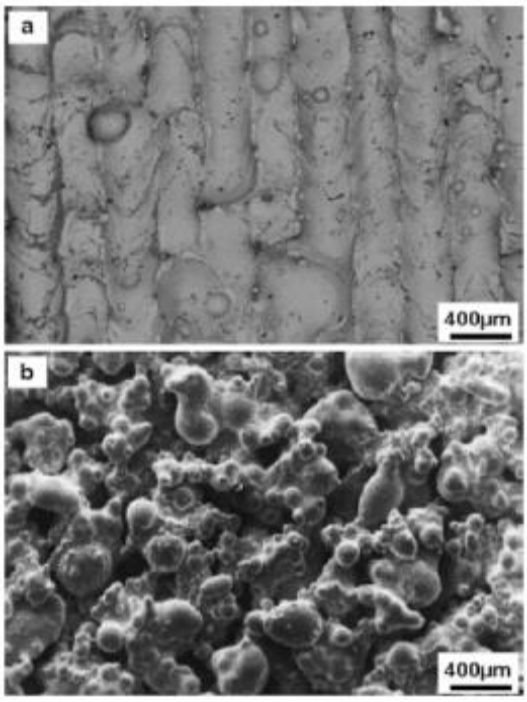


Figure 5. Surface morphologies of high speed steel components processed by (a) LM (b) SLS [1]

#### 1.1.3.2 Laser Metal Deposition (LMD)

LMD is another AM technique that has some differences compared with LS/LM. The major difference is the powder distribution mechanism, conveyed by using a gas and nozzles, see Figure 6. The melting process happens along with the z-axis layer by layer, so the high power laser transmits from the center point of the nozzle along the z-axis. The laser is focused by using a lens to the laser beam diameter calculated previously. The melting process changes if moving the lens or powder nozzle in the z-axis because that change will improve laser focusing. The 3D shape is created in XY plane; the workpiece table is controlled by using a PC. The LMD system can be used to coat, repair the parts, and manufacture parts that have a complex shape with dimensional precision [1, 13, 14, 15].

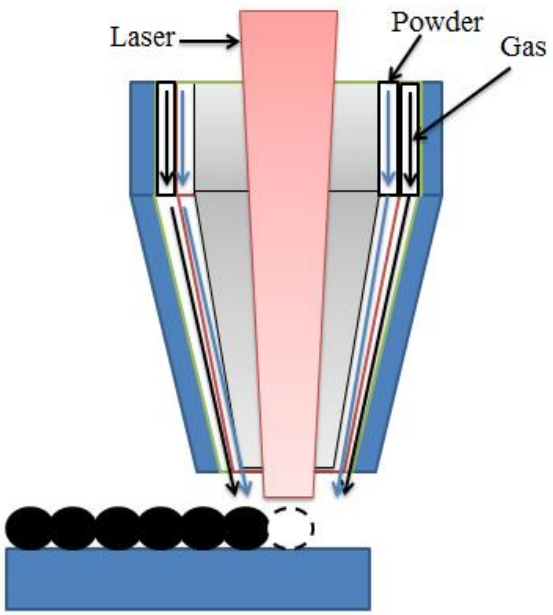


Figure 6. Manufacturing process of LMD

#### 1.1.3.3 Stereolithography (SL)

SL system was invented in the mid-1980s in the USA. Parts are made when a photocurable liquid resin is solidified after scanning a laser on the fluid, as shown in Figure 7. Also, the manufacturing process uses a CAD model and appropriate hardware to build the parts layer-by-layer method. The process is repeated until the part is completed [16].

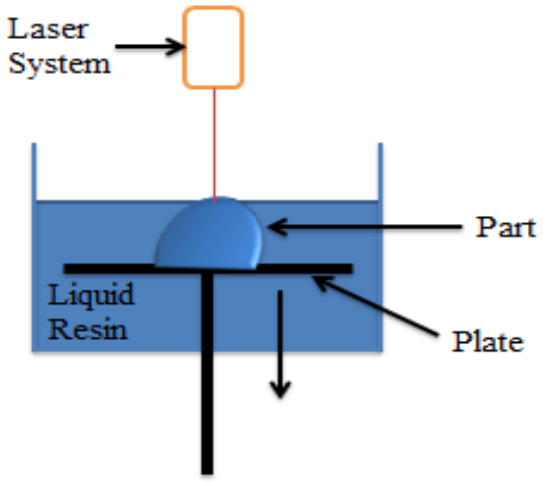


Figure 7. Manufacturing process of SL

#### 1.1.3.4 Laminated Object Manufacturing (LOM)

The LOM system can produce parts by using additive and subtractive operation. Adhesive materials are used to coat the plate. A laser follows a tool path to build a part by cutting the plate. The workpiece table moves down to feed a new plate. The new sheet feeds from a rotary and heated roller, so this process will repeat until the part is finished. See Figure 8 [16].

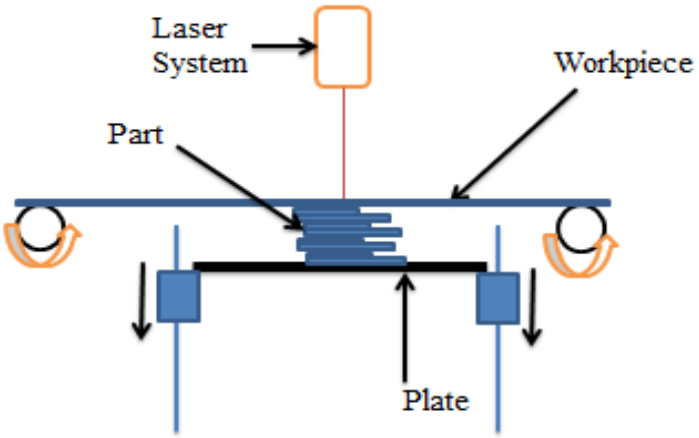


Figure 8. Manufacturing process of LOM

### 1.1.3.5 1.1.3.5 Fused Deposition Modelling (FDM)

FDM uses an extruder to melt and inject the filament from a small nozzle on the system table, see Figure 9. FSM works in three axes. Two of these axes control the X and Y planes and the third axis control the layering process. Parts are built by using the layer by layer method and an extruder will follow the tool path to complete building the part [16].

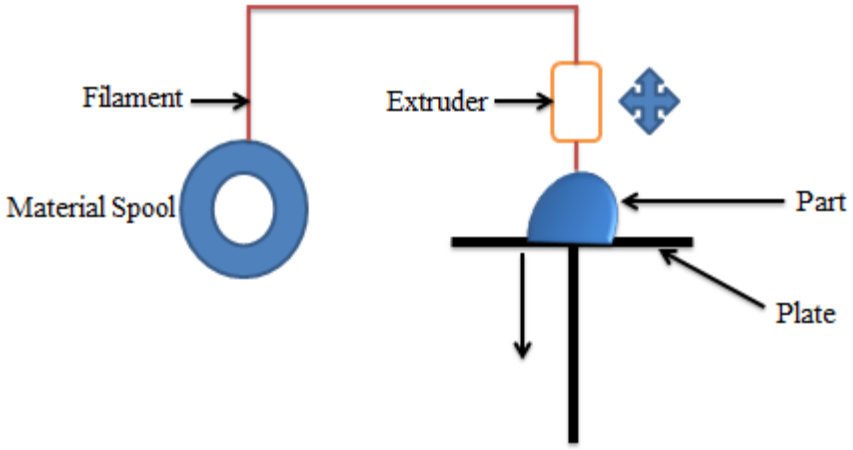


Figure 9. Manufacturing process of FDM

### 1.1.3.6 Selective laser sintering (SLS)

The SLS technique is an additive manufacturing technique. SLS fuses the powdered materials, without full melting, by scanning a laser on the powder bed. After the first layer is completed, the powder bed will move down in the z-axis direction. New powdered material is spread across the worksurface and the new layer will apply on top of the first layer. This allows each layer to fuse to the previous, making a solid part. The powder bed temperature is set lower than melting temperature to reduce part defects [13, 14, 15].

The powder used in SLS and some other AM techniques to generate parts may come from scrap recycling, shown in Figure 10. Parts are ground, then convert to powder. The powder is built into new parts that eventually turn into scrap. These steps are called waste recycling.

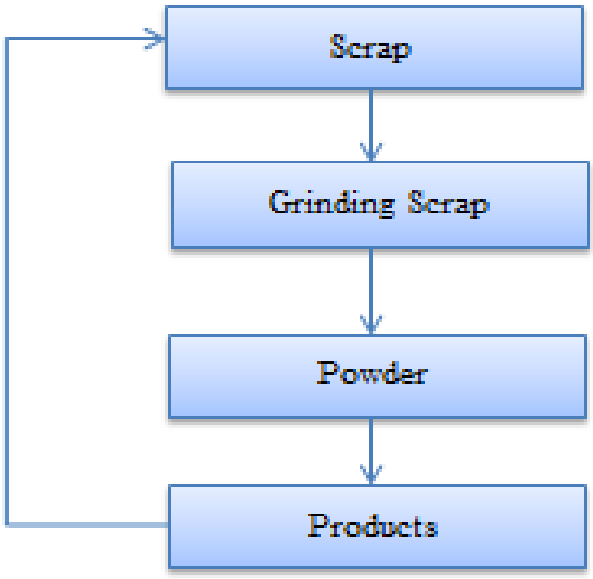


Figure 10. Scrap recycling process

Figure 11 shows the equipment and process of the SLS technique. It has a powder feeder mechanism that will move on the XY plane. The piston carries the powder bed and moves on the z-axis, and the laser will move on the XY plane. The printer control is an application that controls the printer processes. From this request, it will feed a slicing tool path to the printer, monitor the printer's axes and manufacturing parameters, and set the printer bed temperature. After these initialization steps, the printer starts to print the 3D part [17].

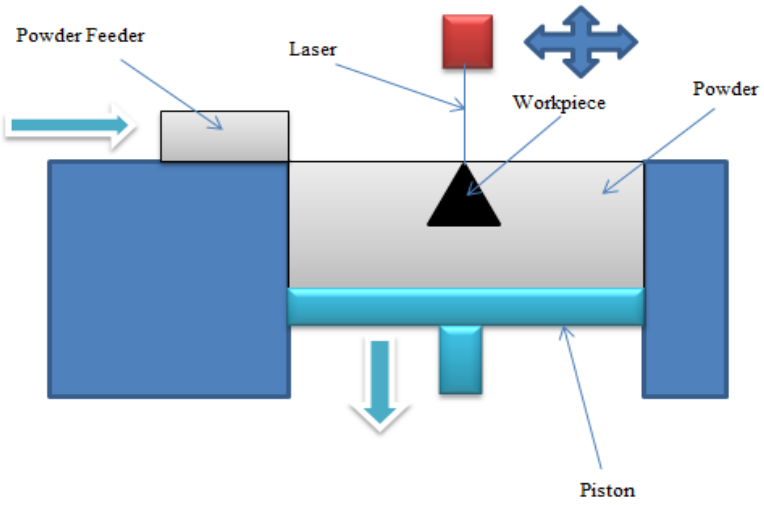


Figure 11. SLS process and equipment (side view)

The SLS controller communicates with actuators and a PC by using a program called firmware. The firmware controls the stepper motor and laser to build 3D objects after feeding the laser tool path from the CAM program. This means that the firmware is considered a link between CAM and SLS system. Also, the CAM program consists of temperature bed, axes movements, and other manufacturing information.

Different types of LS lasers are utilized to get different power that is used to melt powder. The reasons the laser affects the consolidation of powders are [1, 10]: The powder melting relies on the laser wavelength, and the powder metallurgical component is dictated by the laser energy that applies.

Powder properties should be checked before starting the melting process to understand the metallurgical mechanism for powder solidification and to get a melting process. Multi-components are mixed, high melting point materials combined with the low melting material. So, the high melting point is considered as the base of the part, and the low melting point is considered as the binder between grains [1, 2]. The temperature

required to melt the powder is determined by modifying laser parameters. Therefore, the binder melts totally during the printing process to hold the base powder to create the part [1].

## 1.2 SLS Manufacturing Procedures

The procedures produce a 3D part by using SLS techniques start from a CAD model of the 3D part. These procedures are shown as a flowchart in Figure 12. The first step of the manufacturing process is a part design by using CAD program. The second step is to change the CAD to an STL (STereoLithography) model. There are many manufacturing simulation programs used to convert a CAD to STL file of the 3D part. The third step is to slice the STL file into layers. In this section of the process the STL file will be ready to use for fabricating the 3D parts.

The fourth step is to build the part in a layer by layer method. The building process creates one layer for each step until part completion. The last step of the SLS manufacturing process is to clean the part. Sanding and painting are common methods used to treat the surface of the part. The point of post-processing is to enhance appearance and strength [2, 18].

*Layer thickness* is the real depth that prints or melts to build the first layer of a part. *Forward distance* is the distance of a manufacturing laser motion between two points in a front direction. *Sidestep distance* is the distance of a building laser motion between two points in a side direction. *The forward error* is a deviation between design and actual design surface. *Scallop height* is the real height left between two parallel lines of the manufacturing tool [19].

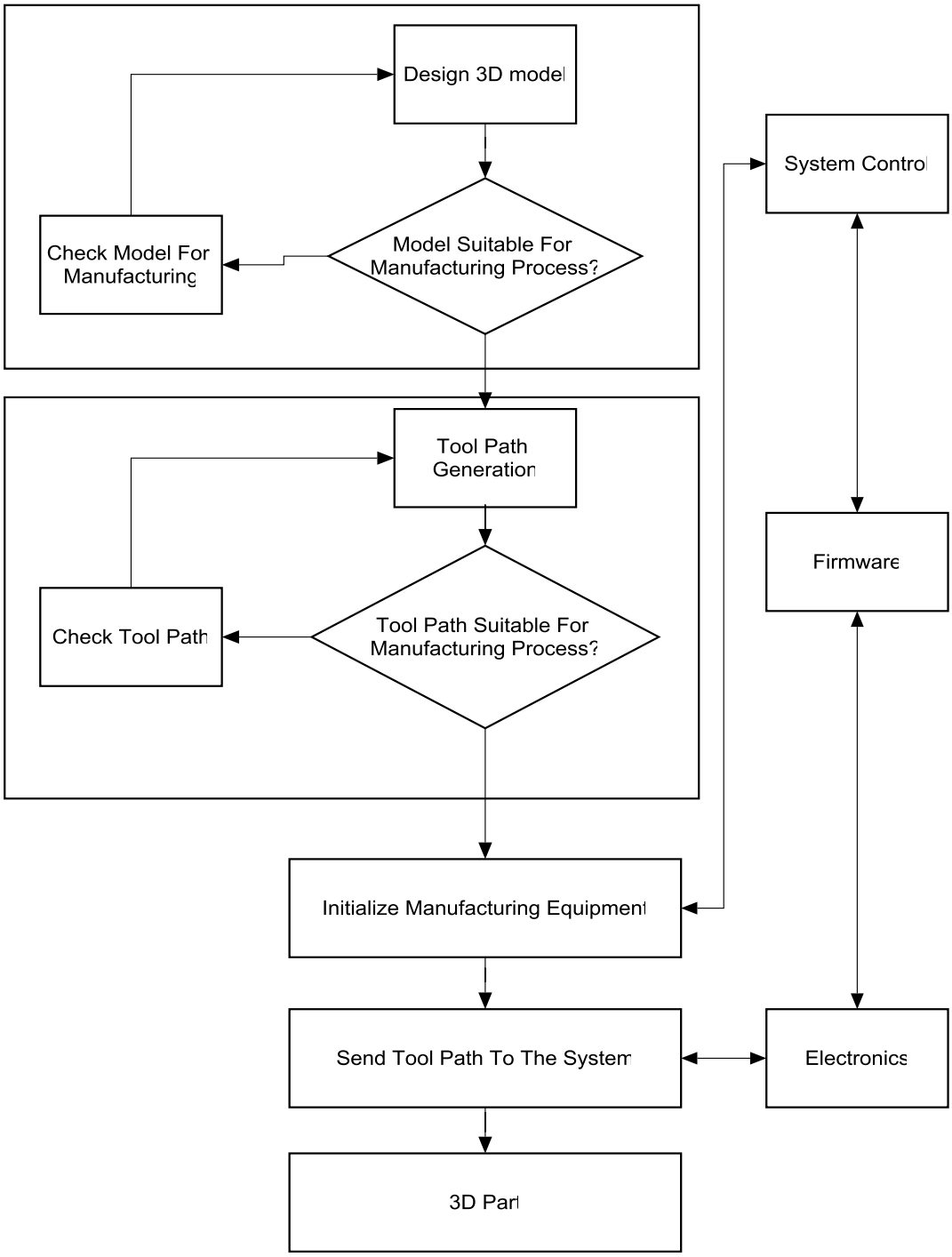


Figure 12. Process map of SLS system

### 1.3 Tool Path Planning

Tool path generation is one of the CAD steps used to generate the necessary part. Two types of paths are used in the AM technique: internal and external. The internal tool path is used to fill the entire part while the outer tool path is used to adjust part roughness. The purpose of studying the tool path types is to reduce surface roughness and increase the mechanical properties of the components [20, 21].

Figure 13 shows line scanning of the slicing and tool path planning. Figure 13 (a) shows the input 3D model represented by triangle meshes. Figure 13 (b) shows the sliced contour, where the outer shape is shown in red color, and inner contour is in blue. The tool path for one patterned layer is provided in Figure 13 (c), and Figure 13 (d) is a close-up view of the whole feature on the layer [22].

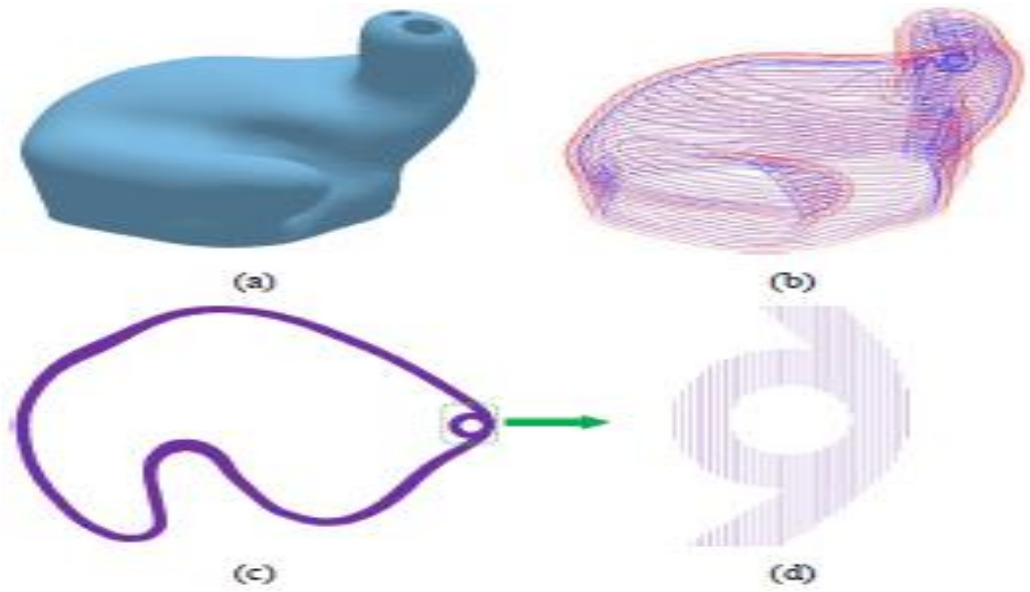


Figure 13. Slicing and path planning [22]

There are many toolpath types used in TM and AM processes, such as zig-zag, zig, isoparametric, isoscalop, and smooth zig-zag, such as shown in Figure 14 [20]. These tool paths are simple to design, easy to use, and effective in AM fields for 2D melting processes. Each kind of tool path provides different part quality, mechanical properties, and manufacturing time.

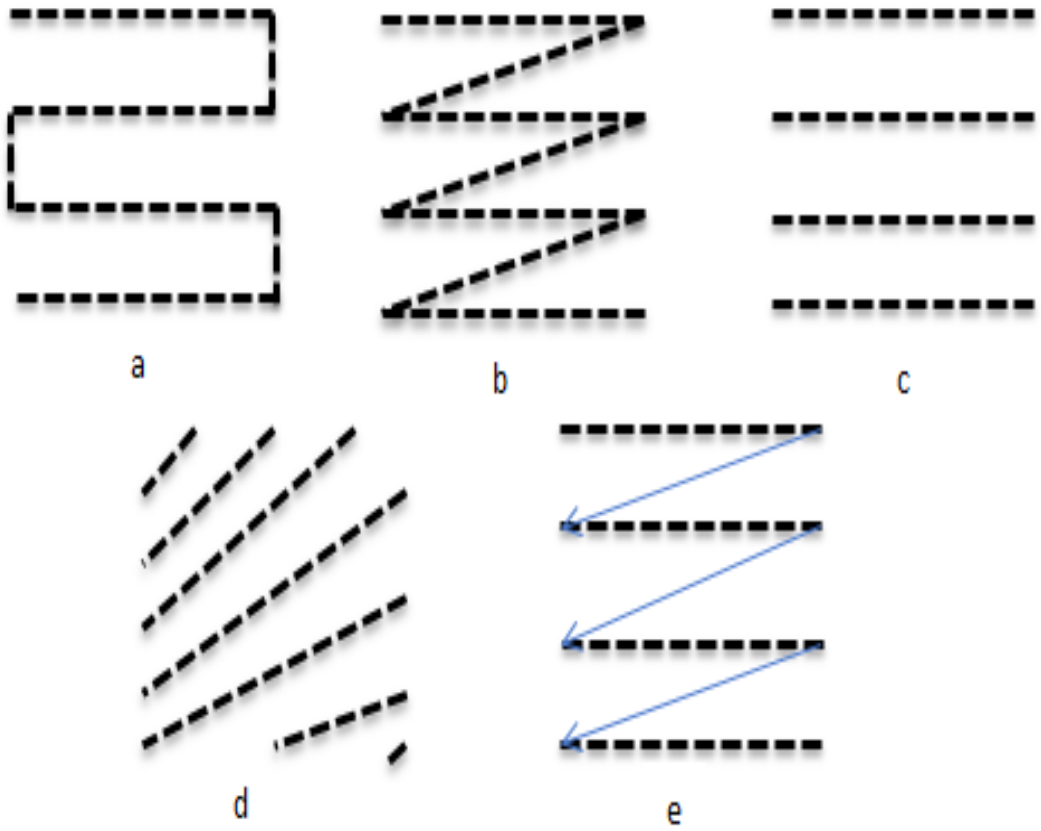


Figure 14. Shows tool path types. (a) Zig Zag. (b) Zig. (c) Isoparametric. (d) Isoscalop. (e) Isoparametric-Zig

Also, some other tool path types used during the sintering process to study improvement of part quality are: (a) in-direction, (b) bi-directional, (c) alternate bi-bearing, (d) island with 90° rotation and (e) island with 90° turns. See Figure 15 [18].

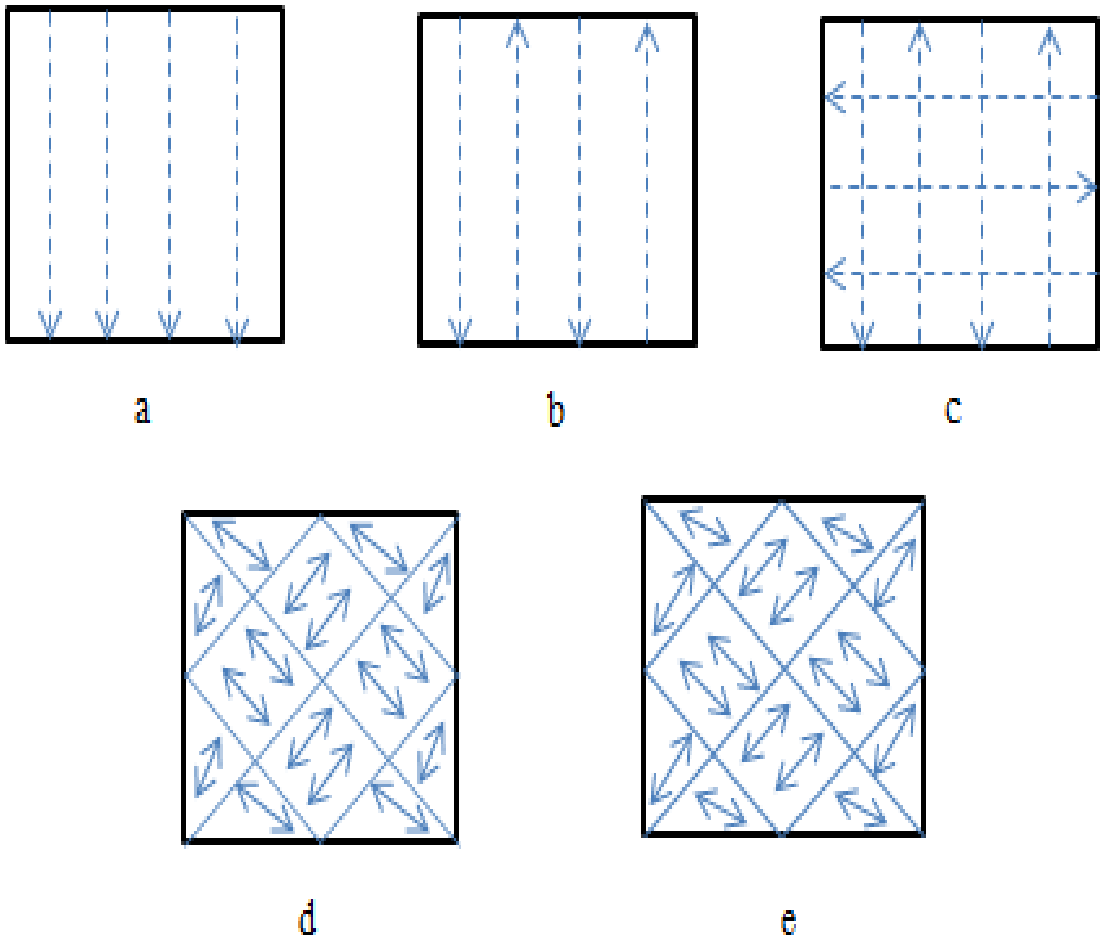


Figure 15. Five different scan strategies [18]

Figure 16 shows manufacturing variables (forward and sidestep). The production process has two types: approximation and interpolation. The approximation method does not have a specific way to calculate manufacturing operation like forward step and side step, feed, manufacturing speed, etc. Therefore, the approximation method produces part that has bad quality, but the interpolation method calculates every step of the manufacturing process.

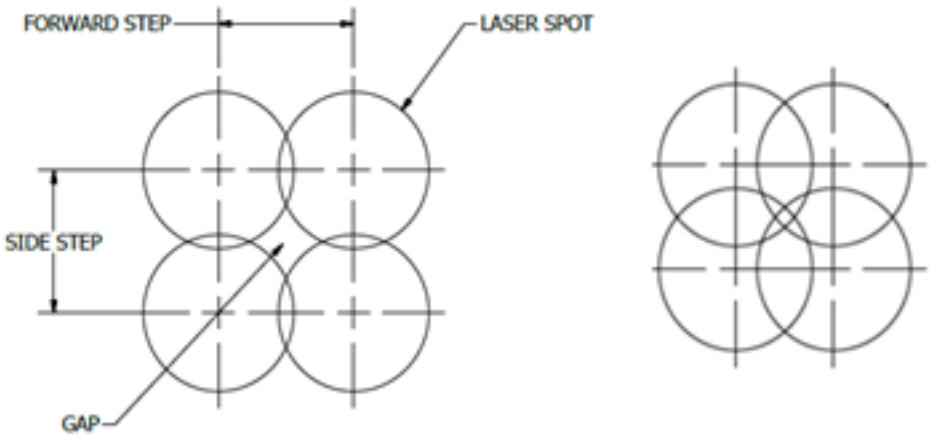


Figure 16. Forward and side steps types(a) Approximation spot (b) Interpolation spot

## 1.4 Part Quality

### 1.4.1 Distortion, Shrinkage and Warping

Distortion, shrinkage, and warping are the major defects that affect part quality. The amount of shrinkage depends greatly on the laser power, layer thickness, and scanning speed. The internal stresses that happen during the printing process lead to distortion and shrinkage [21, 23], see Figure 17 and Figure 18.

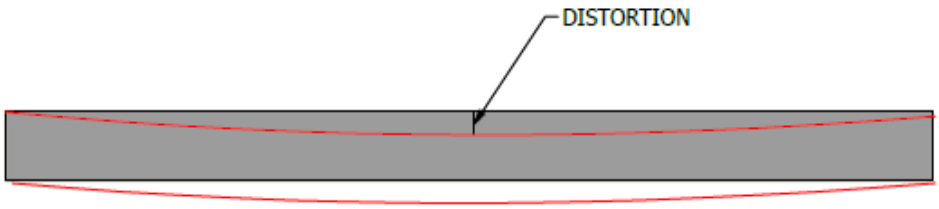


Figure 17. Distortion in RP systems

Figure 18. Shrinkage defect of SLS process

The proposed guidelines about shrinkage, distortion, and warping are [21]: to consider a geometric design, to recognize layer thickness, to respect laser power, scanning speed, and to respect material properties.

### 1.4.2 Surface Finish

The surface roughness value (Ra) is a measure of a part's surface finish. The surface roughness depends on building orientation, layer thickness, and post processing. Equation below is used to estimate average surface roughness (Ra), see Figure 19, by [21, 24]:

$$\mathrm{Ra} = \frac{L}{2}\left|\frac{\cos(\theta-\phi)}{cos\phi}\right| \tag{1.1}$$

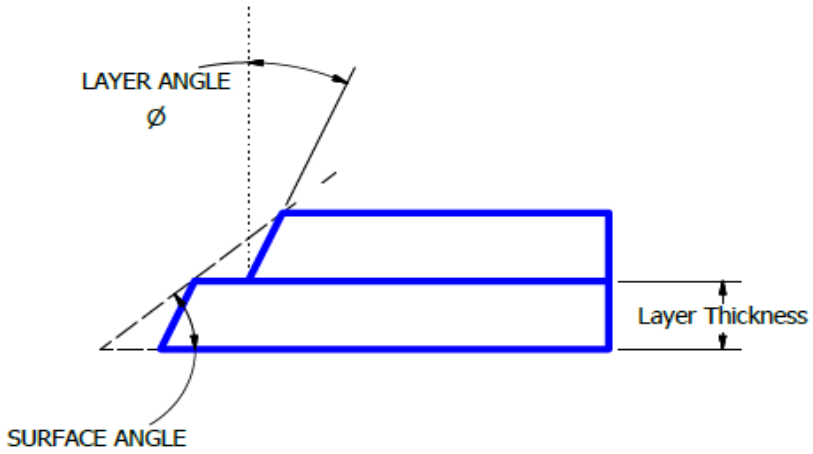


Figure 19. Surface roughness parameters in RP systems [21]

The proposed guidelines about the surface finish are [21]: to calculate the desired surface roughness theoretically, to calculate layer thicknesses, and using 90° of layer angle surface. Each manufacturing process produces different surface properties. Table 1 shows different types of manufacturing process and range surface finishes for each process. Therefore, before starting to produce parts with a specific surface roughness, the table helps the designer to choose the right manufacturing process to match part surface properties.

Table 1. Manufacturing processes with surface finish [25]

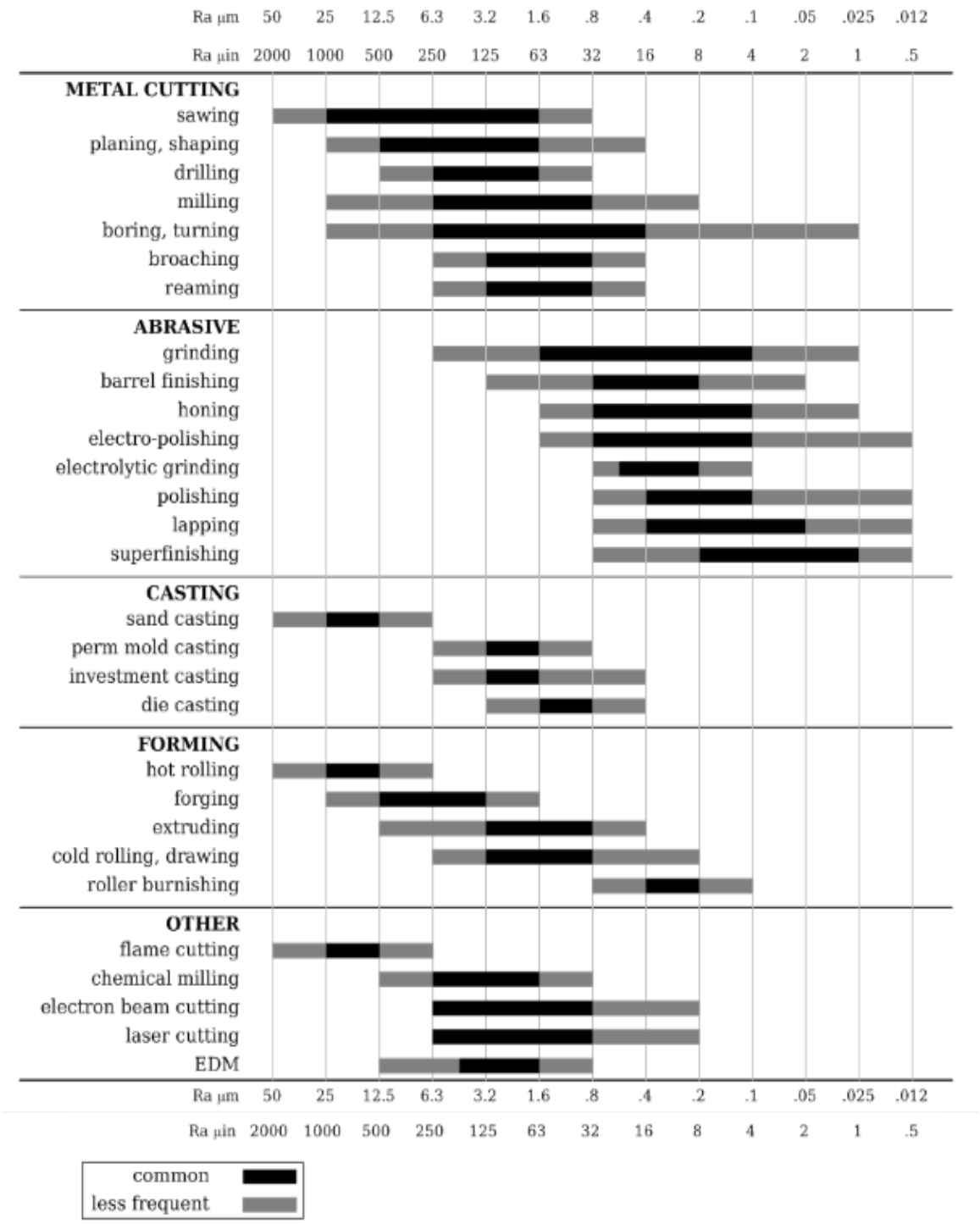

### 1.4.3 Accuracy

The accuracy of an RP system requires it to produce parts with a particular dimensional range. There are several factors that affect part accuracy such as the RP system, deviations, and shrinkage. Most commercial RP systems have accuracy equal to or less than 0.10mm [26, 27, 28], but there are some systems that can provide high precision. Epoxy resin is used to reduce shrinkage that happens during the printing process. The accuracy also depends on the thermal expansion coefficient of the material. The proposed guidelines about the accuracy are [29, 21]: to consider the defects guidelines, shrinkage and warping, and to respect chamber temperature.

### 1.4.4 Porosity Structure

During the powder melting process some defects will happen, and one of those defects is porosity. Porosity is generally considered a bad feature because part quality will decrease with increased porosity. There are two types of porosity: regular and irregular porosity. For some applications, porosity is considered a desired feature such as while producing scaffolded parts, see Figure 20. For other applications, porosity is considered an undesired feature during producing rapid parts, see Figure 21 [30].

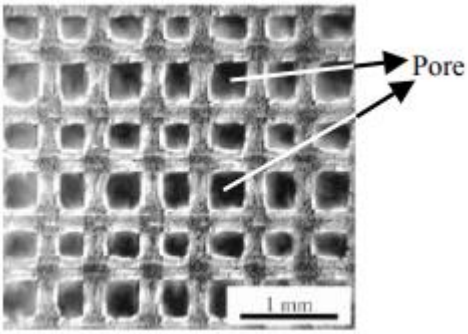


Figure 20. Regular porous structure [30]

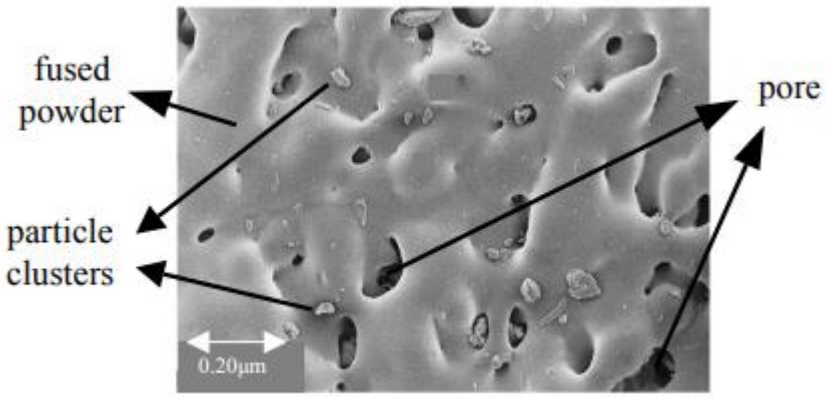


Figure 21. Shows porosity in the SLS product [30]

There are many of variables that can increase or decrease the part porosity and increase part weakness, such as step size (forward step and side step), laser power, laser beam diameter, manufacturing speed, and layer thickness, see Figure 22 [30, 31].

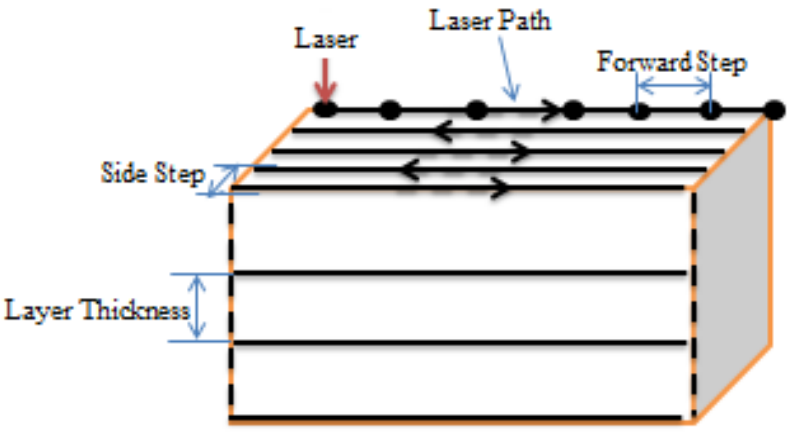


Figure 22. SLS processing parameters affecting porosity [30, 31]

Minimizing the distance between the melting lines leads to providing lines nearer to each other and that produces the overlap fusion, as seen in Figure 23. The overlapping process can reduce porosity and support the part. The big particles absorb the most energy of the laser. The melting process should happen for the current layer with the previous layer to enhance part quality [30, 31].

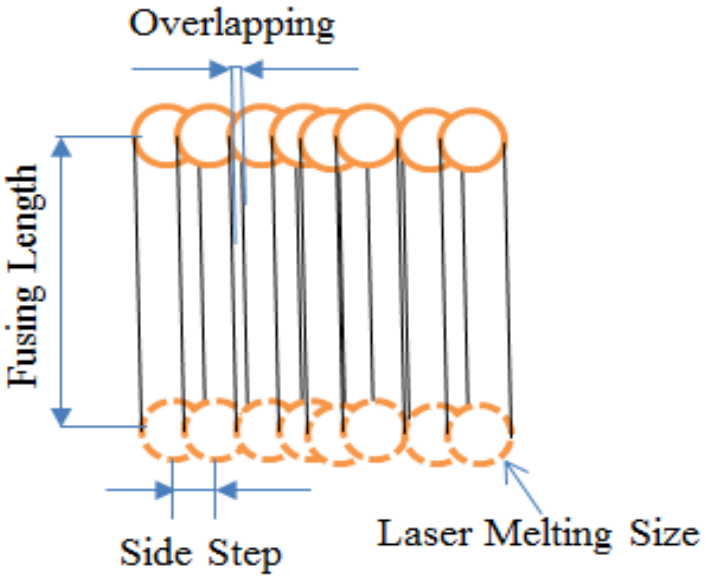


Figure 23. Schematic of multi-line laser scanning of SLS

The laser applies the powder to make a uniform particles temperature, and the melting process happens after the temperature exceeds the melting process. Furthermore, the particles' melting is affected by material properties and manufacturing parameters.

Figure 24a displays a soft zone amongst solid and liquid temperatures, in which the liquid and solid phase exists together during the melting/solidification process. The best sintering temperature is in the mushy zone because this area creates a semi-solid framework. As shown in Figure 24b, pre-alloyed particles melt to be liquid once an adequate amount of liquid is provided along grain limits. Niu et al. have shown that the supersolids liquid phase sintering (SLPS) system of powder during LS of steel powder. Figure 24c shows the ring microstructure around the grain, and that indicates the development of the liquid phase along grain boundaries inside particles amongst SLPS [1].

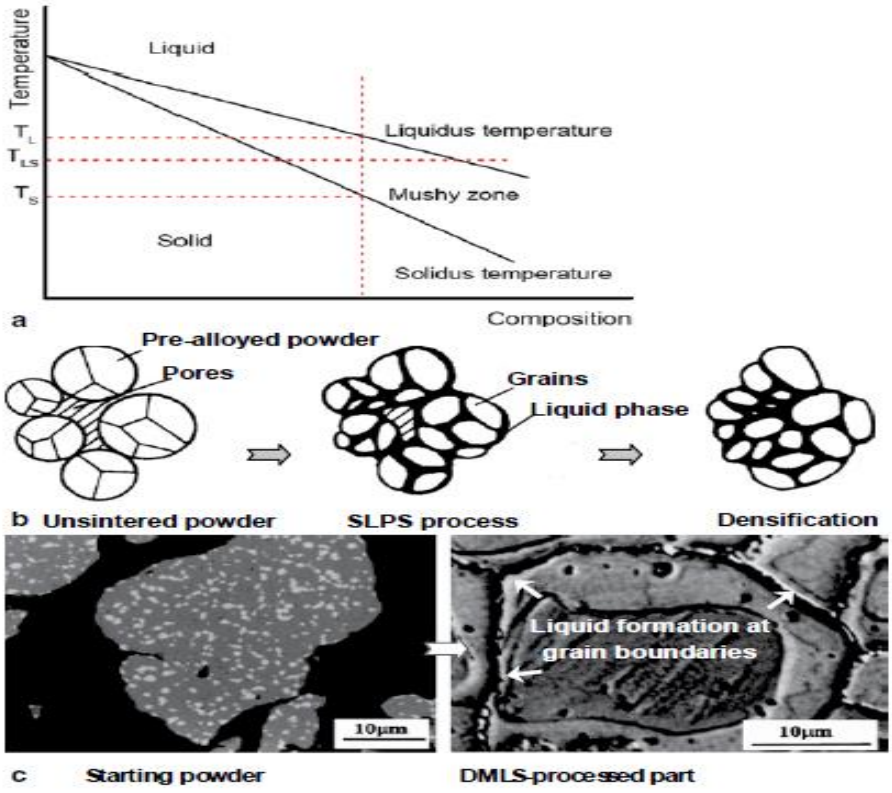


Figure 24 (a) An idealized temperature-composition equilibrium phase diagram for an alloyed binary metal system, (b) Schematic of SLPS densification of alloyed particles, (c) Microstructural development during LS of high-speed steel powder [1]

## 1.5 Contribution

The research scope is to design, build, and validate a low-cost prototype SLS system, and optimize SLS process parameters using the prototype system to minimize defects during the manufacturing process. The prototype SLS system can be used to create a 3D part by using different kinds of material, like plastic, nylon, steel, aluminum, and ceramic.

## 1.6 Dissertation Outline

The study is organized as follows: Chapter two is a literature survey divided into SLS process variables and DOE, SLS raw materials, tool path generation, and laser and powder interactions. Chapter three discusses review modeling of laser thermal interactions. Chapter four is used to design, build and validate the prototype SLS system. Chapter five is optimization of the SLS manufacturing process. Chapter six concludes the work.

# 2. LITERATURE SURVEY

SLS is one of the rapid manufacturing processes that can produce parts from a wide range of prototype materials [32]. Unfortunately, parts produced by SLS are not accurate due to the various errors accumulating from data preparation stage to finishing stage [33].

This section will discuss papers that are relevant to this research. The literature survey is divided into four sections. The first section is SLS process variables, design of experiments, and system design. The second section is raw materials. The third section is tool path generation. The last section is laser and powder interactions.

## 2.1 SLS Process Variables, Design of Experiments, and System Design

It is difficult to achieve the desired accuracy in parts produced by different rapid manufacturing processes. The part accuracy is a function of many different factors, some of which can be interdependent [33]. Layer thickness, laser power, and toolpath are parameters used to optimize each process depending on the applied binding mechanism and chosen powder material [34].

Raghunath and Pandey focused on shrinkage [29]. This defect influences part accuracy in the SLS technique. Also, this paper studies parameters that have an effect on the increased or decreased shrinkage during the manufacturing process, such as laser power, beam speed, hatch spacing, part bed temperature, and scan length. The researchers found laser power and scan length are significant variations in X-direction. Laser power, and beam speed (significantly in Y-direction). Beam speed, hatch spacing and part bed temperature are relevant variables on shrinkage in Z-direction. The researchers did not

consider thermal stress during manufacturing process and the relationship between material properties and laser power.

Luo and Tzou used the Taguchi method utilized in this paper to analyze parameters, such as layer thickness, path width, and nozzle speed [35]. Based on the results, the proposed RP system can produce good quality parts with an adaptive slicing algorithm. This paper did not mention the relationship between thermal conditions of material and surface roughness.

Kruth et al. presented the limitations of SLS/SLM processes [34]. They focused on different SLS/SLM processes regarding manufacturing conditions, such as material, speed, accuracy, mechanical properties, and reliability. A benchmark model was used to check manufacturing conditions and process limitations. The researchers used five methods with different equipment, binding mechanism, material, laser power, and layer thickness. One process guaranteed a small surface roughness, while another method showed a smooth top surface. The researchers spent a long time on for trials and did not use any optimization technique to reduce total time.

Yang modeled a 3D auxetic structure via Timoshenko beam theory and the Euler-Bernoulli beam theory [36]. The models derived could predict various mechanical properties of this auxetic structure, such as strength, elastic modulus, and Poisson's ratio. The researcher used the SLS technique to produce the models. The errors are discussed in this research. This work provides a guideline and a methodology for future design and applications of the 3D auxetic structure. This project did not show the relationship between mechanical properties and parameters.

Paul and Anand optimized a model to calculate layer thickness, orientation, and the total area of sintering to reduce laser energy [37]. The mathematical model to optimize laser energy was developed by using an Interior-Point algorithm. The researchers succeeded to represent an optimization model of minimum total area of sintering TAS and laser energy to produce a part by using the SLS technique.

Chatterjee et al. used the design of experiments to build three mathematical models [31]. The first one is for porosity, the second one is for hardness, and the third one is for density. The parameters used to create the mathematical models are layer thickness and side step with five levels for each parameter. The researchers found increasing side step and layer thickness led to increased porosity and decreased part hardness.

Kumar et al. represented the effect of three parameters (laser control, temperature, and part orientation) on dimensional precision and micro-hardness of parts made using SLS [38]. The Taguchi technique and an orthogonal array were used to minimize the number of experiments and analyze the hardness and the part dimensions.

Chung and Das blended test studies, theoretical modeling and numerical analysis [39]. The design of experiments produced optimal parameters for every creation. These parameters were contrasted and parameters predicted by mathematical modeling. They measured tensile and compressive moduli and the final results compared with Halpin's theoretical model.

Khan et al. used a genetic algorithm and simulated annealing to get optimal cutting parameters for manufacturing processes [40]. Nonlinear production models were used with the objective function to determine optimal cutting conditions.

Zain et al. used simulated annealing and genetic algorithm techniques to get optimal parameters of waterjet machining [41]. The researchers worked on determining the regression model of the manufacturing parameters, then worked on estimating optimal variables by SA-GA techniques.

Afkhamifar et al. worked on the analysis multi-axis automation system [42]. Finite element analysis was used to predict a manufacturing error during running the system.

Mao et al. worked to check manufacturing error of an automation system [43]. The system was working on five axes. The system features can control all the system axes together to achieve a manufacturing process with a high accuracy and ease of operation. Researchers to improve the automation system are used a volumetric error compensation algorithm. Some experiments has applied to check manufacturing error, and maximum error was ±7 μm.

Stwora and Skrabalak [44] examined variety parameters affecting the SLS process including material parameters, process parameters, layer parameters, and economic factors. The largest contributors of producing parts were laser power, distance, and exposure time.

## 2.2 SLS Raw Materials

The SLS process is vastly studied for polymer and metal powders to produce fully functional parts. Although SLS of ceramics was initiated at the beginning of the 1990s, the technology has not yet been commercialized due to the complexity of laser processing of ceramic powders [45].

Song and Koenig studied SLS for direct sintering of bronze [46]. This material has a low-melting metallic powder, and researcher investigated only spots without powder

preheating and with polymer as the binder. The parameters used in this paper were laser beam power, scanning speed and hatching distance, material parameters (particle size influences the melting behavior). The paper showed the significant parameters affect part quality, such as roughness and bonding between layers. The project did not consider critical parameters such as spot size and layer thickness.

Shahzad et al. used indirect SLS to produce 3D complex shape by using ceramic powder in a two-step process [45]. Polyamide 12 and submicrometer-sized alumina are utilized in this research because the composite powder has excellent formability. The effect of laser power, scan speed and scan spacing on the fabrication of green parts was considered in this research. They found at lower energies, the parts distorted whereas polyacrolein burned at higher energy inputs. The sintered density of aluminum oxide ($Al_2O_3$) ceramics was limited to only 50% compared with theoretical density. The work produced parts of $Al_2O_3$ ceramics, but without a good quality.

Shahzad et al. used indirect SLS with use of innovative powder preparation and post-processing techniques to obtain high-density ceramic parts [47]. Also, they studied the effect of polymer concentration, cooling rate, stirring and alumina particles on polymer and polymer-ceramic composite particles. The researchers got increased polymer concentration when increasing polymer particles and agglomerates, and "Mechanical stirring during phase separation reduced the particle size and degree of agglomeration of the polypropylene particles. The addition of alumina decreased particle agglomeration and inhibited particle fracturing. Increasing the alumina concentration reduced the particle size" [47], see Figure 25.

Slaviero studied the addition of determining amounts of carbon black nanoparticle suspension to obtain functionally graded samples in the standard 3D printing binder during the printing process [48]. This work focused on studying shrinkage, density, carbon content and porosity measurements.


Figure 25. Complex parts produced by the SLS pressure infiltration depending sintering route [47]

Kruth et al. presented the various binding mechanisms in SLS and SLM, and use them for a broad range of materials and applications [49]. The researchers explained the connection between the content of sintering and the materials used. This paper looked for full melting of powder to produce a part with good quality. The researchers said, "the idea of full melting metal powders was explored, supported by the continually by improving the manufacturing variables" [49]. However, the researchers did not mention the thermal distribution of the power during the melting process.

Liu et al. presented a method to prepare polymer-coated molybdenum powder [50]. In this paper, the post-treatment of parts produced by the laser sintering process has improved. They found a relationship between scanning speed and relative density,

sintering depth and laser power, sintering depth and scanning speed, relative density and powder layer thickness, and relative density and laser power.

## 2.3 Tool Path Generation

The toolpath is the trajectory of the manufacturing tool holder during an RP process to fill the interior and exterior of part. There are many types of toolpath strategy algorithms, such as contour, zigzag, and spiral patterns. Tool path selection should consider building time, surface quality, cost, defects, and mechanical properties of the part [12].

Jin et al. suggested systematic adaptive algorithms to generate tool paths for complex shapes of rapid prototyping [12]. They assumed two types of tool paths; the first one is the contour tool path for the boundary of the part to reduce error, and the second one is zig-zag for the area inside the part to increase manufacturing speed. They found a tool path algorithm very efficient to produce parts have an excellent surface quality.

Jin et al. presented a hybrid, and adaptive tool-path generation approach, which can create a part has good accuracy and build time of RP/RM for complex biomedical models by using NURBS (Nonuniform Rational B-Spline) of sliced layers [20]. They used contour tool path with the zig-zag tool path to increase manufacturing speed and accuracy of the parts. They got good quality by using the proposed algorithms with reducing printing time.

Yang et al. suggested a fractal scanning path that produced a part by using the SLS system [51]. The results proved parts that were created by using the fractal scanning path have a good physical performance. Also, the researchers improved trimming process of the fractal scanning path out of a non-square part to keep the fractal scanning path feature. Two types of tool paths are zig-zag and the fractal scanning path used to make a

comparison between parts. The fractal scanning has produced an excellent physical property of parts.

Jin et al. developed a novel path filling pattern of AM to reduce and avoid retraction during the printing process [52]. Also, this tool path can reduce total time and avoid discontinuous printing. “Go and back” is a path planning used to reduce the retraction problems and generate a continuous printing. Many types of tool paths were used to check the developed methodology conducted with path filling type. The final results decreased the retraction printing and produced a high-quality part.

Asiabanpour et al. proposed paths to remove a part quickly from the system table [53]. Two types of paths used in this research are boundary and hatch paths. Different sizes and complexity parts were produced by using proposed paths. Testing the process of the path used before sending it to the system reduced errors during the printing process.

## 2.4 Laser And Powder Interactions

Table 2 shows some of the commercial machines in the market for laser forming of metals by layer manufacturing technologies with laser systems, the laser power range is between 50W-18kW [54].

Table 2. Commercial machines and lasers [54]

| Machines | Company | Process | Laser | Power |
|---|---|---|---|---|
| Sinterstation 2000/2500 | DTM | DMLS | $CO_2$ | 50 W |
| EOSINT 250 | EOS | DMLS | $CO_2$ | 200 W |
| EOSINT 270 | EOS | DMLS | Ytterbium fibre laser | 200 W |
| LUMEX 25C | MATSUURA | SLM | Pulsed $CO_2$ | 500 W |
| TrumaForm LF 250 | TRUMPF | SLM | Disk laser | 250 W |
| Realizer | MCP | SLM | Nd:YAG | 100 W |
| Lasform | Aeromet | 3D laser cladding | $CO_2$ | 10–18 kW |
| LENS 850 | Optomec | 3D laser cladding | Nd:YAG | 1 kW |
| Trumaform DMD 505 | TRUMPF | 3D laser cladding | $CO_2$ | 2–6 kW |

Kruth et al. focused on providing a survey of consolidation mechanisms used in laser and powder bed based layered manufacturing, and the researchers also proved how the material properties and composition play an important role to produce a part of high quality [55].

Murali et al. studied laser sintering of a powder mixture of iron and graphite using the Nd-YAG laser [56]. The paper results explained the microstructures and the physical and mechanical properties of the sintered material, such as wear, density, and hardness.

Streek et al. studied energy penetration of a laser beam into a powder layer related to grain density, grain size, laser beam intensity, and material properties [57]. They found better melt when the grain size is small. Also, they got better quality when the layer thickness is 8 μm.

Simchi studied densification and microstructural evolution during direct laser sintering of various ferrous powders and high-speed steel was used in research [58]. The first-order kinetics equation was related to the energy input of the laser beam. The researcher calculated the powder densification from the parameters: laser power, scan rate, layer thickness and scan line spacing. The researcher found the laser energy achieved better densification when using higher laser power, lower scan rate, lower scan line spacing, and lower layer thickness.

Manfredi et al. presented a characterization of an AlSiMg alloy processed by direct metal laser sintering [59]. They analyzed powders in size, morphology and chemical composition, evaluation of mechanical and microstructural properties of specimens built with different orientations parallel and perpendicular to the powder deposition plane.

They found particles with a diameter lower than ten μm tend to agglomerate, forming bigger clusters of irregular shapes.

# 3. REVIEW OF MODELING OF LASER THERMAL INTERACTIONS

Laser applications exist in many different fields, such as engineering and medicine. The laser can heat, melt, and vaporize materials [60]. This section reviews thermal modeling of laser-powder interactions within the SLS process with application to design of the prototype SLS system.

## 3.1 Laser System

SLS uses a high power laser to melt a powder and build a 3D part. Each material needs a specific laser power to start the melting process. Laser energy is divided into sections that are used to warm and melt powder [60]. Gedda et al. checked distribution of the laser energy of high power lasers. The results are shown in Table 3 [61].

Table 3 demonstrates just 10-20% of the laser energy is used to melt the powder layer. Laser reflection, powder heating, and melting previous layer are dependent on powder properties.

Table 3. Redistribution of laser power during laser cladding [61]

| Use of laser power | Laser |
|---|---|
| Reflected off the cladding melt | 40-50% |
| Reflected off the powder cloud | 10% |
| Heat the substrate | 30% |
| Melt the substrate/previously deposited layer | 10-20% |

The melting process starts when the laser energy is enough to melt the powder. If a very high power laser is used, that will lead to thermal defects because of over melting of

powder the during manufacturing process. On the other hand, if not enough energy is used to melt the powder that will cause a reduced melting process and produce parts with a bad quality because there is not enough energy to melt powder. For a particular laser energy (E) can be calculated by

$$E = \frac{P}{D \times V} \tag{3.1}$$

The calculation of E must be precise and accurate to accomplish a specific melting of the powder.

There is a necessary mix of processing parameters that produce a specific melting of powder. These parameters are laser energy and powder fed per unit length. Also, manufacturing parameters and material properties affect the melting ratio between width to height. Therefore, blending manufacturing parameters can produce different qualities. Figure 27 presents the manufacturing parameters and their effects on the part geometry [60].

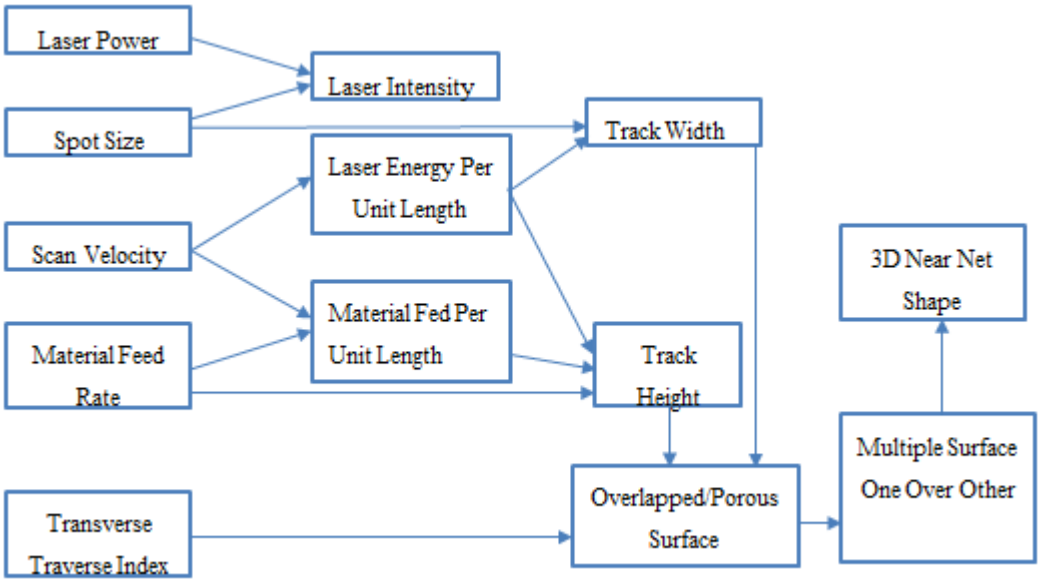


Figure 26. Relevant processing parameters and their effects [24]

## 3.2 SLS Thermal Phenomenon

There are many models that consider laser penetration into the powder bed because of its porosity. A ray tracing model has been simulated considering the geometry and structure of the powder. The laser beam is modeled as a ray, and it is both reflected and absorbed by the surface of powder particles until the power of the radiation reaches the wall of the powder container, as shown in Figure 27 [18].

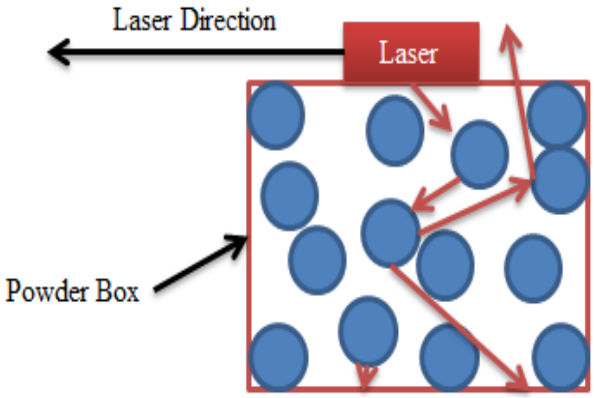


Figure 27. 2D illustrations of the ray tracing model: simulation over a depth of 1mm and width of 1mm of powder bed [18]

Figure 28 shows a schematic representation of a laser melting process on the surface of a powder bed. When the laser is applied to the powder, the powder temperature will warm up to start melting the powder. The heat transfer during sintering process is divided in to three parts: conduction within powder, convection from powder to air, and radiation from powder to surroundings. All these parts happen during melting process.

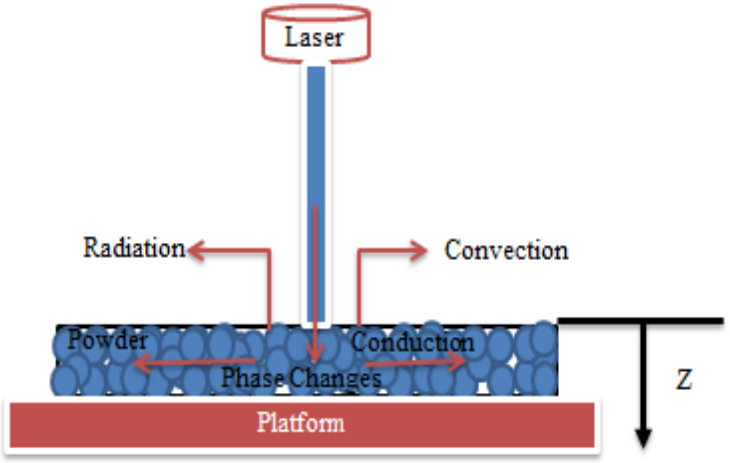


Figure 28. Schematic representation of heat transfer

There are two cases of the powder during manufacturing process: solid case and melting case. When the laser hits the powder, the lase energy will be absorbed by the powder, the solid case of powder start heating to fuse the powder. The fusing process happens when heat that applies on the powder exceed melting point and that changes the powder case from solid to liquid. Therefore, during melting process of SLS technique should consider solid and liquid cases to determine melting mathematical model [60].

### 3.3 Governing Equations and Boundary Conditions

Fourier heat conduction hypothesis is used widely to describe the different heat conduction states. Many researchers use the heat conduction condition as shown in equations below [18].

$$\lambda(T)\left(\frac{\partial^2 T}{\partial x^2}+\frac{\partial^2 T}{\partial y^2}+\frac{\partial^2 T}{\partial z^2}\right)+q=\rho(T)\,C(T)\frac{\partial T}{\partial t} \tag{3.2}$$

Starting temperature is described by

$$T(x,y,z)=T_0 \tag{3.3}$$

Convection of the surface is described by

$$-\lambda(T)\left(\frac{\partial T}{\partial z}\right) = h(T - T_e) \tag{3.4}$$

There is no heat is going to a loss at the base, for example, as follows

$$-\lambda\frac{\partial T}{\partial z}\Big|_{z=0} = 0 \tag{3.5}$$

### 3.4 Laser Beam Approximation Modeling

The Gaussian model has used a symmetrical distribution of laser irradiance over the beam. There are three fundamental modes for the Gaussian model: TEM00, TEM01, and TEM02. Equation below shows the Gaussian intensity distribution for the basic mode TEM00 [18].

$$I(r) = I_o e^{-2\left[\frac{r}{r_1}\right]^2} \tag{3.6}$$

The thermal heat flux is characterized as the thermal power per unit range, as shown below

$$q(r) = \frac{2P}{\pi r_0^2} e^{-\frac{2r_d{}^2}{\pi r_0^2}} \tag{3.7}$$

Furthermore, the average heat flux ($q_m$) on the laser spot is shown in Equation below by utilizing the same definition from heat flux [18].

$$q_m = \frac{1}{\pi r_0^2}\int_0^{r0} q(2\pi r)dr = \frac{0.865\,\alpha\,p}{\pi r_0^2} \tag{3.8}$$

#### 3.4.1 Solid Heating Case

During laser manufacturing, the material changes from solid to fluid and back to the solid state. Therefore, This section will explain the mathematical equations to the thermal conductivity and the beginning of the fusion process. By relying on the powder properties

and the laser beam diameter, the laser powder that needed to melt powder will be determined [18].

When applying the laser onto the powder, the laser energy starts heating up from room temperature to the melting point. The workpiece (powder) is subjected to a laser heat beam at the surface $z = 0$. The heat conduction condition is described by

$$\frac{\partial^2 T_S}{\partial Z^2} = \frac{1}{\alpha_S}\frac{\partial T_S}{\partial t} \tag{3.9}$$

The melting process started with conditions are

$$T_S(z,0)=T_0 \tag{3.10}$$

$$I_{abs} = -k_s \frac{\partial T_S}{\partial z}]_{Z=0} \tag{3.11}$$

Absorbed laser intensity is defined by

$$I_{abs} = (1 - R_f)I_0 = A_s I \tag{3.12}$$

Carslaw and Jaeger [62] answered the above arrangement of equations when the laser intensity profile is in the form

$$I(z,t) = I_{abs}\text{erfc}\frac{z}{2\sqrt{\alpha_s t}} \tag{3.13}$$

where erfc is the complementary error function

$$\text{erfc}(x) = 1 - \text{erf}(x) = \frac{2}{\sqrt{\pi}}\int_x^{\infty} e^{-u^2}du \tag{3.14}$$

and erf (x) is the error function defined by

$$\text{erfc}(x) = \frac{2}{\sqrt{\pi}}\int_x^{\infty} e^{-u^2}du \tag{3.15}$$

The temperature profile in a solid is observed to be

$$T_s(z,t) = T_0 + \frac{2I_{ab\,c}}{k_s}\left[\left(\frac{\alpha_s t}{\pi}\right)^{\frac{1}{2}} e^{-z^2/4\alpha_s t} - \frac{z}{2}\text{erfc}\frac{z}{2\sqrt{\alpha_s t}}\right] \tag{3.16}$$

The goal to determine the temperature model is to evaluate the time required to start the melting process. For a single laser pulse heating, the temperature at the surface (z= 0) can be gotten from [60].

$$T_s(0,t) = T_0 + \frac{2I_{abc}}{k_s}\left(\frac{\alpha_s t}{\pi}\right)^{\frac{1}{2}} \tag{3.17}$$

A series of laser pulses are utilized, as shown in Figure 29. Each successive laser pulse is separated by a pulse off time where there is no laser beam connection. The temperature increase during the pulse ON-time and decreases when the pulse turns OFF-time [60].

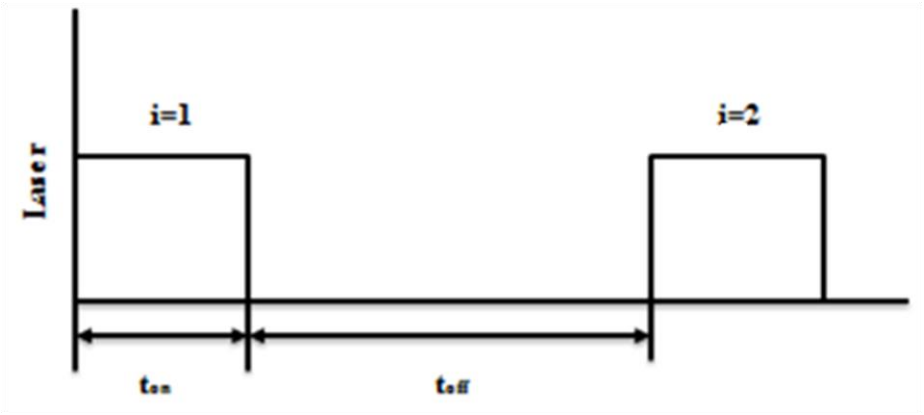


Figure 29. Time step in laser sintering [60]

The changing of the surface temperature through the $i_{th}$ cycle can be determined from a pair of equations for pulse ON-time and pulse OFF-time. During the pulse ON-time surface temperature is given by

$$T_{on,i}(0,t) = T_{(i-1)/f} + \frac{2I_{abs}}{k_s}\sqrt{\frac{\alpha_s(t-{}^{(i-1)}/_{f})}{\pi}} \tag{3.18}$$

while

$$\frac{i-1}{f} \le t \le (\frac{i-1}{f} + t_{on})$$

Then during the pulse OFF-time, surface temperature is given by

$$T_{off,i}(0,t) = T_{(i-1)/f} + \frac{2I_{abs}}{k_s}\left[\sqrt{\frac{\alpha_s\left(t-{}^{(i-1)}/_{f}\right)}{\pi}} - \sqrt{\frac{\alpha_s\left(t-t_{on}-{}^{(i-1)}/_{f}\right)}{\pi}}\right] \quad (3.19)$$

while

$$\left(\frac{i-1}{f} + t_{on}\right) \le t \le \frac{i}{f}$$

### 3.4.2 Melting Case

Two zones are produced when applying a high power laser on a workpiece's surface. The upper zone will be liquid and the lower zone is solid, so solid and liquid cases should consider during the melting process, see Figure 30. Some considerations should take care of them while preparing the laser beam. The laser beam should be wider than the molten zone, and depth of the laser also should be deeper than the thermal penetration depth to get an appropriate melting of the powder. The mathematical model is applied to different materials, and the mathematical model depends on thermos physical parameters to consider solid and liquid phases during the melting process [60].

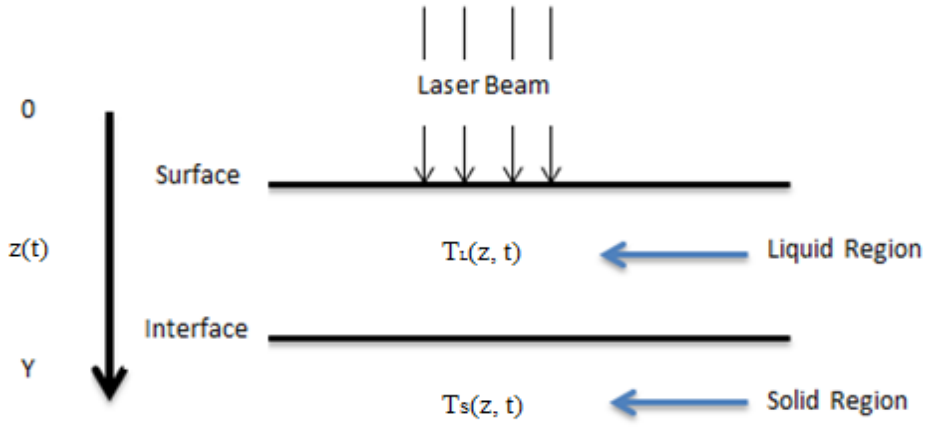


Figure 30. The geometry of laser irradiation [60]

There are two equations are used to to describe the heat conduction conditions of liquid and solid cases. The heat conduction conditions of liquid case is given by

$$\frac{\partial^2 T_l(z,t)}{\partial z^2} - \frac{1}{\alpha_l}\frac{\partial T_l(z,t)}{\partial t} = 0, \qquad 0 \le z \le z_m \tag{3.20}$$

The heat conduction conditions of solid case is given by

$$\frac{\partial^2 T_s(z,t)}{\partial z^2} - \frac{1}{\alpha_s}\frac{\partial T_s(z,t)}{\partial t} = 0, \qquad z_m \le z \le \infty, \tag{3.21}$$

The boundary conditions given by

$$-K_l \frac{\partial T_l(z,t)}{\partial z} = A_l I_0, \qquad z = 0, \tag{3.22}$$

The boundary conditions of the temperature profiles in a liquid and solid given by

$$T_s(z,t) = T_l(z,t) = T_{m;} \qquad z=z_m(t) \tag{3.23}$$

The boundary conditions of the latent heat in a liquid and solid given by

$$\rho_s L_m \frac{dz_m(t)}{dt} = k_s \frac{\partial T_s(Z,t)}{\partial z} - k_l \frac{\partial T_l(Z,t)}{\partial z}; \qquad z = z_m(t) \tag{3.24}$$

while

$$T_s(z,t) = T_{O;} \qquad z \to \infty \tag{3.25}$$

Some researchers propose nonlinear fractional differential conditions. Carslaw and Jaeger [62] reported an approximated method response in the solidification of a huge liquid mass. It must be noticed that the proposed arrangement is useful just for the model of low power laser irradiation.

The temperature expected in the liquid layer to be as shown in equation below when heat conduction equations at some points, z = 0, z = $z_m$ (t), and z [60].

$$T_l(z,t) = T_m - \frac{A_l I_0}{k_l}[z - z_m(t)] + f(t)[z^2 - z_m^2(t)] \tag{3.26}$$

while

$$f(t) = \frac{A_l I_0}{2\alpha_l k_l (1+\frac{z_m(t) dz_m(t)}{\alpha_l \quad dt})} \frac{dz_m(t)}{dt} \tag{3.27}$$

The temperature profile in the solid an exponential function was assumed by

$$T_s(z,t) = T_m - (T_m - T_O)\{1 - \exp[-b(t)(z - z_m(t))]\} \tag{3.28}$$

while

$$b(t) = \frac{1}{\alpha_s} \frac{dz_m(t)}{dt}$$

By substituting the supposed temperature equations into the heat conduction equations, the fusing depth and the fusing front speed were concluded. Also, the temperature equations proposed the following exponential temperature equations in their laser fusing model [60].

$$T_l(z,t) = T_{l0}(t)\exp[\frac{-z}{\delta_l(t)}] \tag{3.29}$$

$$T_s(z,t) = T_m \exp[\frac{-(z-z_m(t))}{\delta_s(t)}] \tag{3.30}$$

By substituting equations (3.29) and (3.30) into the heat conduction and boundary methods. The $T_{l0}(t)$ will be as shown below [60].

$$T_{l0}(t) = [\frac{2\alpha_l A_l^2 I_0^2}{k_l^2} t + C_0]^{1/2} \tag{3.31}$$

while

$$C_0 = T_m^2 - \frac{\alpha_l k_s^2 A_l^2}{\alpha_s k_l^2 A_s^2}(T_m - T_0)^2 \tag{3.32}$$

In this chapter, the thermal equations of the solid and liquid states were presented of the powder that will be used to build parts. The purpose of this presentation is to determine the mathematical model that will be used to calculate the laser power required for melting the powder.

# 4. SLS SYSTEM DESIGN AND VALIDATION

This chapter will discuss identification of the SLS subsystems, design and fabrication of the prototype SLS system, and validation processes for the prototype SLS subsystem. The validation includes design consideration such as forward step, side step, laser beam diameter, laser power system, and vibration on gantry system.

Before starting the design, any system should determine what the purpose of this system is, which problems this system can fix, and the specifications required to get the target of this design. Figure 31 explains the research steps. This research focuses on increasing the accuracy of the SLS prototype system to study parameters that will affect on part quality, so two types of defects will study in this research are surface roughness and crack width that happen during manufacturing process by using SLS system. The second step is system specifications, such as forward step, side step, and layer depth. The components of the SLS system will pick them up depending on the previous steps, and after taking the elements and assembling process of the SLS system, the validation process will check the system specifications and the system will change until reaching the required resolution [63, 64, 65].

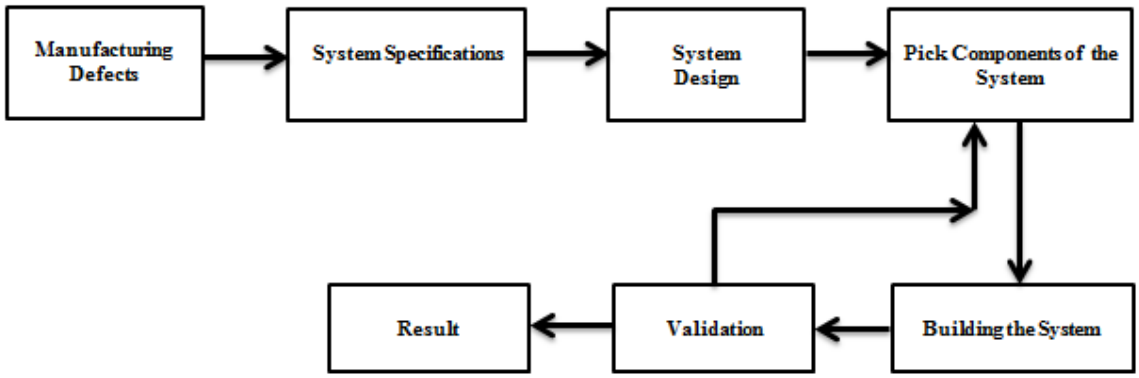


Figure 31. Research flowchart

The prototype SLS system consists of hardware such as microprocessor, motor drivers, stepper motors, gantry system, powder distribution, and laser system. The system movement consists of four axes (X, Y, Z, A). The laser moves in the X and Y field, the powder bed moves in the Z-axis and the powder distribution moves in the X and Y field.

## 4.1 Design Specifications

The prototype SLS system is designed to work on four axes, and the target of design is to use the system to produce parts from powder by using high power laser, easy to use and fix, and can use different powder materials to produce a part. The SLS code language feeds to the microprocessor from a PC by using a USB. Some systems work on image processing or G code or manual controller or STL file, and that depends on the interface program.

The system dimensions and powder table dimensions will select small size because the prototype SLS system use to produce parts small size in laboratory. Nylon powder will use as binder to produce parts by using different powder, such as steel, ceramic, aluminum, etc. Table 4 represents the design specifications for the SLS prototype system. The information in the table was calculated and determined to study surface roughness and crack width of parts that are going to be manufactured by using the SLS prototype system.

Table 4.Specifications of SLS prototype system

| | |
|---|---|
| Structural material | Steel |
| Communications | USB |
| File formats | G-Code or Wireless Electronic Handwheel or C language |
| Table dimensions (mm) | 152x152 |
| Travel dimensions (mm) | 240x240x70 |
| **XY-direction (Forward Step & Side Step)** | |
| Required resolution for forwarding step and side step (mm/step), mm | 0.003 |
| **Z-direction (Layer Depth)** | |
| Required resolution (mm/step) | 0.003 |
| **Total cost to build SLS prototype system** | |
| Cost | $10,000 |

## 4.2 Laser Positioning System

A laser positioning system with size (12in × 12in) contains two axes, X axis and Y axis, see Figure 32. Bearings are used at the left and right of laser holder to get smooth movement. The laser secures on the XY plane to produce the required part. Designers are looking to design and build gantry systems which have high-speed movement, high accuracy, and easy to fix. SolidWorks 2015 used to design all subsystems of the laser positioning system. Also, the gantry holders and laser holder are manufactured by using 3D printer.

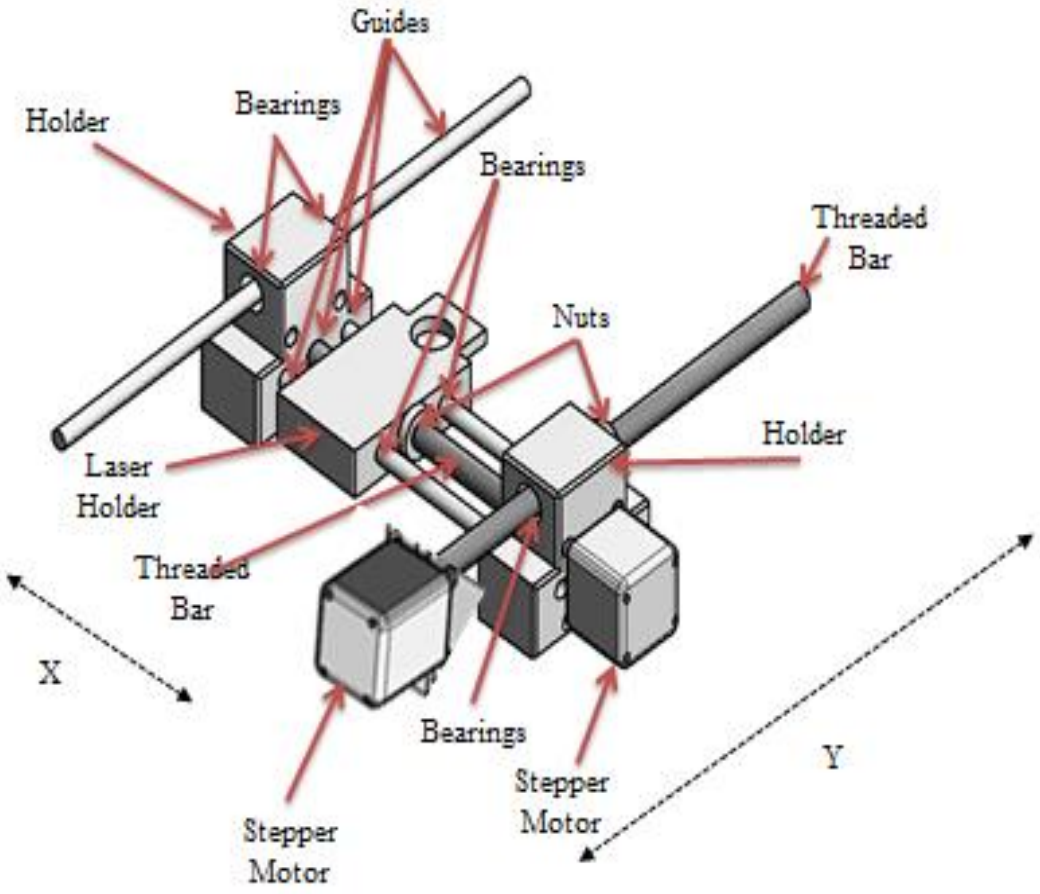


Figure 32. Laser positioning system of SLS system

Table 5 shows quantity of parts that used to build the gantry system, eight parts with different materials used in gantry system. some of parts used platic or rubber because they are easy to build and not expensive if compared with other materials. 3D printer used to produce holders, laser holder and system covers.

Table 5. Laser positioning system parts

| # | Part Name | Material | Quantity |
|---|---|---|---|
| 1 | Holder | Plastic | 2 |
| 2 | Laser holder | Plastic | 1 |
| 3 | Bearings | Steel | 8 |
| 4 | Guides | Steel | 3 |
| 5 | Threaded bar | Steel | 2 |
| 6 | Nut | Rubber | 2 |
| 7 | Stepper Motor | - | 2 |
| 8 | Coupler | Steel | 2 |

The accuracy of the automation system is an important point for the system specifications. The accuracy of the SLS system means forward step and side step in X and Y direction respectively. In this research, the minimum step (Δl) in X and Y directions is equal to 0.003mm calculated by

$$\Delta l = \frac{PB}{360} . \frac{\theta_s}{i} \text{ mm/step} \quad (4.1)$$

where $\theta_s$ is equal to 1.8($^o$/step), i is equal to 1, and PB is equal to 0635 (mm/rev).

### 4.3 Laser System

The laser power W/mm$^2$ has been calculated to melt PA650 powder depending on: powder specific heat capacity KJ/kg K; powder melting temperature $^o$c; powder density g/mm$^3$; power thermal conductivity w/mk; powder thermal diffusivity, m$^2$/s; absorptivity;

temperature of the powder surface k; processing times; and temperature penetration depth m. The laser power required to fuse the PA650 powder is calculated by using [60]

$$I = \frac{K_s T_w(t)}{A_s \delta_s(t)} \tag{4.2}$$

Calculation process of the laser power that required to melt powder dependent on thermal properties of PA650 powder that shown in Table 6. The laser power has determined by considering these limitations. Therefore, The PA650 powder needs 9.7W laser to start melting with laser beam equal to 0.42mm.

Table 6. Thermal properties of the PA650 powder that used to calculate laser power [66, 67, 68]

| # | Symbol | Units | Parameter | Value |
|---|---|---|---|---|
| 1 | $C_p$ | J/kg×K | Specific heat capacity | 2500 |
| 2 | M | $^oC$ | Melting temperature | 180 |
| 3 | ρ | $kg/m^3$ | Density | 460 |
| 4 | $K_s$ | W/m×K | Thermal conductivity | 0.37 |
| 5 | $A_s$ | Constant | Absorptivity | 0.5 |
| 6 | $T_w$ (t) | K | Temperature of the surface | 453 |
| 7 | $\alpha_s$ | $m^2/s$ | Thermal Diffusivity | $3.217\times10^{-7}$ |

The laser specifications used are: laser size 33 x 33 x 75mm, laser wavelength 450nm, laser power is 10W, voltage DC is 12V, working temperature is +10 ~+40, driver module is TTL.

In addition, the reason of purchase this kind of laser with this specifications because sometimes it is very hard to find a laser beam diameter exactly the same as what the researchers have calculated. Laser beam will change from 4mm to 0.42mm to match the laser beam diameter that designed. Therefore, one lens used to reduce beam diameter to get a same laser beam diameter has calculated prevously. The specifications of the lens that have been utilized in this study are the lens diameter (9 mm), effective focal length EFL (90 mm), back focal length BFL (88.68mm), radius R1 (46.51 mm), edge thickness ET (1.78 mm) and center thickness CT (2 mm), such as shown in Figure 33.

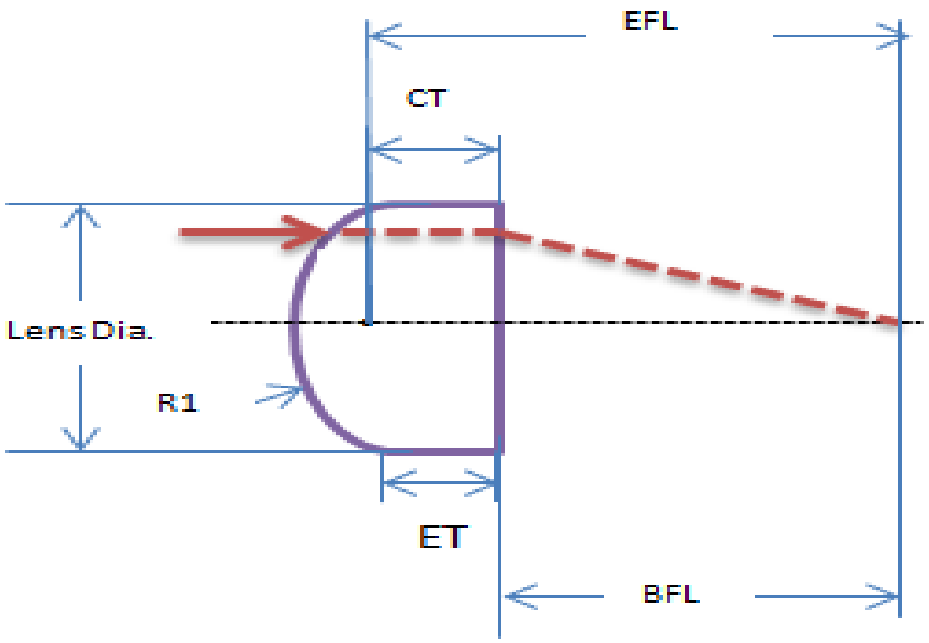


Figure 33. 9.0mm Dia. X 90.0mm FL laser lens

Figure 34 shows a holder and lens that is used to focus laser. The holder consists of two parts and can connect together after putting a lens inside the first part of the holder. Also, the laser system connects with the lens holder.

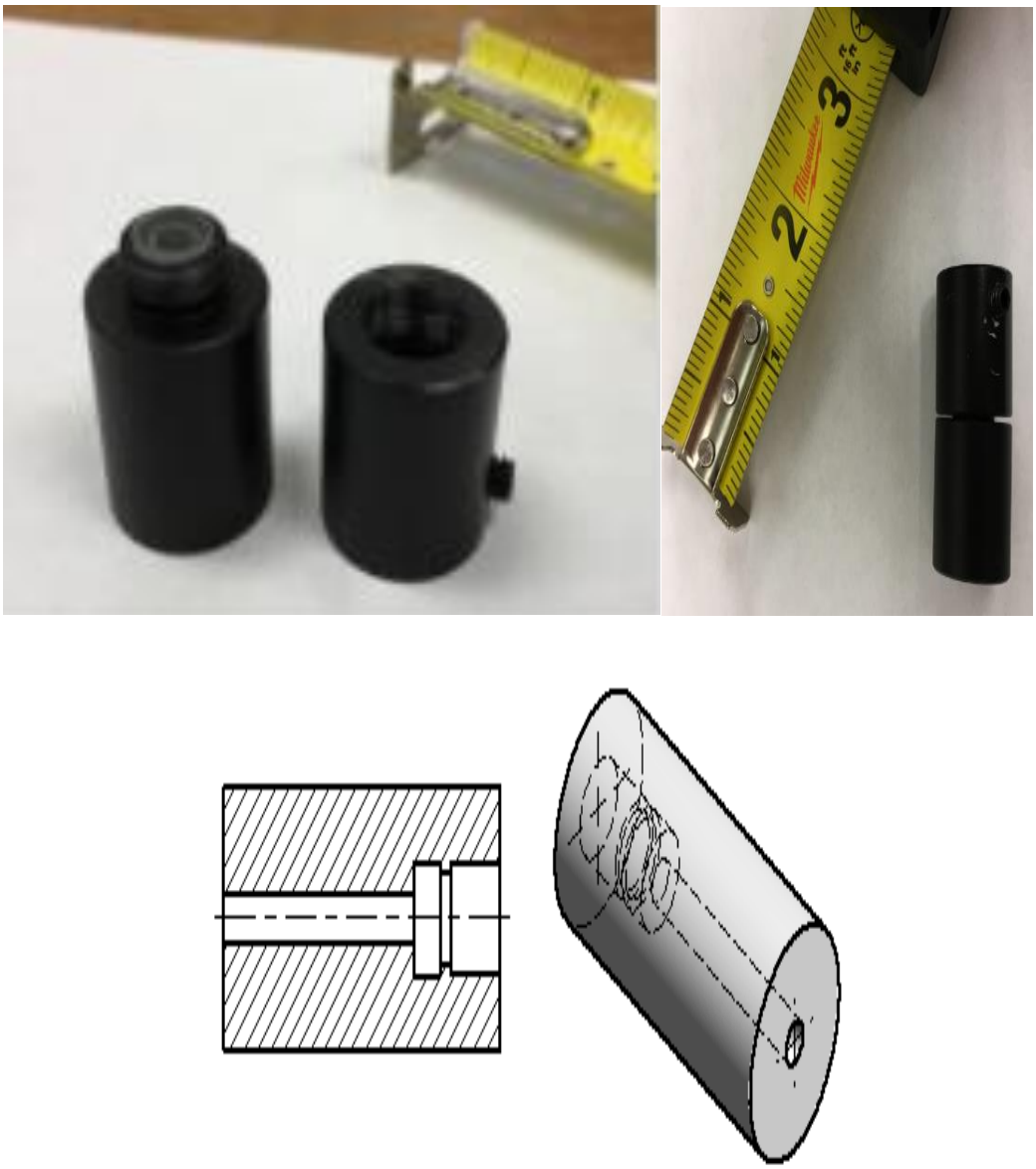

Figure 34. Laser lens holder

### 4.4 Powder Distribution System

The powder distribution mechanism with size (11in × 11in) consists of a powder container with size (8in × 1.25in × 2.5in), threaded bar, melting table with size (4.5in × 5in), and stepper motor, see Figure 35. The powder feeder has a container, and the

powder will be put in the container manually. After putting the powder in the container the powder feeder moves on the XY plane to distribute powder on the SLS table. The second part of the powder distribution mechanism is the threaded bar that will drive the powder container forward and backward. The container will carry a powder, so when fusing the first layer of powder the platform moves down to feed the second layer by the powder feeder and this process will be repeated until complete a part is formed. For this work, the powder feed was chosen at 200mm/s. Also, the CAM software is used to control speed of the powder distribution mechanism.

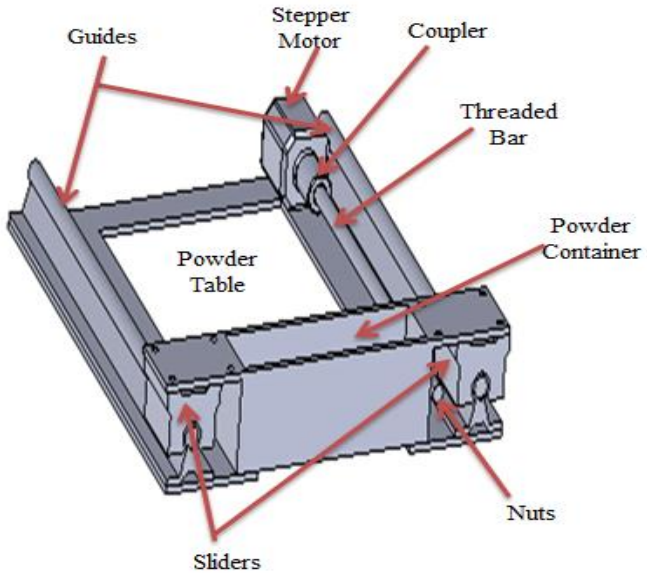


Figure 35. Powder distribution mechanism

Table 7 shows quantity of parts that used to build the powder distribution mechanism system, the powder distribution system is designed to be easy to use and easy to fix. 3D printer used to produce powder container.

Table 7. Powder distribution parts

| # | Part Name | Material | Quantity |
|---|---|---|---|
| 1 | Container | Plastic | 1 |
| 2 | Slider | Steel | 2 |
| 3 | Guides | Steel | 2 |
| 4 | Threaded bar | Steel | 2 |
| 5 | Nut | Steel | 1 |
| 6 | Stepper Motor | - | 1 |
| 7 | Coupler | Steel | 1 |

### 4.5 Structure and Enclosure

The prototype SLS system uses a frame built from a combination of steel structural components and plastic components. Table 8 shown the bill of materials for the structure. The prototype views of SLS design are shown in Figure 36.

Table 8. Bill of material for the structure

| # | Part Name | Material | Quantity |
|---|---|---|---|
| 1 | Bearings | Steel | 3 |
| 2 | Stand of Powder Table | Steel | 1 |
| 3 | Guides | Steel | 2 |
| 4 | Nut | Rubber | 1 |
| 5 | Frame | Steel | 1 |

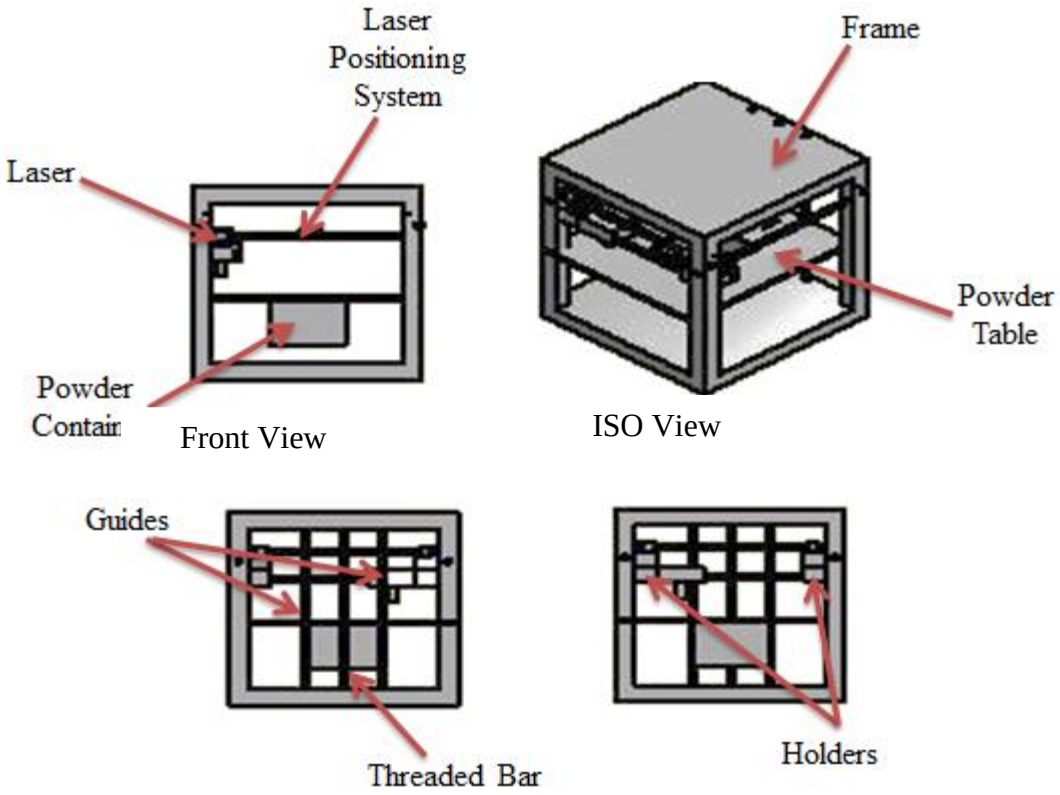


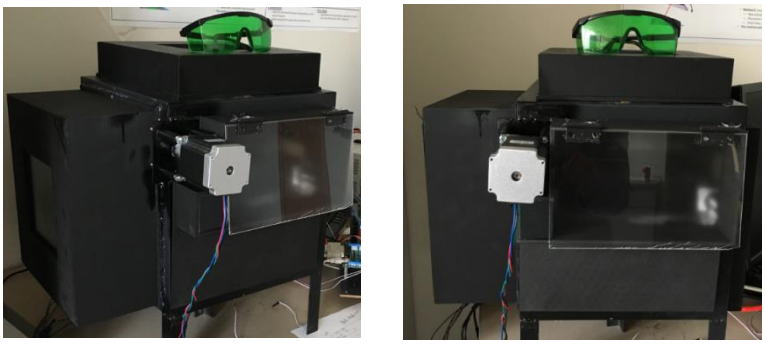

Figure 36. SLS system views and the prototype SLS system

## 4.6 Electronic and Control System

The electronics platform drives all the actuators of the SLS system. The SLS system includes many different components working together to build the 3D parts. These components include a microprocessor, platform heater, motor drivers, stepper motors, high power laser and power supply [58], see Figure 37.

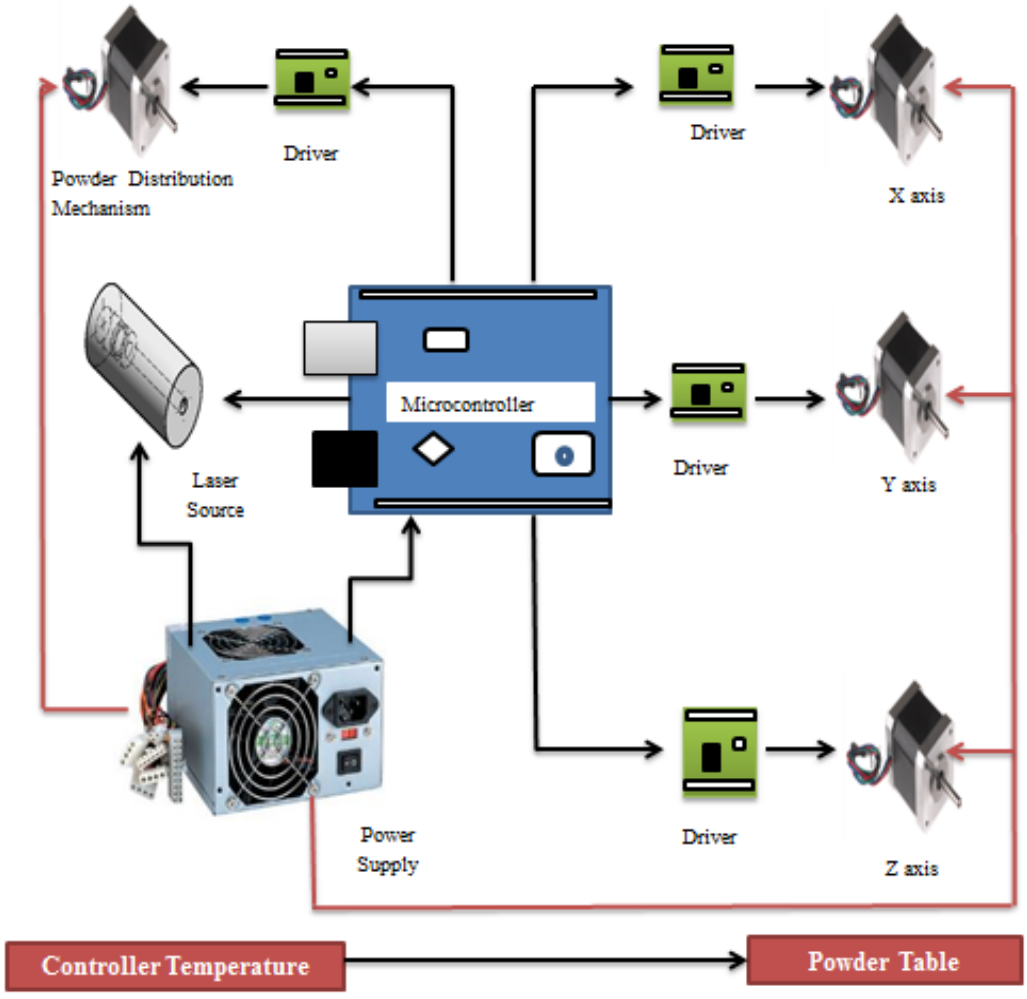


Figure 37. Electronic components of SLS system

Figure 38 shows a diagram of the electronic control system of stepper motor and microprocessor. All the stepper motors and high power lasers connected to the microprocessor and a checkup process of the electronic system control will use interface program and a manufacturing simulation program. The microprocessor consists of five channels of stepper motor drivers, and USB port used to connect with PC by using a cable connection. Each channel of stepper motor has five wires. The first one is for step, second one is for direction, third is for ground, and last one is for power (5v).

There are four stepper motor drivers. Each driver has two connections, the first one is for the microprocessor and the second one is for the stepper motor. Four stepper motors are used to run three manufacturing axes, and the four axis is used to run powder distribution mechanism with 24v power.

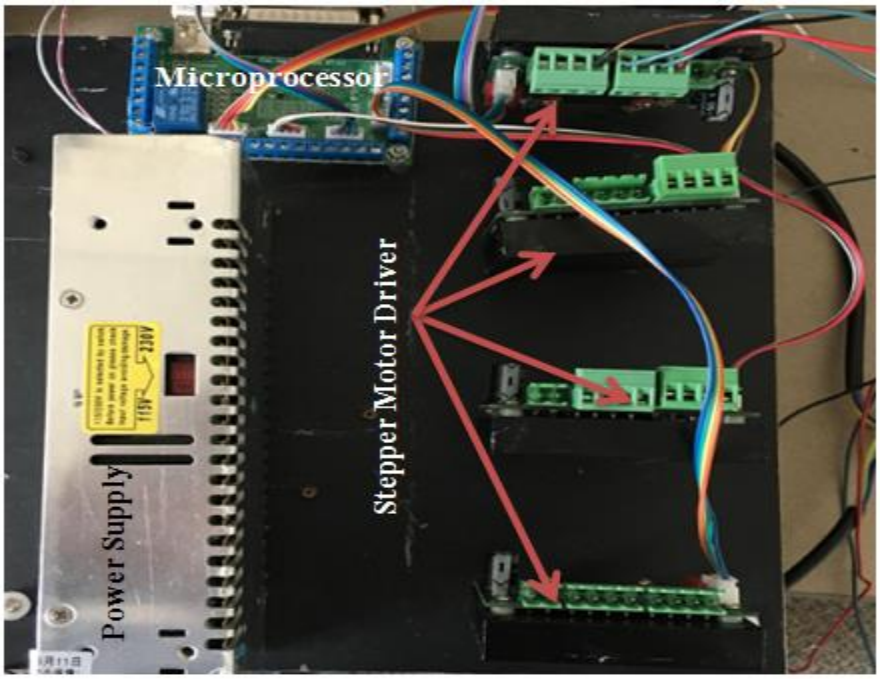


Figure 38. Electronic control system

## 4.7 Integration of Computer Aided Manufacturing (CAM)

The prototype SLS system is connected with a PC and the setup process of all actuators was between the CAM software and the PC. The running operation of the system was checked before starting to produce the parts, such as axis movement, system speed, platform temperature, and laser ON/OFF of the SLS system.

Checking process will happen before running the prototype SLS system. Figure 39 shows the validation flowchart of the manufacturing process of the SLS operation.

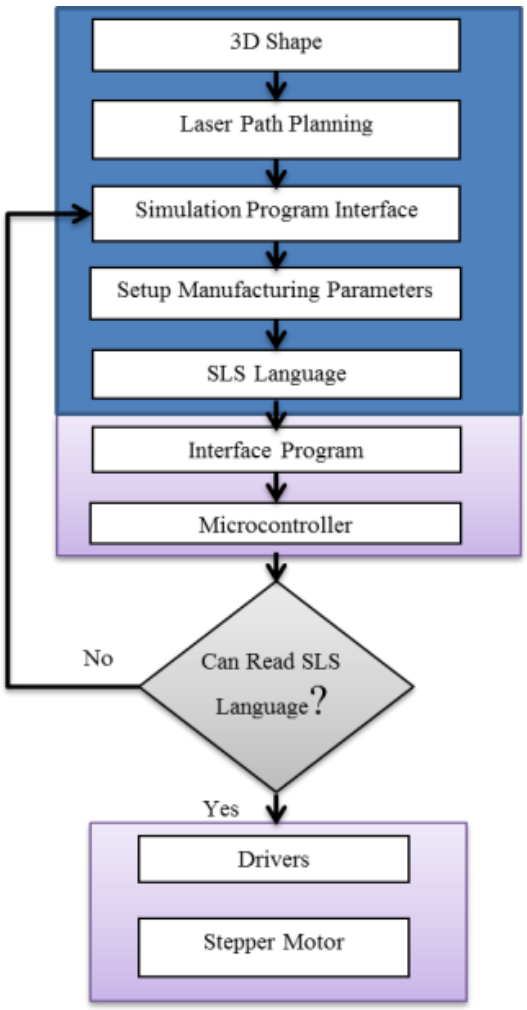


Figure 39. Flowchart of manufacturing process validation

The laser tool path of the 3D part was checked by using Mach3, and this program is CAM program used to feed manufacturing languge to prototype SLS system. The Mach3 used in this research because the microprocessor works on this CAM program. Also, Mach3 can control all the system, such as max or min speed, feed rate, ON/OFF, emergency shut down, check laser tool path, etc. Figure 40 shows Mach3 program front page.

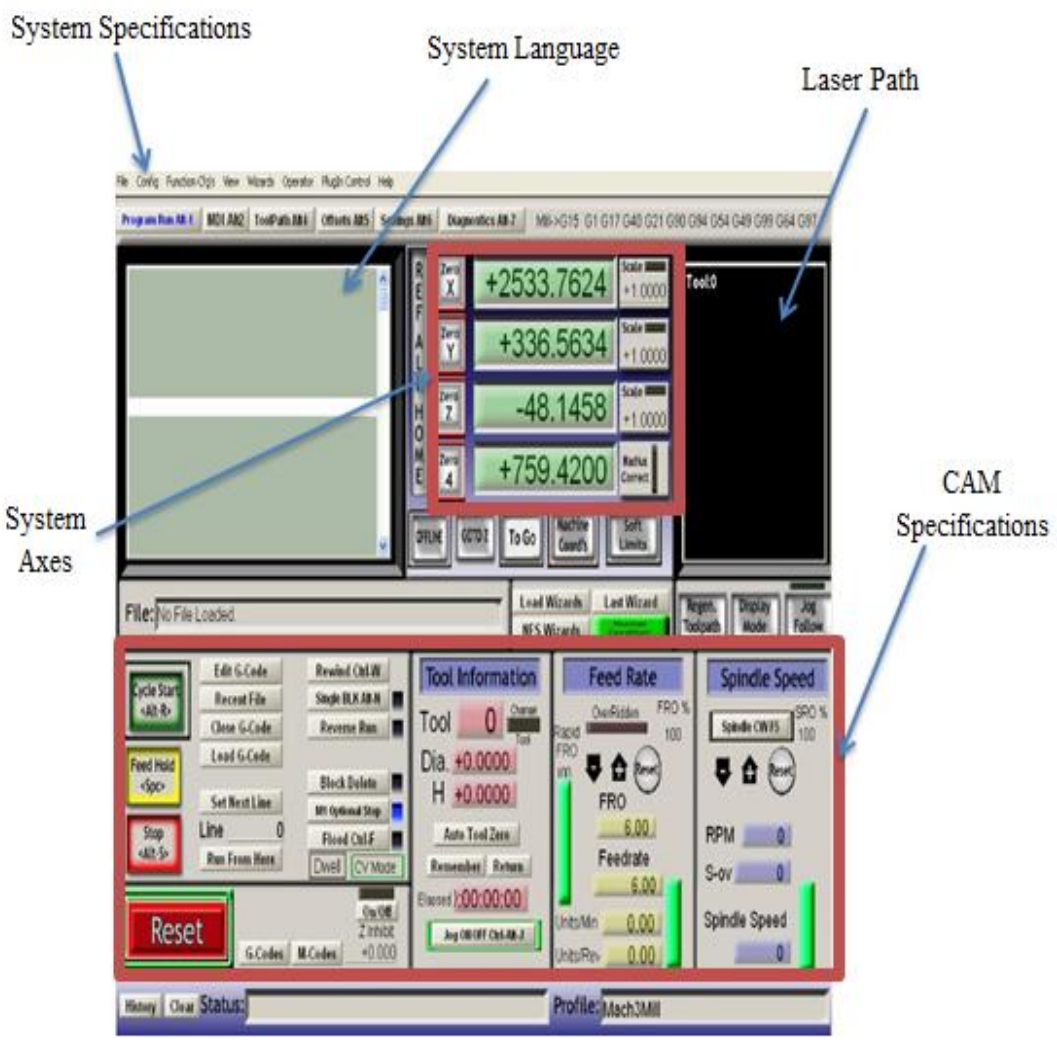


Figure 40. CAM simulation program front page

## 4.8 Material Selection

The powder utilized in this study consists of 90% carbon steel powder and 10% carbon, wax, resin and nylon powder (PA 650). The powder was preheated between 150 $^{o}$C to 170 $^{o}$C then a high power laser was applied to melt the powder. The interconnection between the grains happened by helping the PA650 material. Figure 41 shows the powder grains before and after the melting process.

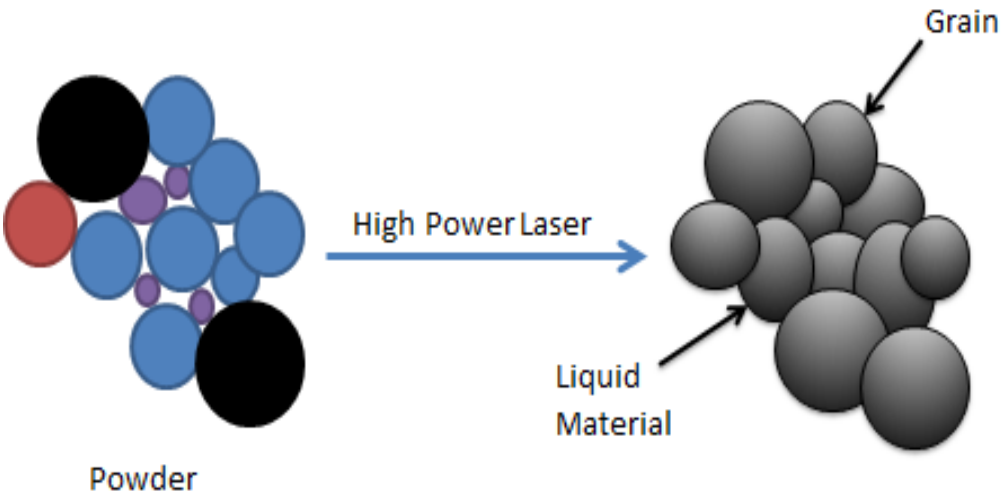


Figure 41. The powder grains before and after melting

An environment scanning electron microscope (ESEM) was used to check powder that used to build parts by using the prototype SLS system in Biomedical Engineering Department/Lawrence Technological University, see Figure 42.

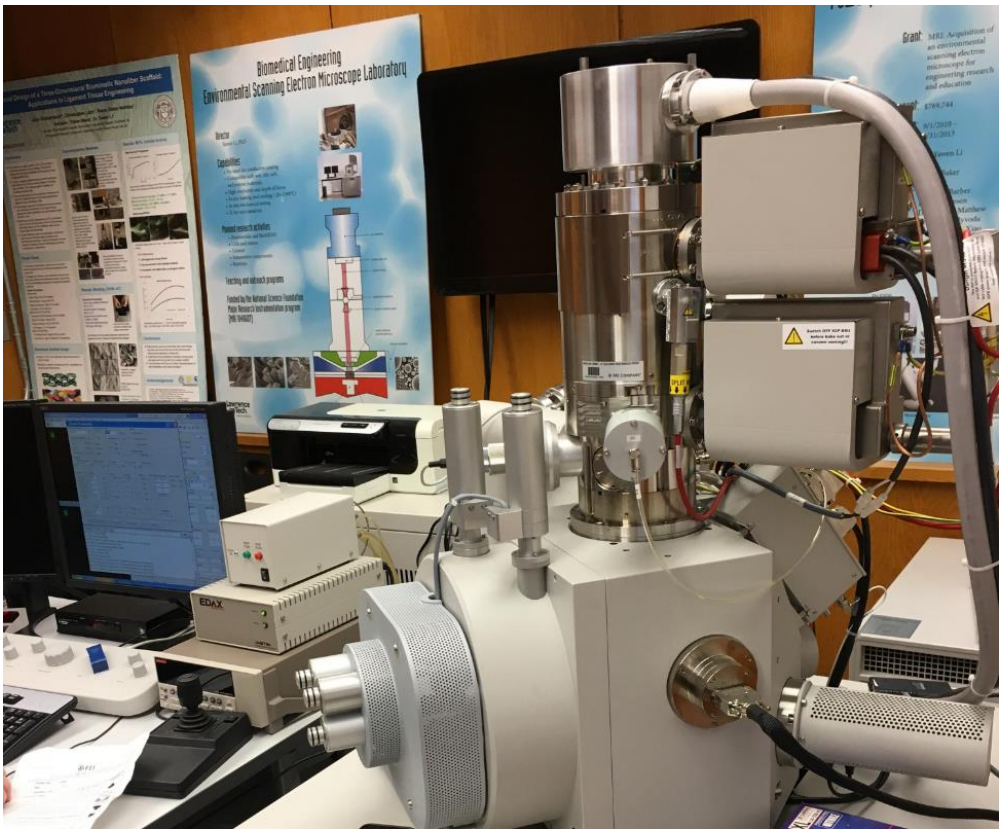


Figure 42. An environment scanning electron microscope (ESEM)

Figure 43 shows the microscope results of carbon steel powder used in this research. Table 9 defines the chemical composition of the powder. The table consists of elements, weight percentage, and atomic percentage for each item. Each element has a different energy, and by depending on this energy, the element type will discover. The reason of using the ESEM is to check powder components, match with powder data sheet, and select a proper laser power before starting the manufacturing process. If powder does not match the powder data sheet that will lead to produce parts that have bad quality because each material has a different melting point and the laser used has a specific energy. Therefore, the part produced will be over or under melting and that will effect part quality.

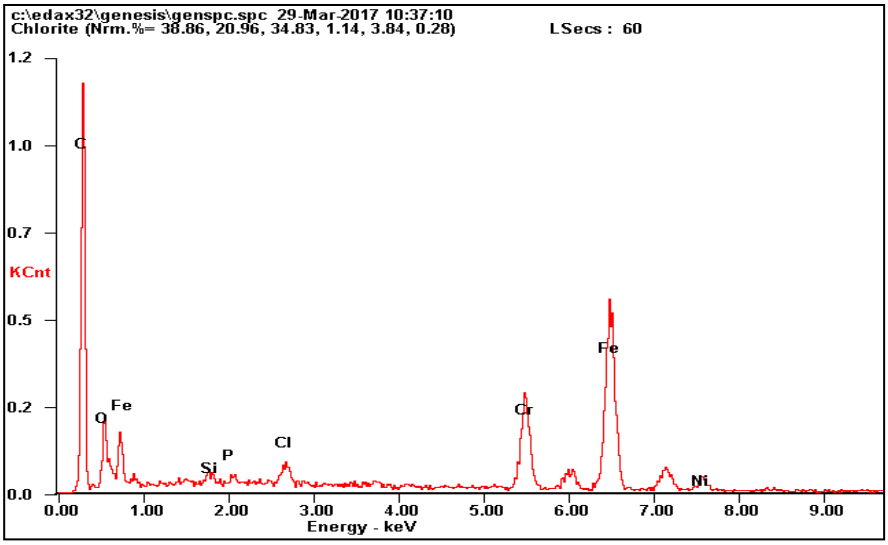


Figure 43. Electron microscope result of the powder

Table 9. Chemical composition

| Element | Weight Percentage% | Atomic Percentage % |
|---|---|---|
| C | 49.16 | 75.95 |
| O | 07.82 | 09.07 |
| S | 00.60 | 00.40 |
| P | 00.36 | 00.22 |
| Cl | 01.11 | 00.58 |
| Cr | 09.48 | 03.38 |
| Fe | 28.71 | 09.54 |
| Ni | 02.75 | 00.87 |

Initial experiments were run before starting optimization to determine powder mixture and manufacturing parameters that will effect part quality. Each sample has different

quality, some have porosity or warp or disconecct layers, see Table 10. These results will be used in the following chapter.

Table 10. Experiments used to study effects powder compound and manufacturing parameters

| # | Powder Compound | Manufacturing Parameters | Observed Defects |
|---|---|---|---|
| 1 | %7C, %93 PA650 | (1mm) Side step, (100 mm/s) speed, (55mm) length | Over melting, warping, and crack |
| 2 | %7C, %46.5 PA650, %46.5 carbon steel | (1mm) Side step, (100 mm/s) speed, (55mm) length | Over melting and warping |
| 3 | %7C, %46.5 PA650, %46.5 carbon steel | (2mm) Side step, (100 mm/s) speed, (55mm) length | Porosity and disconnect between layers |
| 4 | %7C, %46.5 PA650, %46.5 carbon steel | (1.5 mm) Side step, (100 mm/s) speed, (55mm) length | Warping and disconnect between layers |
| 5 | %7C, %46.5 PA650, %46.5 carbon steel | (1.5mm) Side step, (150 mm/s) speed, (55mm) length | Warping and overlapping |
| 6 | %7C, %46.5 PA650, %46.5 carbon steel | (1mm) Side step, (150 mm/s) speed, (55mm) length | Warping and crack |
| 7 | %7C, %46.5 PA650, %46.5 carbon steel | (1.5mm) Side step, (200 mm/s) speed, (55mm) length | Warping |
| 8 | %7C, %25 PA650, %75 carbon steel, %3 wax | (1mm) Side step, (150 mm/s) speed, (55mm) length | Warping and Surface roughness |
| 9 | %7C, %25 PA650, %75 carbon steel, %3 wax | (1mm) Side step, (180 mm/s) speed, (55mm) length | - |
| 10 | %7C, %25 PA650, %75 carbon steel, %3 wax | (1mm) Side step, (180 mm/s) speed, (55mm×90mm) length | Warping |
| 11 | %7C, %25 PA650, %75 carbon steel, %3 wax | (1mm) Side step, (180 mm/s) speed, (55mm×90mm) length | Warping and crack |
| 12 | %10 (C,PA650, wax, resin), %90 carbon steel | (1mm) Side step, (180 mm/s) speed, (55mm×90mm) length | - |

## 4.9 Safety system

The safety system is used to protect employees that work on the SLS prototype system. The safety machine includes: easy shut down of the system for any emergency case. A protection casing or guard fence is used to protect researchers from risks (flying objects), noise during running the system, and interference during moving actuators. Also, below are some rules use to protect employees [69]:

- Wear laser safety glasses (comes with the laser) during running the system to protect researchers eyes because high power laser is used to melt powder.
- Cover long hair during running the system.
- Keep hands away during printing process.
- Nitrile gloves.
- Do not: wear loose clothing, wear jewelry, and touch the system parts during running the system.

## 4.10 System Validation

This section of the research will discuss the validation procedure for the prototype SLS system. The validation processes will check all the subsystems using sensors and simulation programs.

Forward and side steps will be validated to check the minimum steps and to check how much deviation there is between designed and measured steps. Laser positioning system vibration will be validated to reduce parts defects. Validation of laser beam diameter is applied to check how much difference there is between design and measure of laser beam diameter. Stepper motor speed is the last part of the validation process. Speed control process will be checked by using a manufacturing simulation program.

### 4.10.1 Laser Positioning System

Some of validations processes will be done in this section to check how much deviation has the laser positioning system and how this deviation is going to affect the part quality. First validation is to measure runout on X and Y axes of laser positioning system during running the prototype SLS system. Due to runout, the laser position applies on powder bed will change and that will produce error during manufacturing process. Table 11 shows the runout of the laser positioning system and the measuring process used a dial indicator. Therefore, parts manufacture by using the prototype SLS system will have deviation and these will affect on part length and width. Maximum error due to runout is equal to 0.381 mm in X direction and 0.762 mm in Y direction. These errors are very large relative to the designed system of 0.003 mm due to the low cost

components that used to build the laser positioning system. Future work should focus on improving this error.

Table 11. The runout of laser positioning system

| # | Axis | Runout |
|---|---|---|
| 1 | X | 0.381 mm |
| 2 | Y | 0.762 mm |

Second step of laser positioning system is validate minimum forward step and side step can produce by the prototype SLS system. Figure 44 is a validation flowchart steps followed to validate a minimum step. An interface program, stepper motor, stepper motor driver and Arduino will be used to complete validation process. The interface program has number of pulses equal to 5mm will control a motion distance of the laser positioning system with a motor step angle equal to 1.8$^{o}$/step and a threaded bar pitch equal to 0.635mm. After the laser positioning system stopped the distance that the laser positioning system moved was measured. After running the system the minimum step measured was 0.003mm.

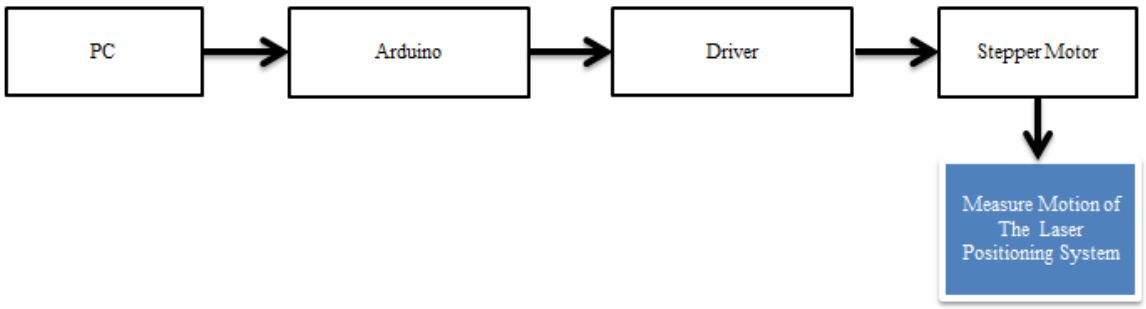


Figure 44. Forward and sidestep validation flowchart

Two experiments were used to check the resolution of the SLS prototype system; see Table 12. Because X and Y axes used the same motor and threaded bar, resolutions are assumed to be identical. The validation process of 5mm distance had an error equal to 0.000625mm, and this this error is only 20% of a step. For 10mm distance had an error equal to 0.00125mm, also this error is only 41% of a step. These errors are consistent with rounding the number of pulses.

Table 12. Data used to validate the laser positioning system

| # | Distance (mm) | Pulses needed | Pulses used | Distance (mm) |
|---|---|---|---|---|
| 1 | 5 | 1574.803 | 1575 | 5.000625 |
| 2 | 10 | 3149.606 | 3150 | 10.00125 |

Figure 45 shows the validation diagram used to validate the gantry system vibration in X, Y, and Z directions. The accelerometer type 8692C50, SN C109475 was used to check the system vibration after connecting it to the amplifier KISTLER type 5134. Data recording of the accelerometer will be checked after connecting the amplifier to the oscilloscope DSO-X 2012A.

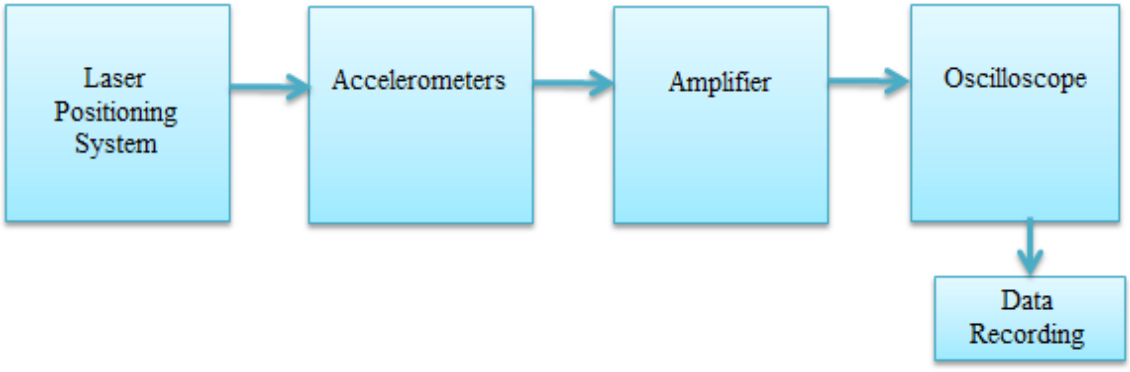


Figure 45. Validation diagram of the SLS vibration

The accelerometer was calibrated by applying 1g by using a PCB 394C06 handheld shaker device before start recording the wave data. The oscilloscope recorded amplitude equal 2.81V. This calibration of amplitude value with other parameters will use to calculate the manufacturing deviation for parts that manufactured by prototype SLS system. Calibration waveform and handheld shaker shown in Figure 46.

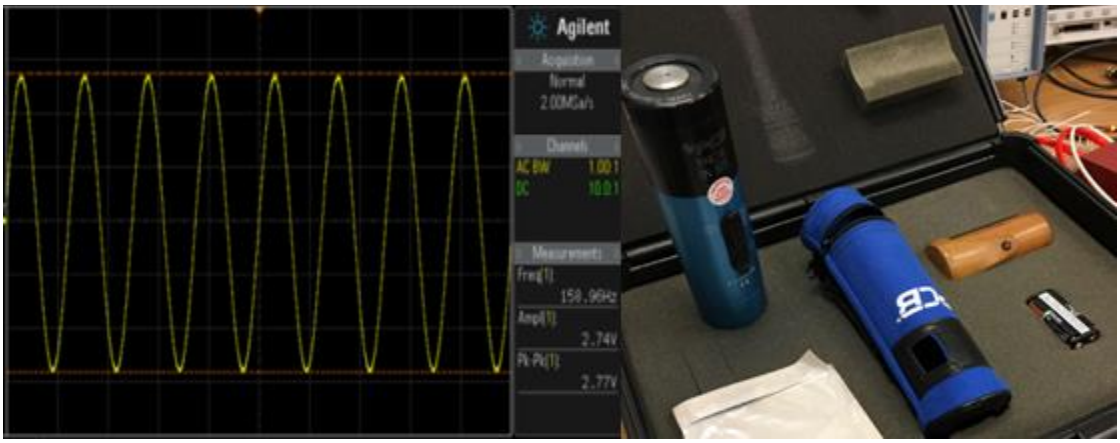


Figure 46. Calibration signal of the accelerometer by using Handheld Shaker

The vibration was measured in X and Y directions with five different speed values for each direction. The reason for recording the frequency is to calculate how much manufacturing error, which is going to effect part quality, happens during running the prototype SLS system. Assume a sinusoidal vibration with measured acceleration specified by A (m/s$^2$), $f$ (Hz), and $t_s$ (s). The acceleration is given by

$$\ddot{x} = A\sin(2\pi f t_s) \tag{4.3}$$

Integrating twice, the displacement is given by

$$x = \frac{A}{(2\pi f t)^2}\sin((2\pi f t_s)) \tag{4.4}$$

Thus, the maximum tool path error is given by

$$x_{max} = \frac{A}{(2\pi f t_s)^2} \tag{4.5}$$

Maximum tool path error due to vibration in X direction is 0.736 µm when speed of the laser positioning system equal to 170 mm/s and Y direction is 0.012 µm when speed of the laser positioning system equal to 190 mm/s, see Table 13. These are significantly smaller than one step.

Table 13. Frequency and amplitude of laser positioning system in X and Y direction

| | **Linear Speed of Laser Positioning System (mm/s)** | **150** | **160** | **170** | **180** | **190** |
|---|---|---|---|---|---|---|
| **X-Direction** | Frequency (Hz) | 230 | 236 | 240 | 255 | 275 |
| | Amplitude ($m/s^2$) | 0.516 | 0.736 | 1.672 | 1.779 | 1.957 |
| | Maximum Tool Path Error (µm) | 0.247 | 0.335 | 0.736 | 0.693 | 0.656 |
| **Y-Direction** | Frequency Hz | 841 | 880 | 955 | 1036 | 1040 |
| | Amplitude ($m/s^2$) | 0.185 | 0.341 | 0.345 | 0.348 | 0.530 |
| | Maximum Tool Path Error (µm) | 0.006 | 0.011 | 0.009 | 0.008 | 0.012 |

### 4.10.2 Laser Validation

For the laser validation , the first step is to measure laser power. The PM100D sensor is used to check the power of the laser by applying laser on a laser power sensor. After checking process, the laser power was 9.7W, see Figure 47.

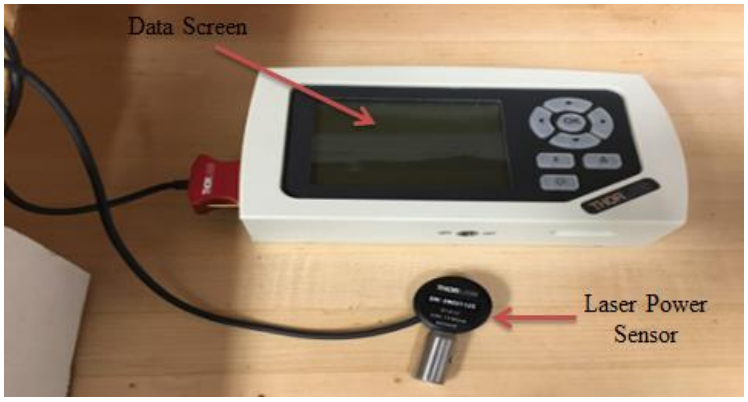


Figure 47. PM100D sensor that used to check laser power

Figure 48 shows two area affected by laser. First area is the melting line and second area is heat affected zone around melting line [70]. These areas will affect on the part quality because the heat affected area will melt during next step and that will produce bad melting process and increase defects that happen during producing parts. Equation below is to show the heat flux area around the thermal source.

$$T(r,t) - T_O = \frac{Q}{4\pi kt}\exp\left[-\frac{r_c^2}{4\propto t}\right] \quad (4.6)$$

where units of Q is (J/m), k is (W/mK), t is (s), and $r_c$ is (m)

A

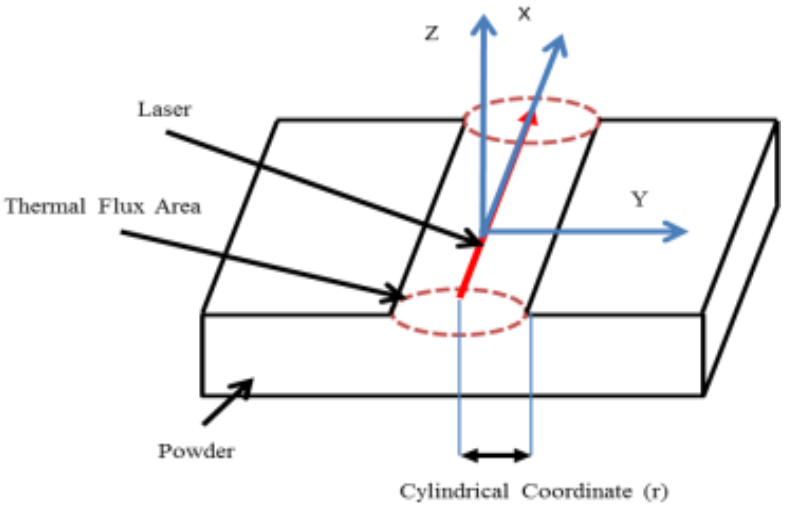


B

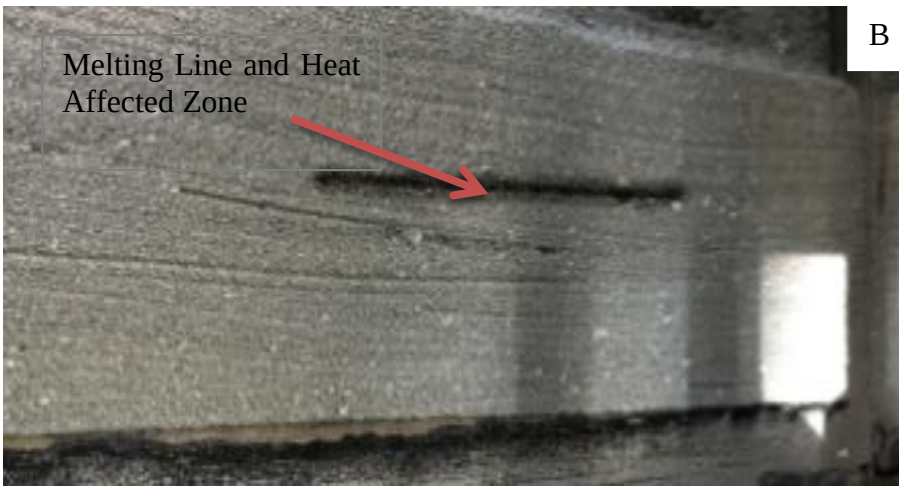


Figure 48. (A) Thermal flux area and cylindrical coordinate (B) Sample to check melting process

Before starting to use the laser, one must check the laser beam shape. So after checking without a lens, the laser cross section profile was not circular. It was very close to triangle. SPIRICON model SP620U was the laser beam diagnostics sensor used with the filters to measure the beam diameter of the laser. Four filters must be used to cut power 9-10 times to minimize the laser power to measure the laser beam diameter because the sensor that is used to measure laser power could not measure high power laser. Table 14 shows the types and quantities of the laser filter. Two filters of ND540A, one filter of ND510A, and one filter of ND520A are used to reduce 10 times of laser power, as shown in Figure 49.

Table 14. Types and quantities of the laser filter

.

| No. | Filter | Quantity |
|---|---|---|
| 1 | ND540A | 2 |
| 2 | ND510A | 1 |
| 3 | ND520A | 1 |

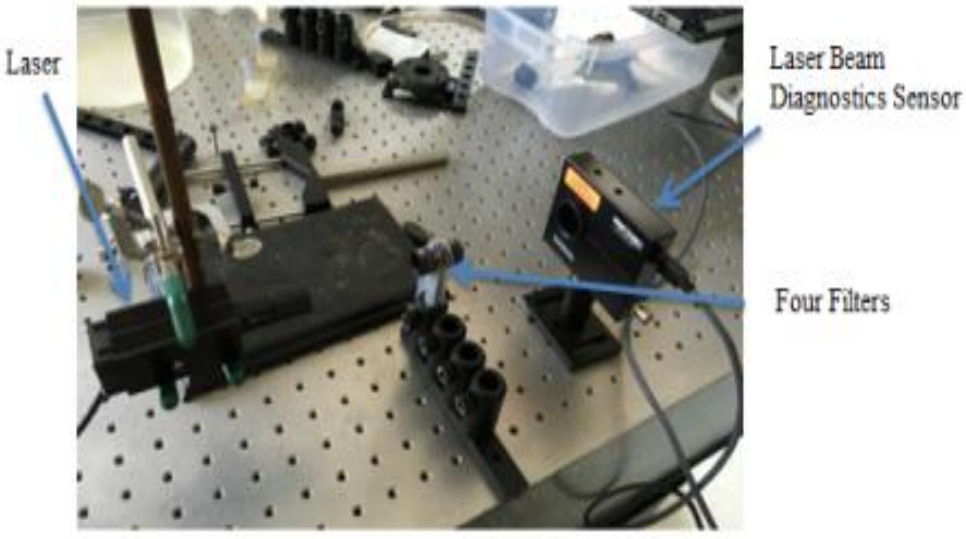


Figure 49. Validation diagram to measure laser beam diameter

Figure 50 demonstrates the image of the laser beam diameter. The laser beam shape was not a circle, but it was very close to an ellipse. The measurement of the laser beam diameter was 0.42 mm in the major axis and 0.038 mm in the minor axis by using D4sigma method. The results measured are acceptable because beam diameter was designed with 0.42 mm.

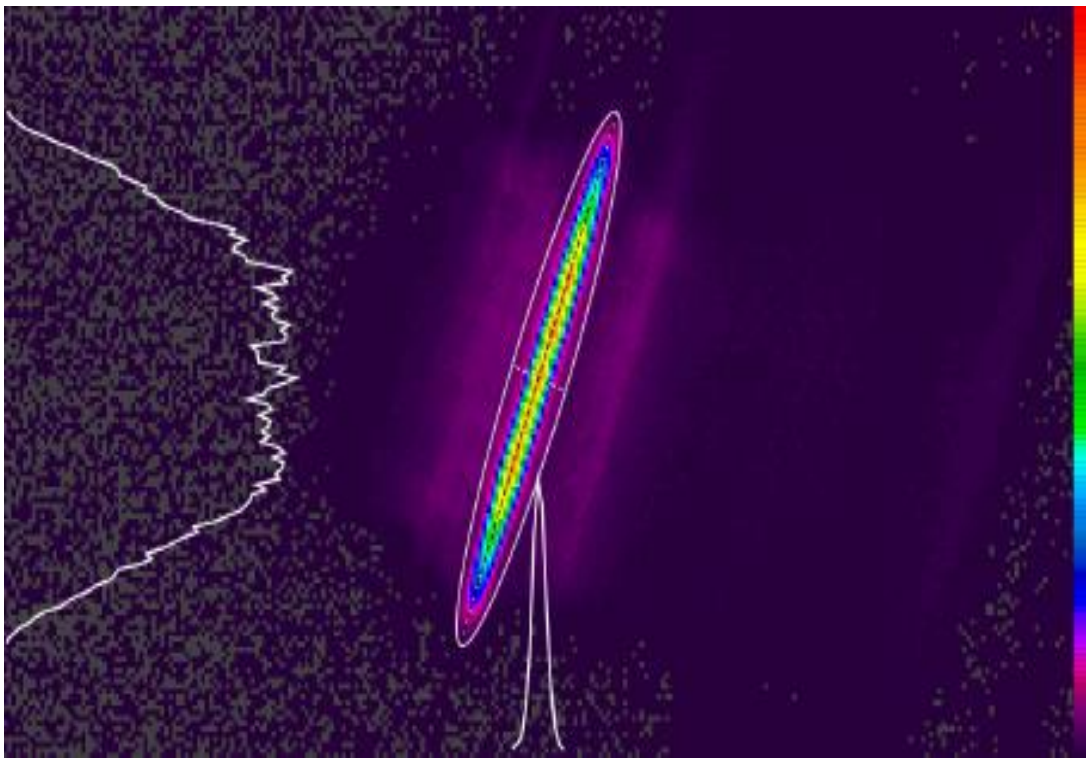

Figure 50. 2D beam display of the laser

### 4.10.3 Stepper Motor Speed Validation by Using LabView Simulation Program

Figure 51 shows encoder, encoder electrical circuit, MyRIO, Tachometer model #HPT-100A, and power supply used to validate stepper motors. The validation process measured stepper motor speed to check how much deviation there was between input and output speed. Input speed was set using the manufacturing simulation program, and output speed was measured using the encoder and MyRIO. Digital Photo Tachometer model #HPT-100A was used to do a double check of the results from encoder and MyRIO.


Figure 51. Validation equipment of stepper motors and hardware that used to validate stepper motor speed

Figure 52 shows the electronic circuit of SLS prototype system that is used to validate motor speed by using encoder, MyRIO, and LabView program.

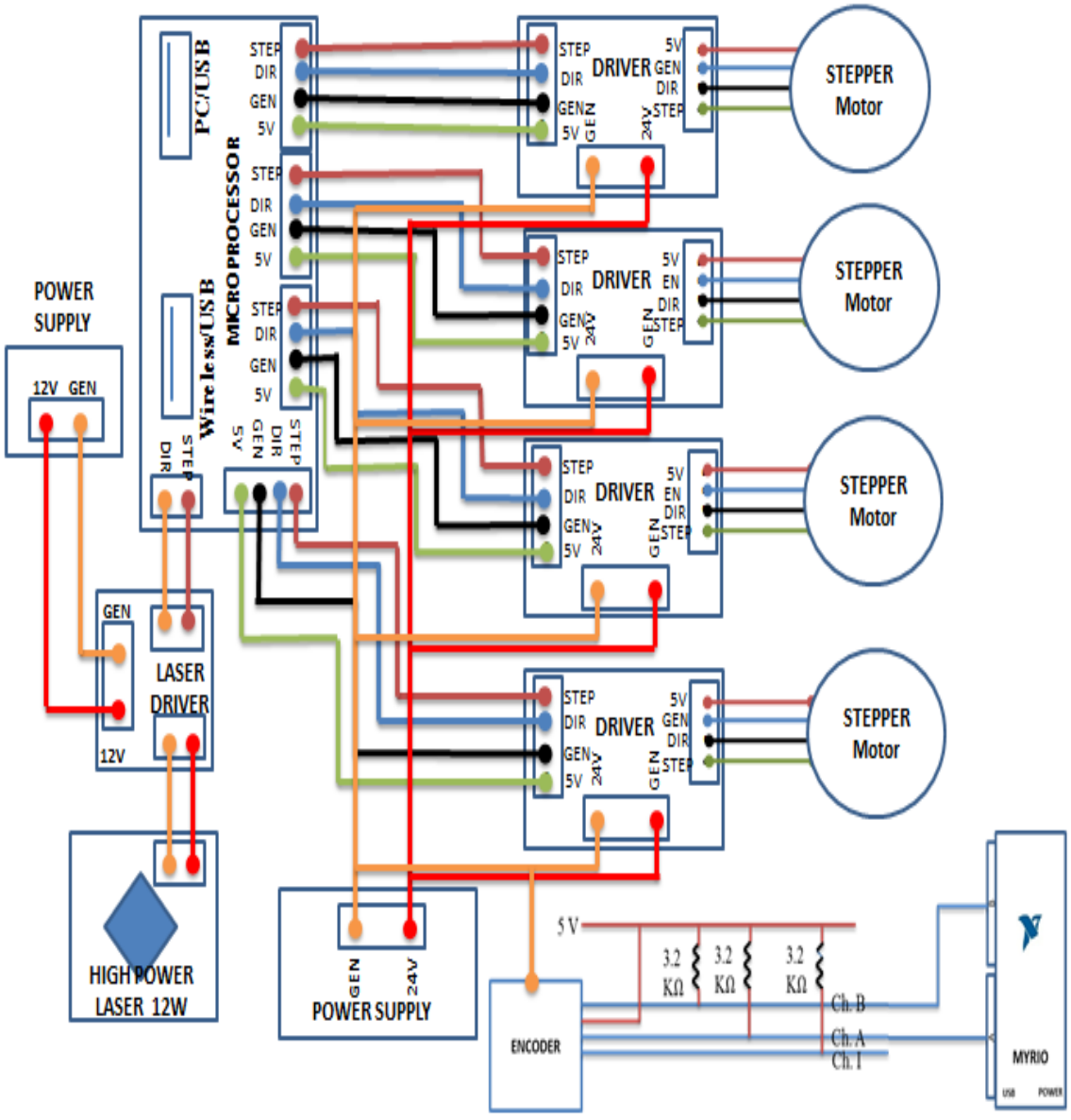


Figure 52. Electronic circuit of SLS system

The encoder sensor consists of a circular plate and signals detector. The encoder type used is Avago-HEDS-5500/5540 and can produce two channels, A and B. Figure 53

shows the signals of the encoder to check the working channels of the encoder before using it to measure stepper motor speed, so the yellow pulse is for channel B, and the green pulse is for channel A.

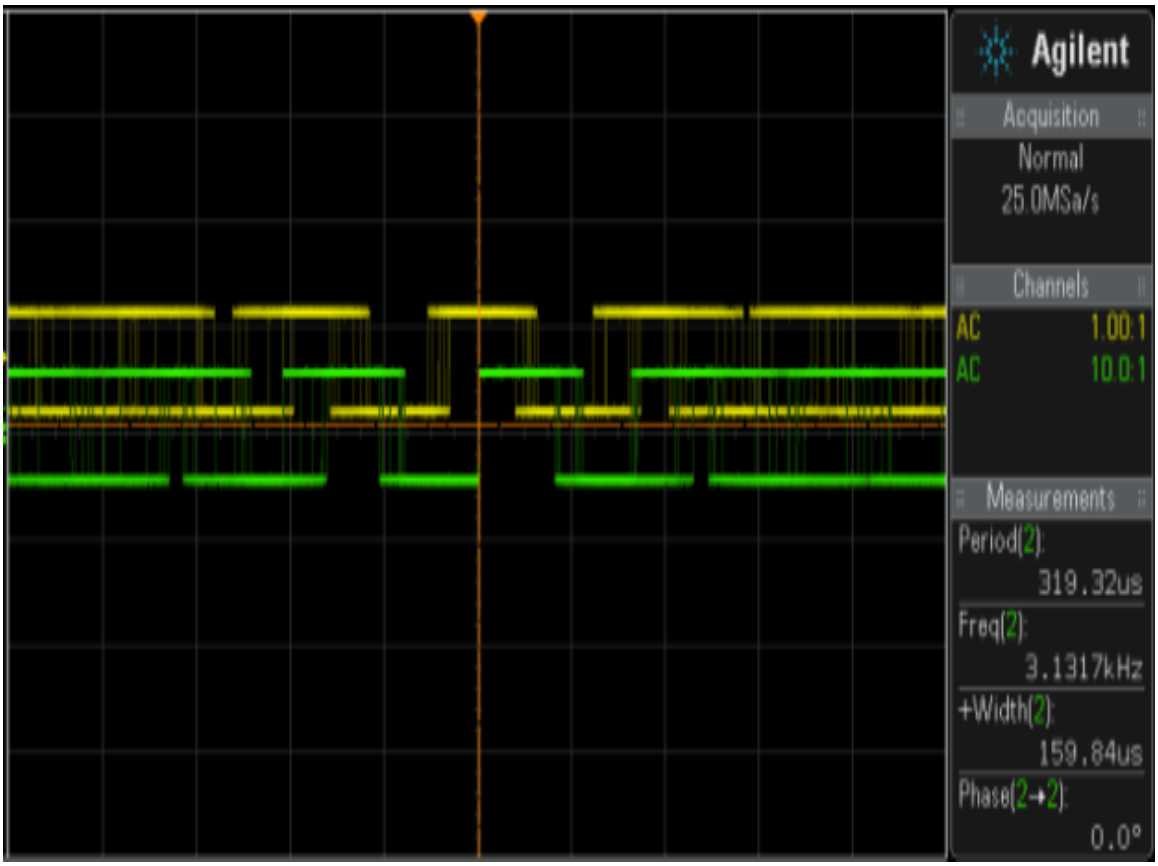


Figure 53. Encoder signals of channel A and B

The MyRIO programmed with LabView was used to validate stepper motor speed. Table 15 explains configuration of the MyRIO.

Table 15. LabView and MyRIO channels

| Part Name | Signal Type | Signal Type | MyRIO Channel | Port | Pin |
|---|---|---|---|---|---|
| Encoder/Signal A | Input | Digital (0-5V) | DIO0 | A | 11 |
| Encoder/Signal B | Input | Digital (0-5V) | DIO1 | A | 13 |
| Motor Control PWM | Output | Digital (0-5V) | DIO4 | A | 17 |
| Ground | | | DGND | A | 16 |

Figure 54 shows stepper motor code to generate PWM voltage. The desired pulse is passed from the real time layer to produce the FPGA layer PWM signal with required duty cycle. The myRIO used DIO4 (CW) and DIO5 (CCW). This is used to check the encoder rotation CW or CCW, to observe the LabView program is working or not.

Figure 55 is LabView code to read channels A and B of the encoder by using MyRIO channels DIO0 and DIO1, also by comparing edges to determine a direction of encoder rotation and position. Figure 56 shows LabView code to measure stepper motor speed by depending on LabView position code and Figure 57 shows front panel to measure stepper motor speed. Five experiments were used to check gantry speed are 150, 160, 170, 180, 190 mm/s, results of the SLS prototype system 150, 160, 170, 180, 190 mm/s. That means the SLS prototype system is accurate and there is no deviation between input and output

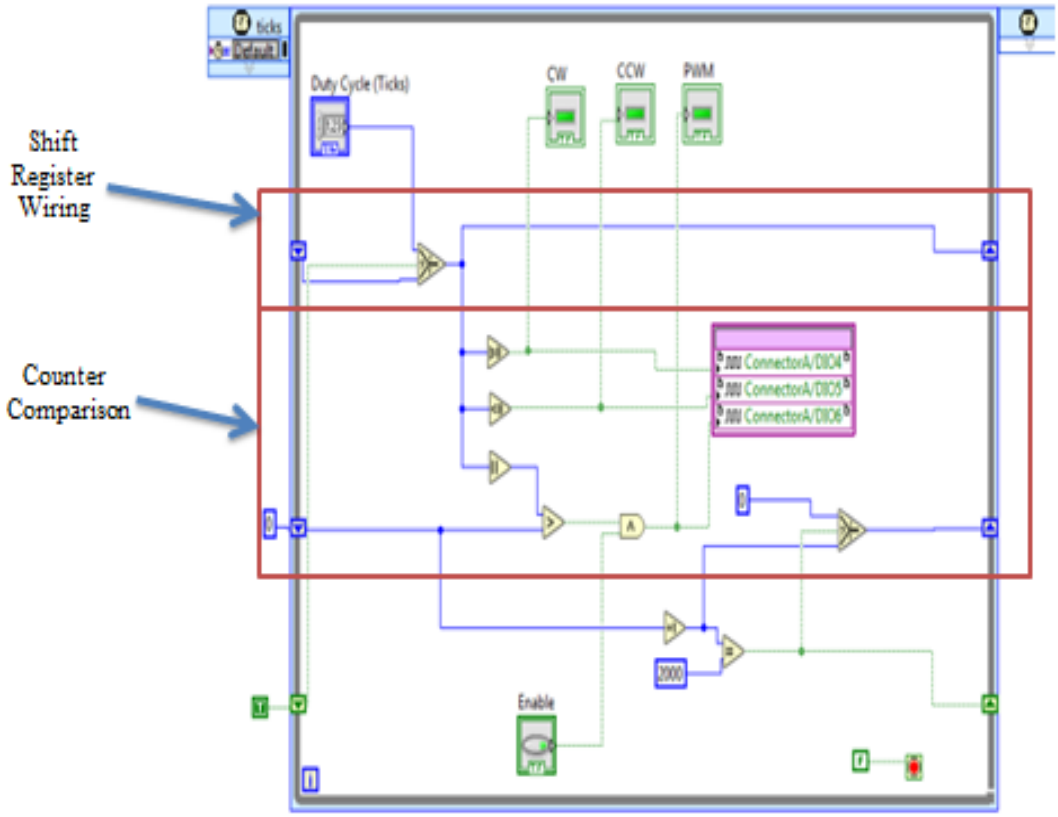


Figure 54. LabView code to check the encoder works CW and CCW

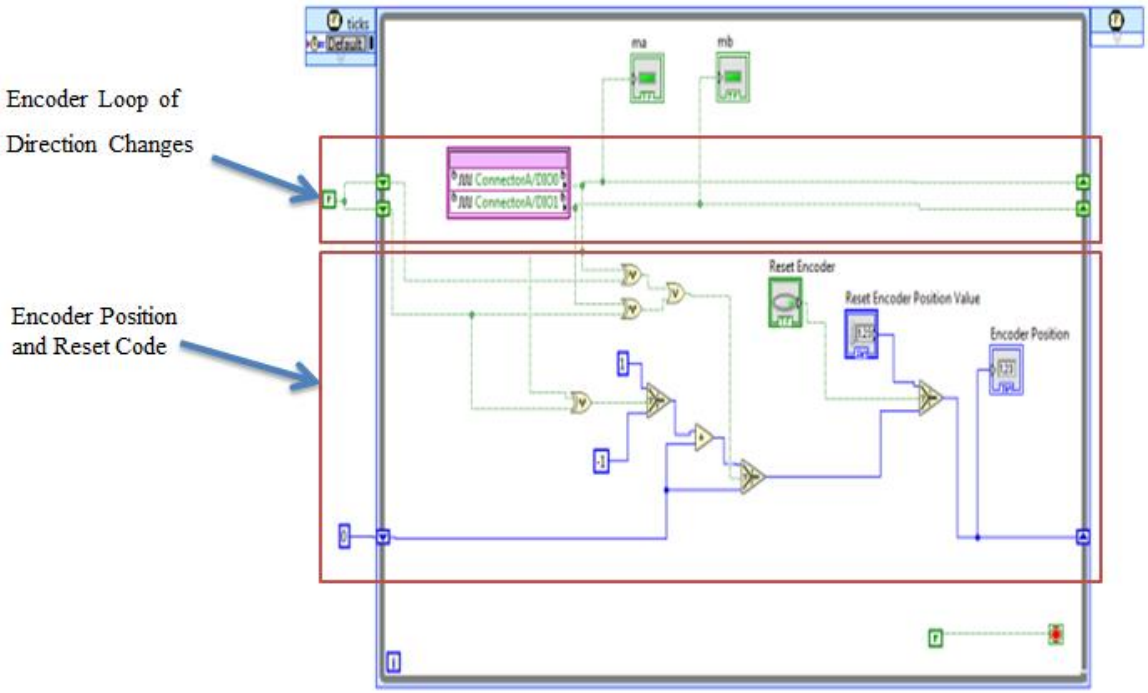


Figure 55. LabView code to read the encoder position

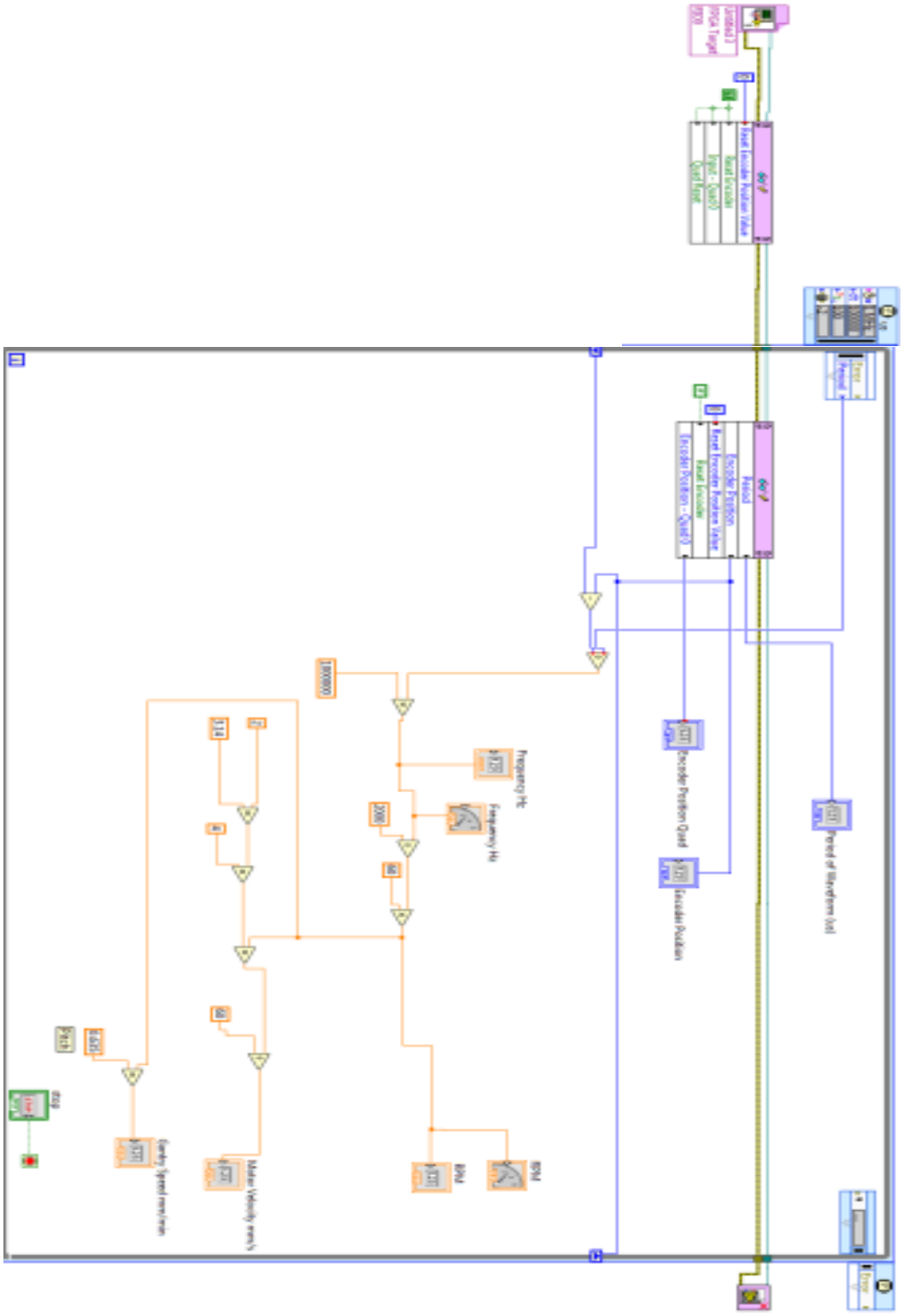

Figure 56. LabView code to calculate stepper motor speed

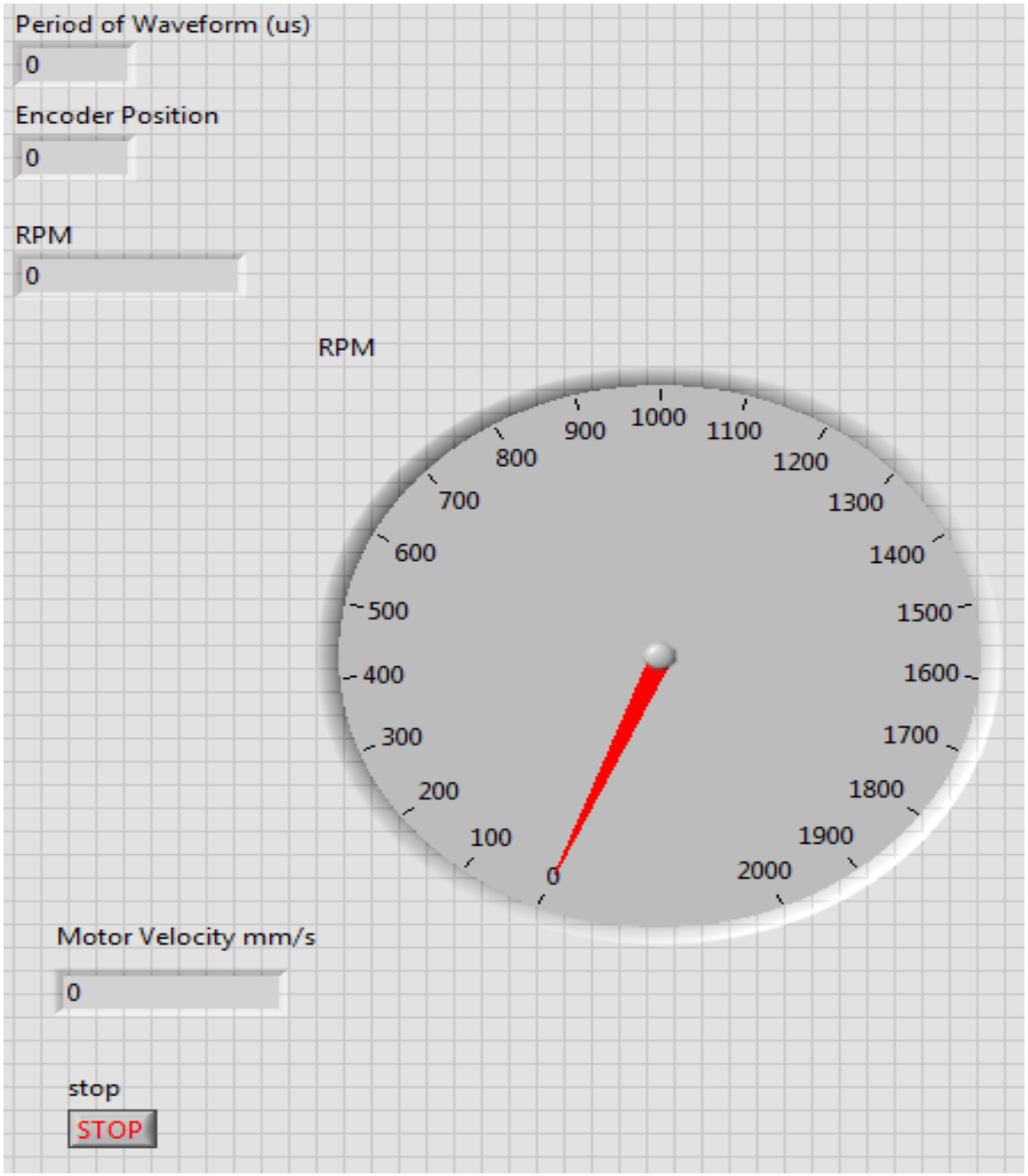


Figure 57. Front panel to measure stepper motor speed

# 5. OPTIMIZATION OF PROCESS PARAMETERS

An experiment is a process used to check how a system works and to ensure part quality before shipping. Conclusions are dependent on the experiment process, so experiment design and analysis techniques are significant to determine right solution. Data analysis of experiments should have at least two parameters that the researcher thinks are critical [71].

There are many methods of design of experiments used to analyze data, and each method will provide analysis of all parameters, intractions between parameters, and get a mathmetical model of parameters. This chapter will discuss response surface methodology (RSM) and genetic algorithm (GA) methods that are used to determine the mathmetical model and optimal solution by using five parameters and five levels. All samples will be manufactured using the prototype SLS system by applying different scenarios of the manufacturing process. Also, each scenario will be produced using different parameters. The target of analyzing the manufacturing process is to reduce surface roughness and crack width that happen during part production.

## 5.1 Factorial Experiments

A factorial experiment design has different parameter arrangement levels for each trial. Also, the experiment plan depends on the number of parameters, parameter levels, and methods used to arrange the trials. When building the experiments all the levels and parameters should consider getting better results. Figure 58 plot represents interaction of two variables A and B and two levels. The lines of this figure are parallel, which means

there is no interection. Figure 59 plot shows case of the interaction between the variables [71].

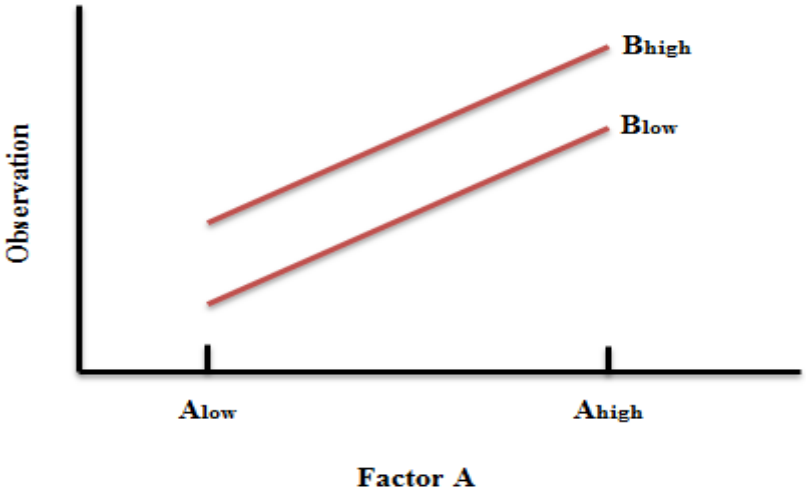


Figure 58. Factorial experiment, no interaction

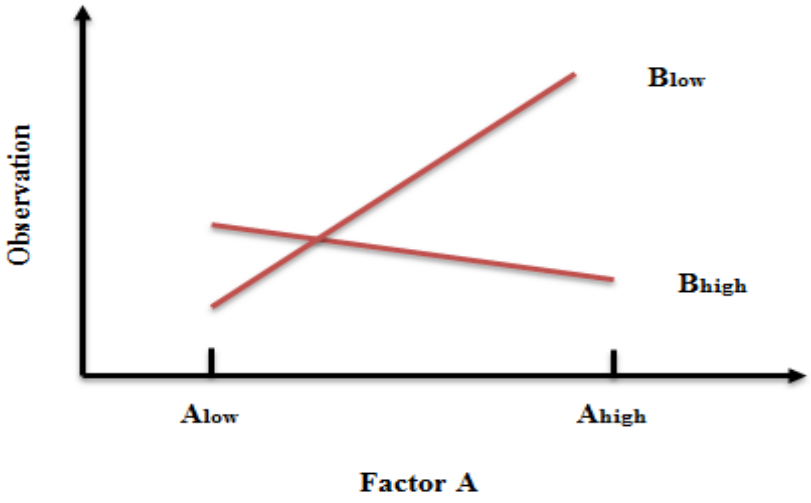


Figure 59. Factorial experiment, with interaction

## 5.2 $2^k$ Factorial Designs and Design of $k \geq 3$ Factors

Frequently, the factorial design is used to arrange the variables and their levels to study affecting variables on a final result. The most useful part of the matrix design of parameters is dependent on the variables number and level number [71]. The formula used to calculate number of experiments is $2^k$, when number 2 is used to represent number of levels and k is used to represent the number of levels. Two examples in this section show how to build the experiments matrix design. The building process depends on parameters number and levels number. The first example, shown in Figure 60, represents an experiments with two levels (high and low), and two parameters (A and B), so the total of experiments will be four. The plus sign indicates the high level, and the minus sign indicates the low level for each parameter.

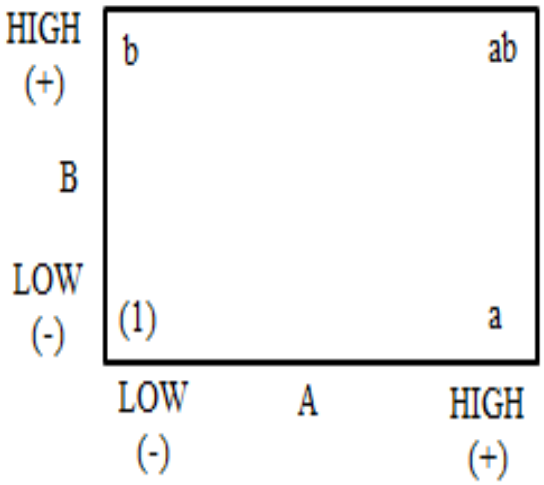


| Treatment | A | B |
|---|---|---|
| (1) | - | - |
| a | + | - |
| b | - | + |
| ab | + | + |

Figure 60. The $2^2$ factorial design [71]

The second example uses two levels and three parameters (A, B, and C). The formula will represented as $2^3$; so the total experiments will be eight. Figure 61 (a) displays the cubic geometry of the eight experiments and Figure 61 (b) shows the matrix design of $2^3$. RSM is used to build the matrix design of the experiments that will be used to build mathematical model.

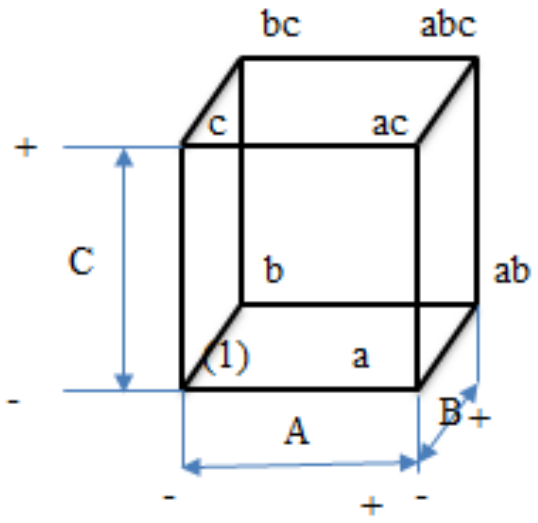


(a) Geometric View

| RUN | A | B | C |
|---|---|---|---|
| 1 | - | - | - |
| 2 | + | - | - |
| 3 | - | + | - |
| 4 | + | + | - |
| 5 | - | - | + |
| 6 | + | - | + |
| 7 | - | + | + |
| 8 | + | + | + |

(b) The $2^3$ Design Matrix

Figure 61. Example 23 design [71]

A main effect plot represents the change in a dependent parameter by changing the in independent parameter [71]. Figure 62 shows the main effects of the three variables, and interactions plots of two or three parameters. This figure also shows high and low levels of the parameters used to build the mathematical model. Main effect and interaction plots will be used in this research to check the relationship between parameters.

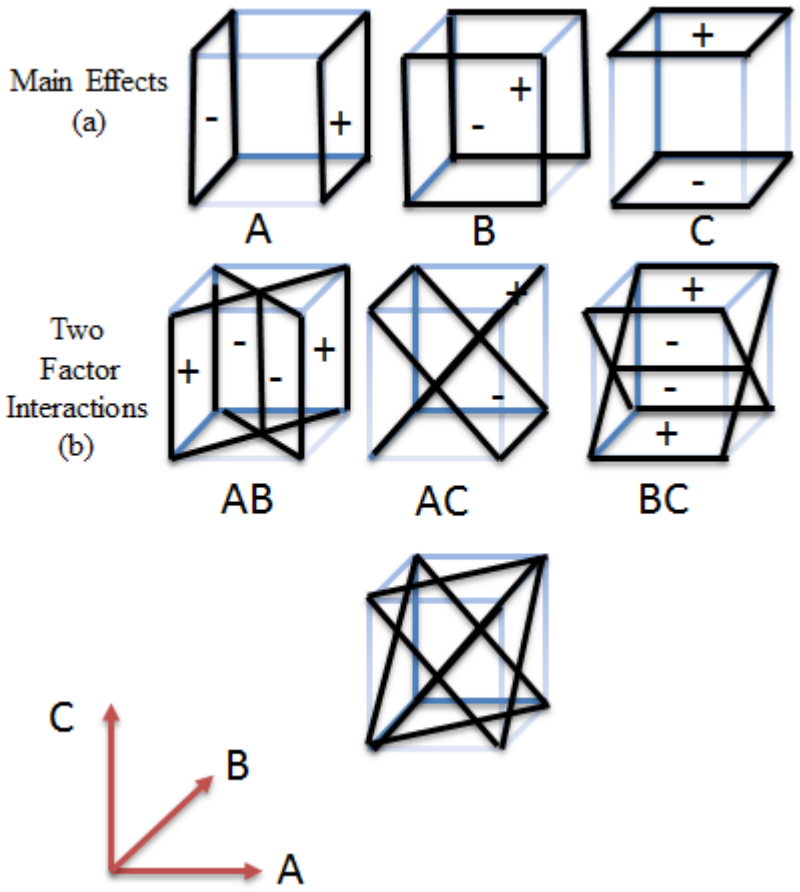


Figure 62. Contrasts of the main effects and interaction in the 23 design. (a) Main results. (b) Two-factor interactions. (c) Three-factor interaction [71]

## 5.3 Experimental Methods

RSM is a method combined with mathematical and statistical ways that are used to analyze experimental data and identify the optimum process parameters based on the response surface. The true relationship between the response surface and parameters is assumed to be unknown. Therefore, the first step is to determine an appropriate approximation of the response and process parameters. Next, an approximate region for the process parameters is determined by experimentation. Then a reduced set of experiments can be conducted within the approximate area to fit the approximate model to the response surface [71].

Figure 63 shows a representation of the central composite design used to get the RSM experiment matrix that will be used to determine the mathematical model of the SLS quality defects. The 32 base runs in this research depend on the numbers of variables and levels used to represent the mathematical model. Therefore, the specifications used to represent the total number of experiments are 16 cube corners, 10 axial points, and 6 cube center points [72].

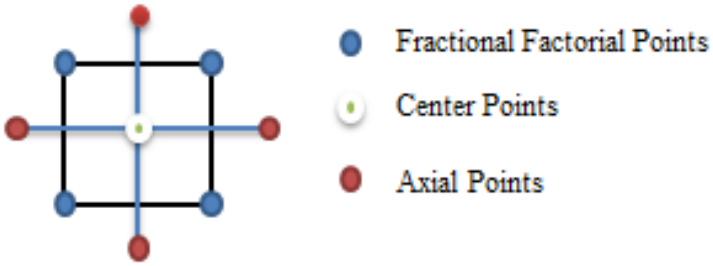


Figure 63. Central composite design

## 5.4 Application to Prototype SLS System

Determining manufacturing variables of the SLS system in this research, some initial trials should be done to understand how the system is working and which variables increase or decrease the defects part. Based on the initial trials, when increasing the side step or forward speed of the laser, a disconnect occurs during the fusing process that leads to increased porosity in the part. Figure 64 shows the flowchart used to determine the regression model to analyze defects that happen during production of parts by using the SLS prototype system.

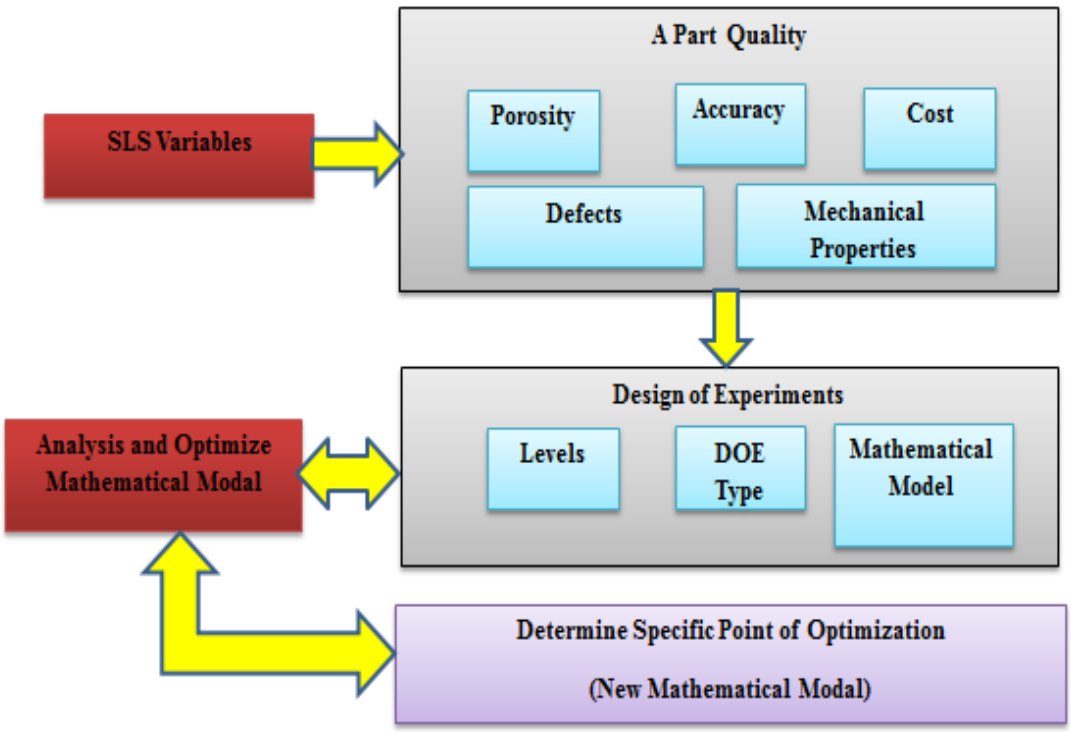


Figure 64. Regression model flowchart

The powder utilized in this study consists of 90% weight carbon steel powder and 2% carbon, 2% wax, 1% resin and 5% nylon powder (PA 650) by weight. Five process parameters (variables) and five levels are used in this research to build a mathematical model of part quality defects during the SLS process. Each of the variables is assigned a letter code for brevity. The variables are: side step A (mm), layer depth B (mm), speed C (mm/min), platform temperature D ($^{o}$C), and part length E (mm). Table 16 shows all variables and associated levels. The variables were selected based on the literature review and some initial experiments using the prototype SLS system.

Table 16. Manufacturing process levels

| **Symbol** | **Variables** | **Levels** | | | | |
|---|---|---|---|---|---|---|
| | | **-2** | **-1** | **0** | **1** | **2** |
| **A** | **Side Step (mm)** | 1 | 1.25 | 1.5 | 1.75 | 2 |
| **B** | **Layer depth (mm)** | 1 | 1.25 | 1.5 | 1.75 | 2 |
| **C** | **Speed (mm/s)** | 150 | 160 | 170 | 180 | 190 |
| **D** | **Platform Temp ($^{o}$C)** | 150 | 155 | 160 | 165 | 170 |
| **E** | **Part Length (mm)** | 45 | 50 | 55 | 60 | 65 |

Laser power, laser beam diameter, and material properties are critical variables that effect a part's quality. Therefore, laser power and laser beam diameter must be determined depending on the material properties and melting size. Figure 65 shows the top view and side view of manufacturing processes, and these views show the production paths and melting depth. Laser path given below will used to achieve experiments that will use also to build mathematical models of surface roughness and crack width.

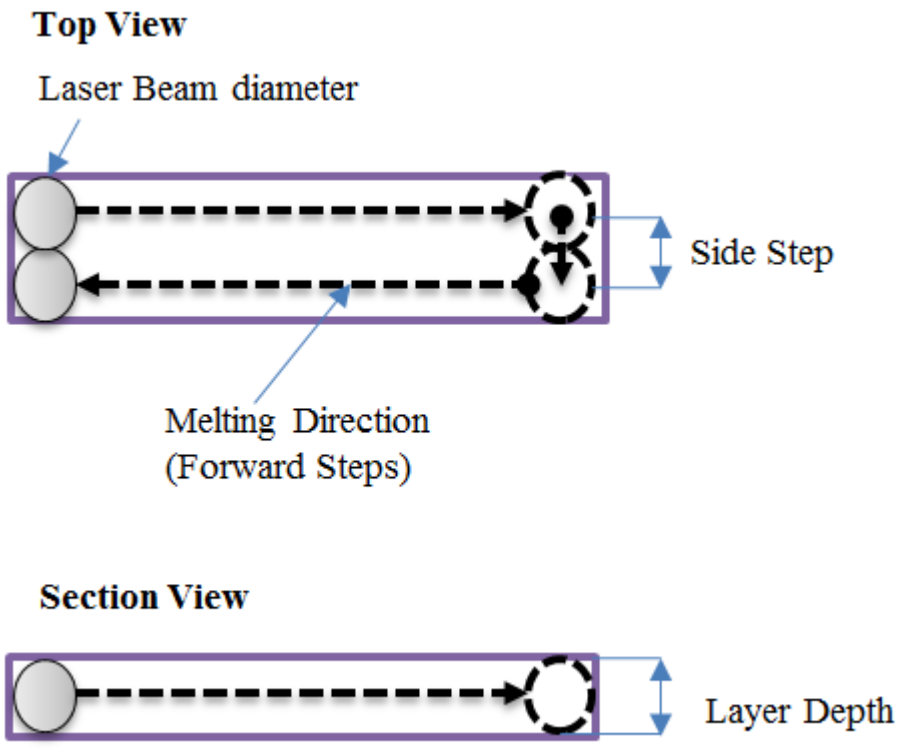


Figure 65. SLS manufacturing process views

### 5.4.1 Mathematical Models of Defects

The mathematical model of the defects is determined based on the variables defined previously. Equation 5.1 shows the standard regression model.

$$y = b_i x_i + \varepsilon \tag{5.1}$$

$$\hat{y} = y - \varepsilon = \sum b_i x_i \tag{5.2}$$

where i=1,2,3,4,5 refer to the variables, y is response $\hat{y}$ is the predicted value of the response, $b_i$ are experimentally determined coefficients, $x_i$ are the variable values, and $\varepsilon$ is the model error. Minitab 17 was selected to implement RSM based on ease of use and familiarity. Building the RSM experiment matrix after setting up some variables, creating the matrix design, determining variables and levels, and choosing the design table are analytical procedures used in this research to determine a mathematical model. The experiments are given in Table 17. All the arrangement process depended on the RSM method. Equation 5.3 is a second-order polynomial regression, and this equation was built depending on Equation 5.2 to represent the defects with manufacturing parameters.

$$\begin{aligned} y = {} & b_0 + b_1 A + b_2 B + b_3 C + b_4 D + b_5 E + b_{11} A^2 + b_{22} B^2 + b_{33} C^2 + \\ & b_{44} D^2 + b_{55} E^2 + b_{12} A \times B + b_{13} A \times C + b_{14} A \times D + b_{15} A \times E + \\ & b_{23} B \times C + b_{24} B \times D + b_{25} B \times E + b_{34} C \times D + b_{35} C \times E + b_{45} D \times E \end{aligned} \tag{5.3}$$

Table 17. Matrix of experimental conditions with resulting crack width and surface roughness values

| # | Levels | | | | | Crack Width mm | Surface Roughness mils |
|---|---|---|---|---|---|---|---|
| | A mm | B mm | C mm/s | D mm | E mm | | |
| 1 | -1 | -1 | -1 | -1 | 1 | 0.416 | 29 |
| 2 | 1 | -1 | -1 | -1 | -1 | 0.35 | 31.2 |
| 3 | -1 | 1 | -1 | -1 | -1 | 0.5 | 24.6 |
| 4 | 1 | 1 | -1 | -1 | 1 | 0.6 | 24 |
| 5 | -1 | -1 | 1 | -1 | -1 | 0.3 | 15.9 |
| 6 | 1 | -1 | 1 | -1 | 1 | 0.7 | 26.1 |
| 7 | -1 | 1 | 1 | -1 | 1 | 0.45 | 22.4 |
| 8 | 1 | 1 | 1 | -1 | -1 | 0.35 | 25.2 |
| 9 | -1 | -1 | -1 | 1 | -1 | 0.38 | 28.4 |
| 10 | 1 | -1 | -1 | 1 | 1 | 0.55 | 22.7 |
| 11 | -1 | 1 | -1 | 1 | 1 | 0.38 | 26.9 |
| 12 | 1 | 1 | -1 | 1 | -1 | 0.7 | 24.2 |
| 13 | -1 | -1 | 1 | 1 | 1 | 0.45 | 24.6 |
| 14 | 1 | -1 | 1 | 1 | -1 | 0.48 | 29.6 |
| 15 | -1 | 1 | 1 | 1 | -1 | 0.48 | 26.6 |
| 16 | 1 | 1 | 1 | 1 | 1 | 0.44 | 22.9 |
| 17 | -2 | 0 | 0 | 0 | 0 | 0.38 | 22 |
| 8 | 2 | 0 | 0 | 0 | 0 | 0.28 | 24.3 |
| 19 | 0 | -2 | 0 | 0 | 0 | 0.4 | 20.5 |
| 20 | 0 | 2 | 0 | 0 | 0 | 0.3 | 16.5 |
| 21 | 0 | 0 | -2 | 0 | 0 | 0.32 | 27 |
| 22 | 0 | 0 | 2 | 0 | 0 | 0.3 | 17 |
| 23 | 0 | 0 | 0 | -2 | 0 | 0.33 | 30 |
| 24 | 0 | 0 | 0 | 2 | 0 | 0.28 | 19.4 |
| 25 | 0 | 0 | 0 | 0 | -2 | 0.3 | 5.8 |
| 26 | 0 | 0 | 0 | 0 | 2 | 0.42 | 15.7 |
| 27 | 0 | 0 | 0 | 0 | 0 | 0.3 | 23.5 |
| 28 | 0 | 0 | 0 | 0 | 0 | 0.3 | 23.5 |
| 29 | 0 | 0 | 0 | 0 | 0 | 0.3 | 23.5 |
| 30 | 0 | 0 | 0 | 0 | 0 | 0.3 | 23.5 |
| 31 | 0 | 0 | 0 | 0 | 0 | 0.3 | 23.5 |
| 32 | 0 | 0 | 0 | 0 | 0 | 0.3 | 23.5 |

Figure 66 presents 32 samples of the experiments produced by using the SLS prototype system by using different parameters and levels to observe difference between samples. These samples were used to measure surface roughness and crack width for each sample, which will use to build mathematical models of surface roughness and crack width.

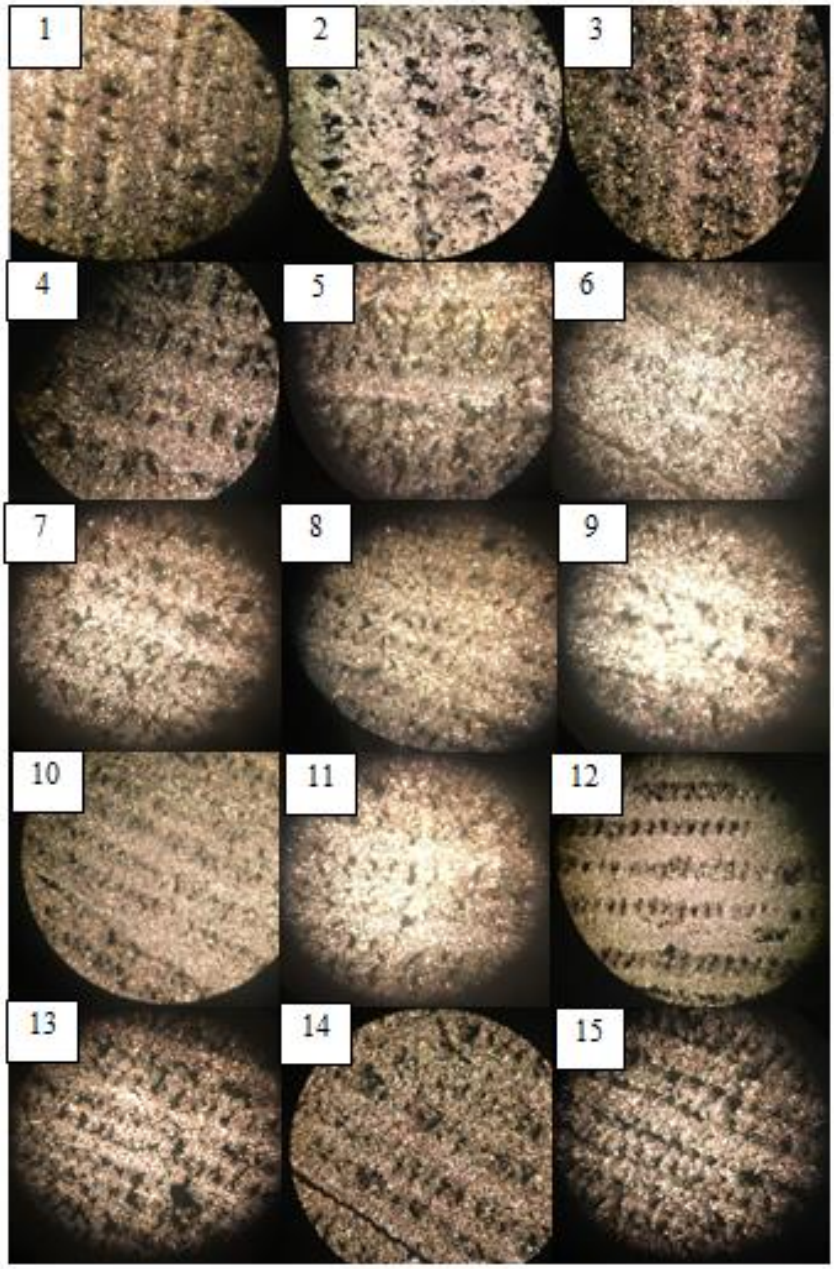

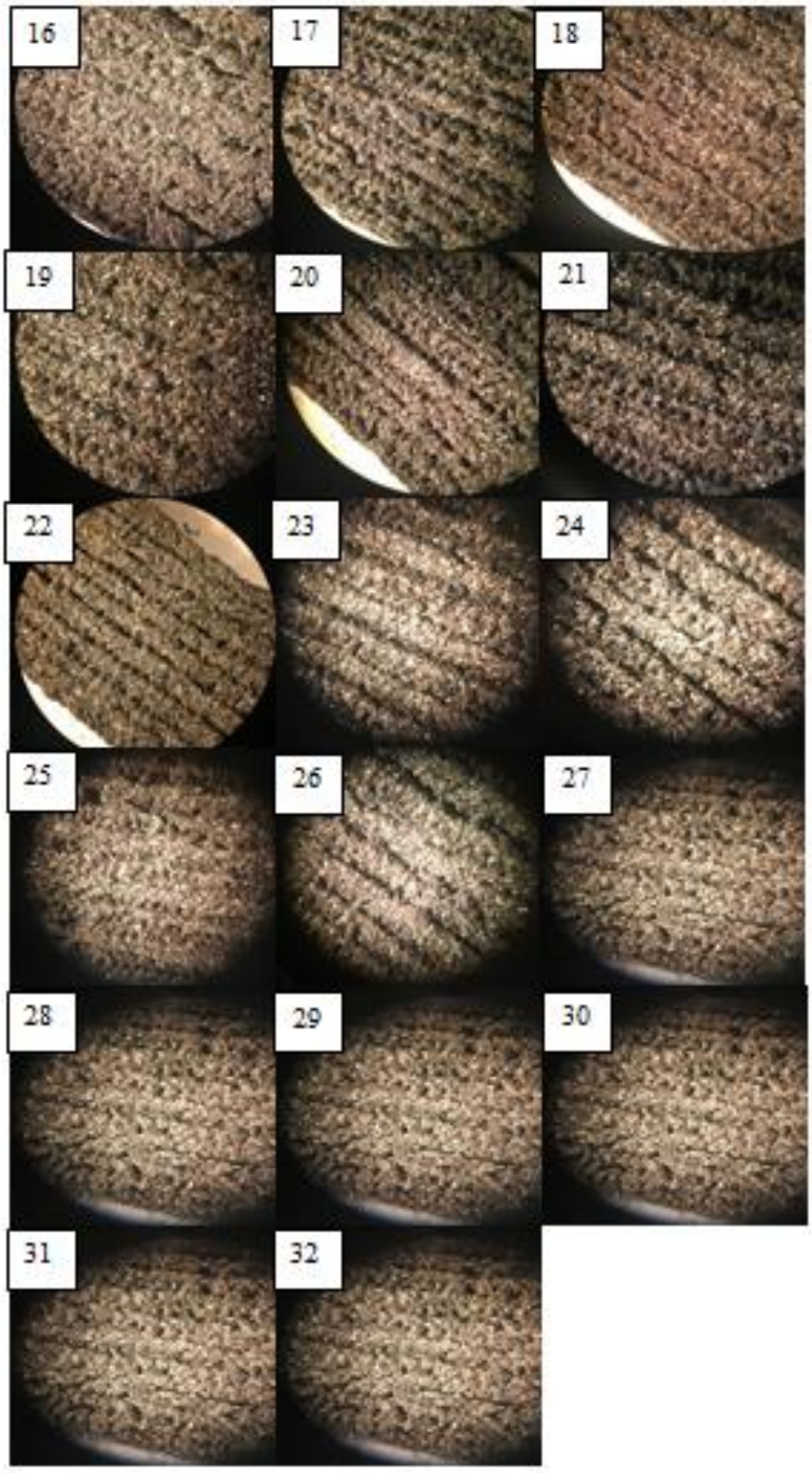


Figure 66. Microscope images of 32 experiments

Using Minitab and standard RSM methods, the crack width data from experiments shown in Table 17 was used to calculate the coefficients of Equation (5.3). The resulting model for crack width based on the selected variables is given in Equation (5.4) where $\hat{y}_1$ represents the crack width measured in mm.

$$\begin{aligned}\hat{y}_1 = {} & 0.2750 + 0.0218A - 0.0007B - 0.0074C + 0.0001D \\ & +0.0249E + 0.0325A^2 + 0.0375B^2 + 0.0275C^2 \\ & +0.0262D^2 + 0.0400E^2 - 0.0102A \times B \\ & -0.0202A \times C + 0.0148A \times D + 0.0290A \times E \\ & -0.0490B \times C + 0.0060B \times D - 0.0423B \times E \\ & -0.0115C \times D + 0.0202C \times E - 0.0498D \times E\end{aligned} \tag{5.4}$$

The main effect plot changes depend on the line status, so if the line is horizontal that means there is not main effect of the crack width and surface roughness. In this case, the results of crack width and surface roughness will be the same for all parameter levels. But if the line is not horizontal that leads to increased or decreased defect value. In this case, the results of crack width and surface roughness will be not the same for all parameter levels. Therefore, The greater defect happens when increasing in line height.

Figure 67 is for the main effect plot of parameters with various levels that have been produced by using data from Table 17. Greater main effect value happens when increasing the slope of the line.

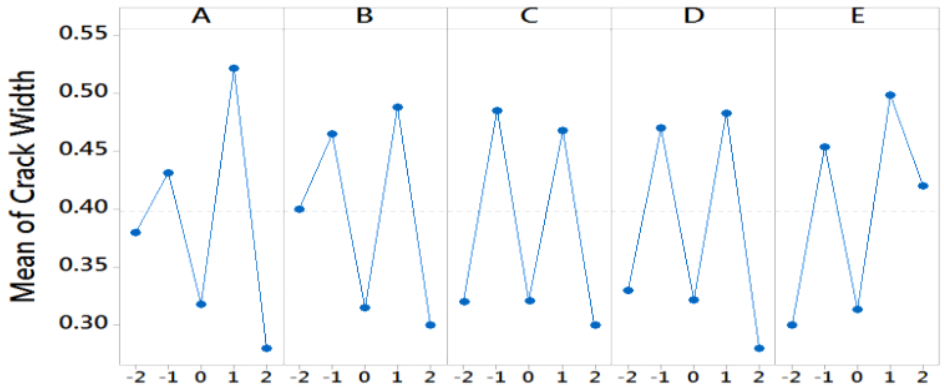


Figure 67. Main effect plot for crack width by using data from Table 17

Figure 68 shows the main effect plot of the crack width during the manufacturing process produced using Equation 5.4. The plot demonstrates the behavior of crack width by considering each parameter level. The minimum crack width happened near the mean values of the parameters (at Level 0). This is an indication that the first guess at optimal variables was reasonable.

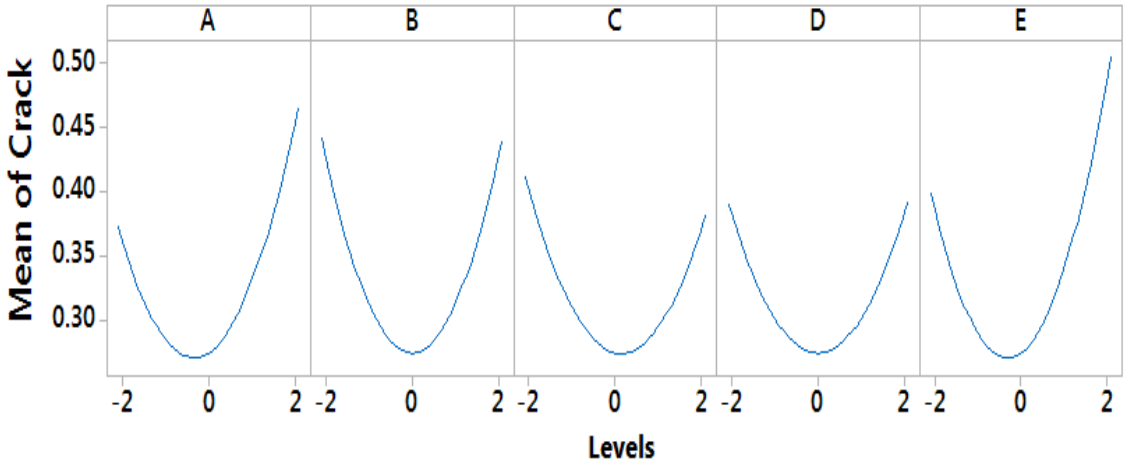


Figure 68. Main effect plot for crack width by using Equation 5.4

Interaction plots are used to display the mean defect effects versus parameters levels and to check whether or not results are significant by observing the interaction between parameters. Figure 69 shows the interaction between parameters of crack width. Analyzing the results, all parameters had interaction between each other. Therefore, all the combinations of parameters will be kept in the final results.

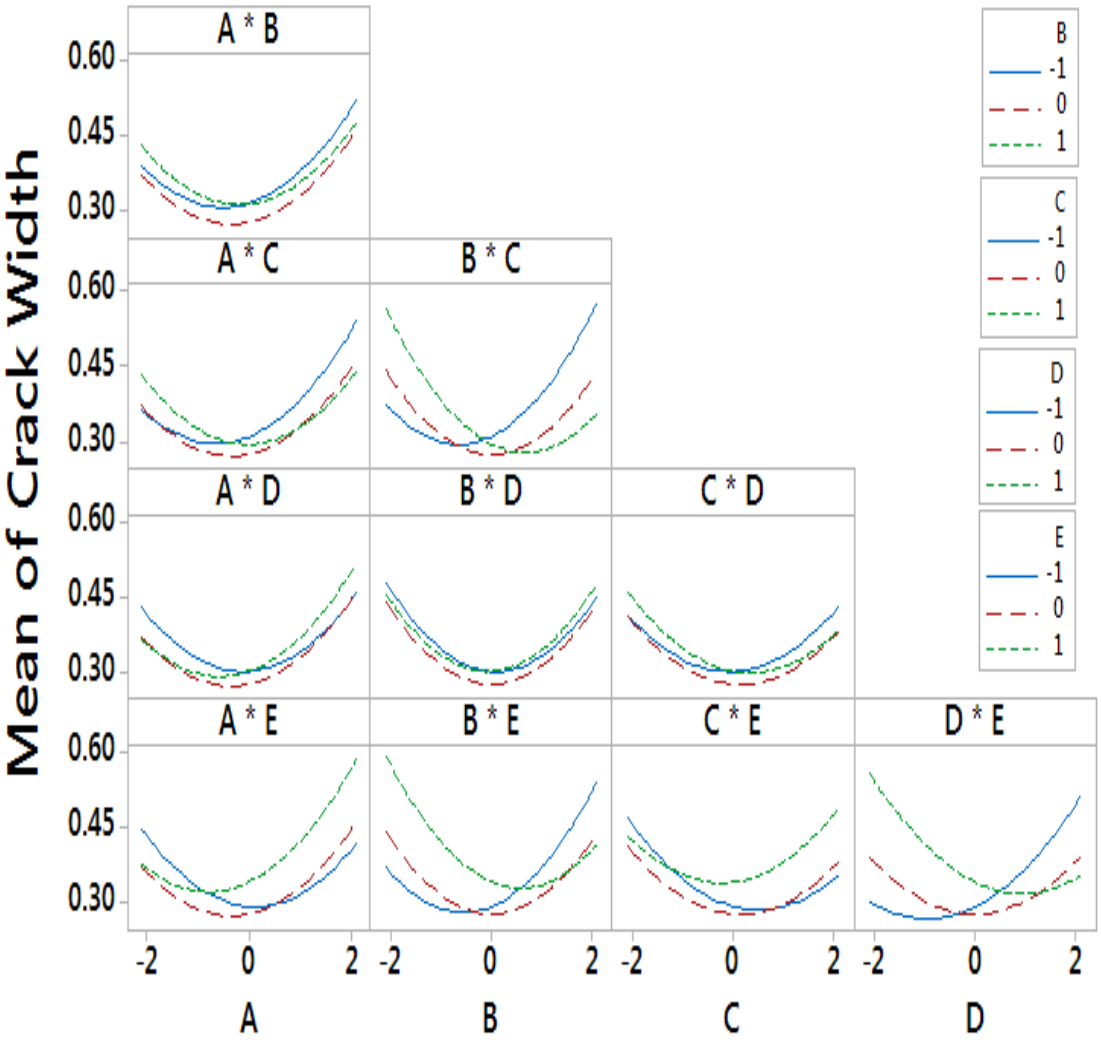


Figure 69. Interaction plot of crack width

Contour and surface plots are also used to analyze experiments The plots are drawn between each two parameters. Different colors of the contour plot and different shapes of the surface plot means changing the parameter values. Figure 70 shows the contour plot of all the combinations of parameters, and the results show that the variable level zero falls within the contour of minimum crack width. Unfortunately, this does not identify an exact optimal value for the variables.

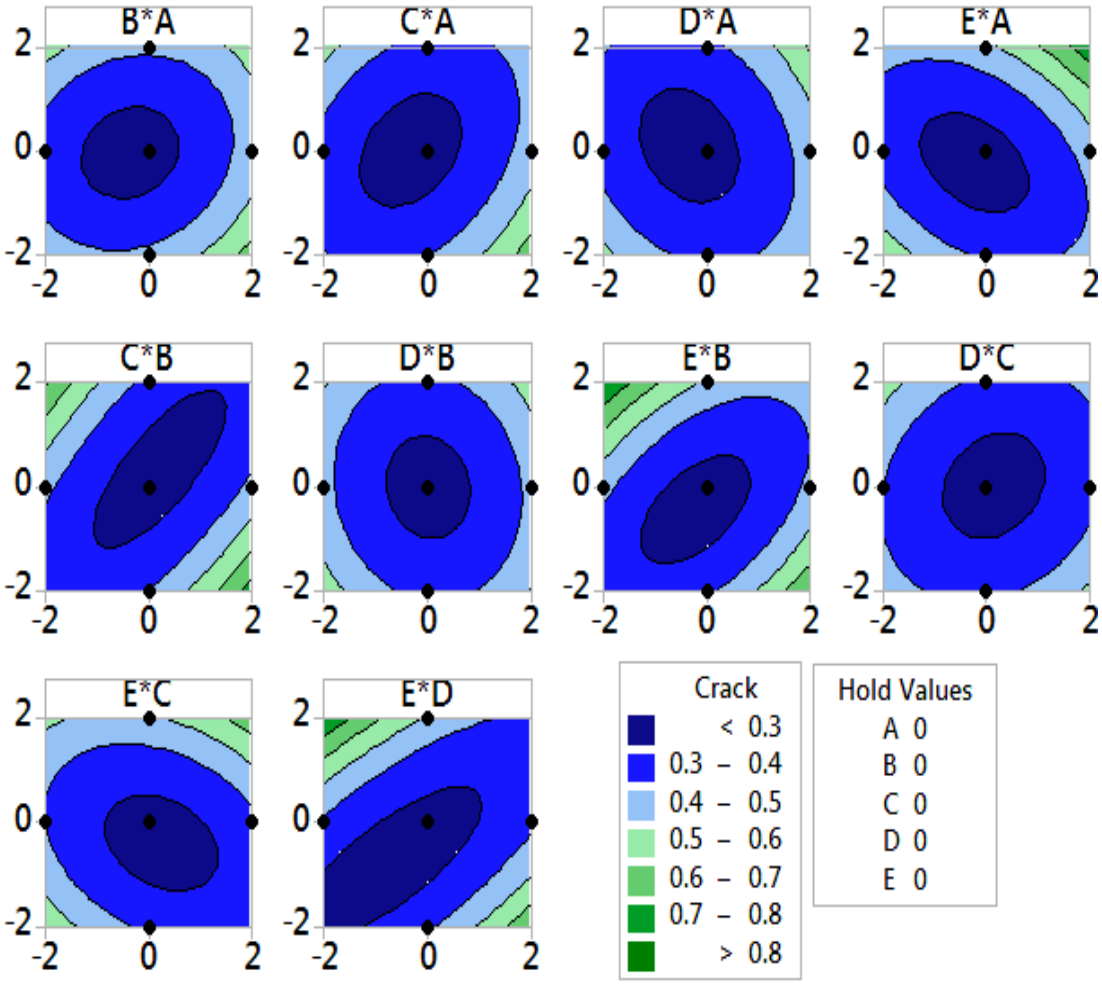


Figure 70. Contour plots of crack width

Figure 71, Figure 72, and Figure 73 show a series plots of response surface plots for significant interactions of all parameters. The results proved that crack width values decreased when all the parameters are at the medium level (level zero).

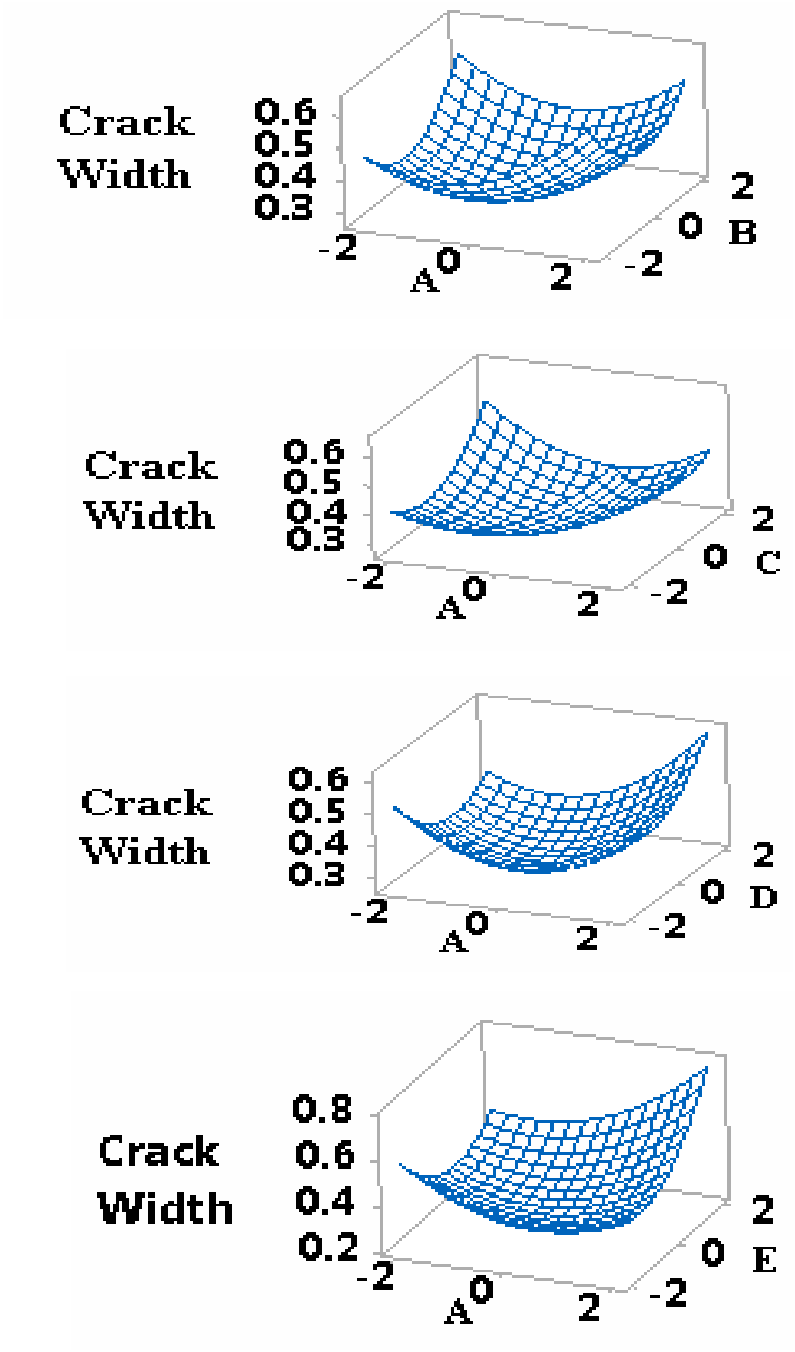


Figure 71. Surface plots of crack width for parameter A with other parameters

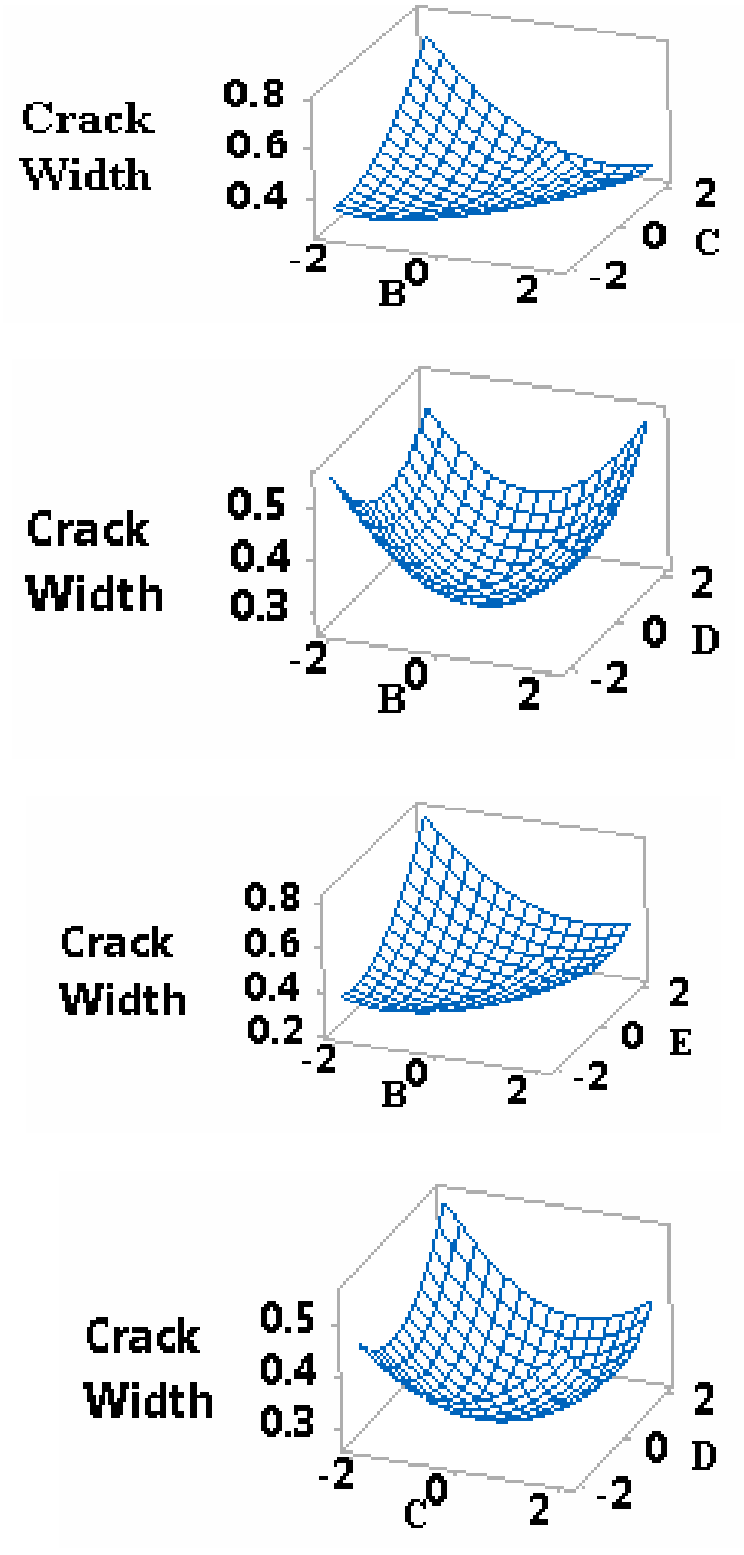


Figure 72. Surface plots of crack width for B parameter with other parameters and C parameter with D parameter

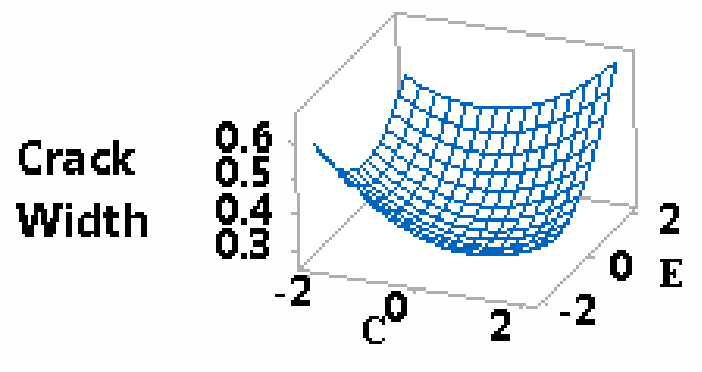


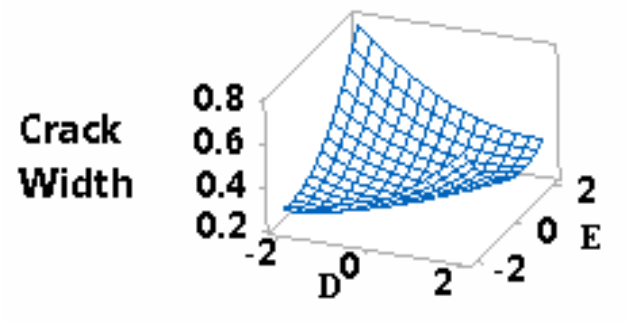


Figure 73. Surface plots of crack width for B parameter with other parameters and C parameter with D parameter

After crack width, the second defect considered was surface roughness. An SRT-622 surface profile gauge was used to measure roughness for Table 17. Equation (5.5) is the resulting second order model of surface roughness for the five variables tested where $\hat{y}_2$ represents the surface roughness.

$$\begin{aligned}\hat{y}_2 = {} & 22.34 + 0.50A - 0.78B - 1.57C - 0.57D + 0.53E \\ & +1.070A^2 - 0.092B^2 + 0.783C^2 + 1.458D^2 \\ & -2.030E^2 - 0.99A \times B + 1.32A \times C \\ & -1.36A \times D - 1.37A \times E + 0.78B \times C \\ & +0.08B \times D - 0.11B \times E + 1.29C \times D \\ & +0.28C \times E - 1.02D \times E\end{aligned} \tag{5.5}$$

As with crack width, RSM results were displayed regarding main effects, shown in Figure 74 and Figure 75; the interaction between parameters, shown in Figure 76; contour plots, shown in Figure 77; and surface plots, shown in Figure 78, Figure 79, and Figure 80. From the plots, all the parameters had interactions with each other; therefore, that all parameters will be used in the final result. The contour plot shows maximum and minimum surface roughness zone. The distribution area is a nonuniform region with settings levels. Surface roughness range changed from less than 15 to more than 40 mils. The target values of surface roughness are between 4-8 micrometers, see [25].

Ten response surface plots for significant interactions of all parameters were used to analyze the surface roughness data. The surface plot shows the relationship between parameters and surface roughness in 3D dimension. The results proved that surface roughness Ra values decreased when all the parameters were at the medium level (level zero).

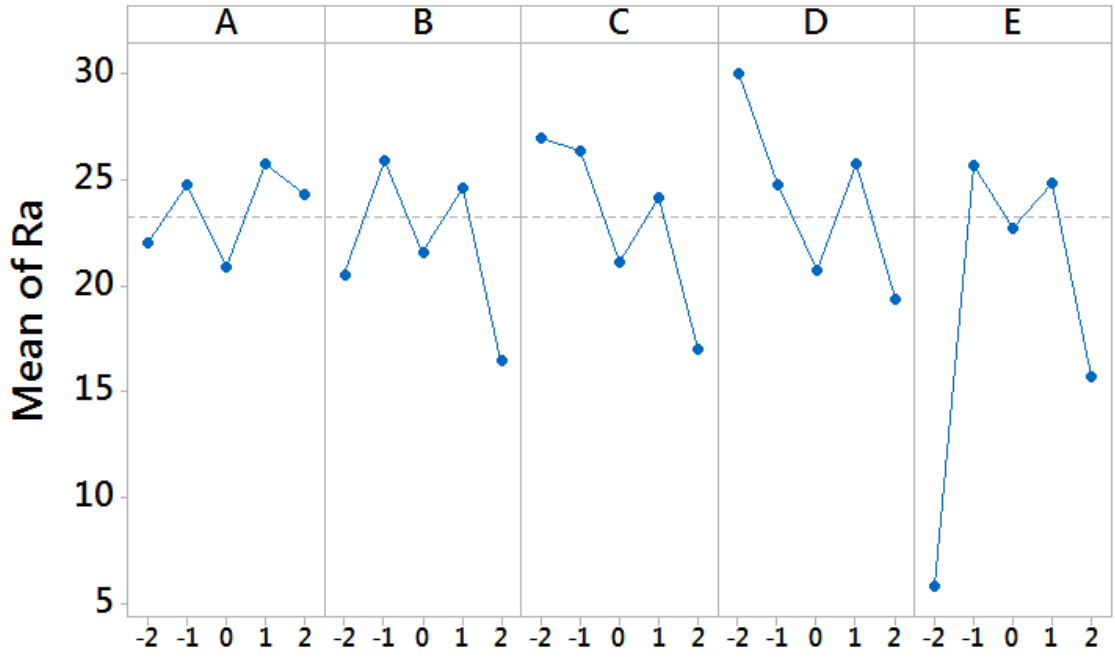


Figure 74. Main effect plot for surface roughness Ra by using data from Table 17

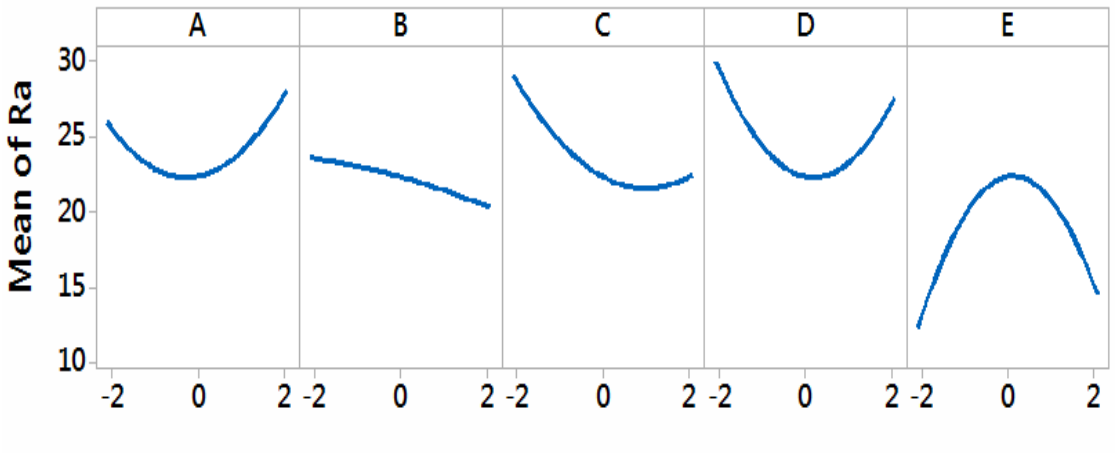


Figure 75. Main effect plot for surface roughness Ra by using Equation 5.5

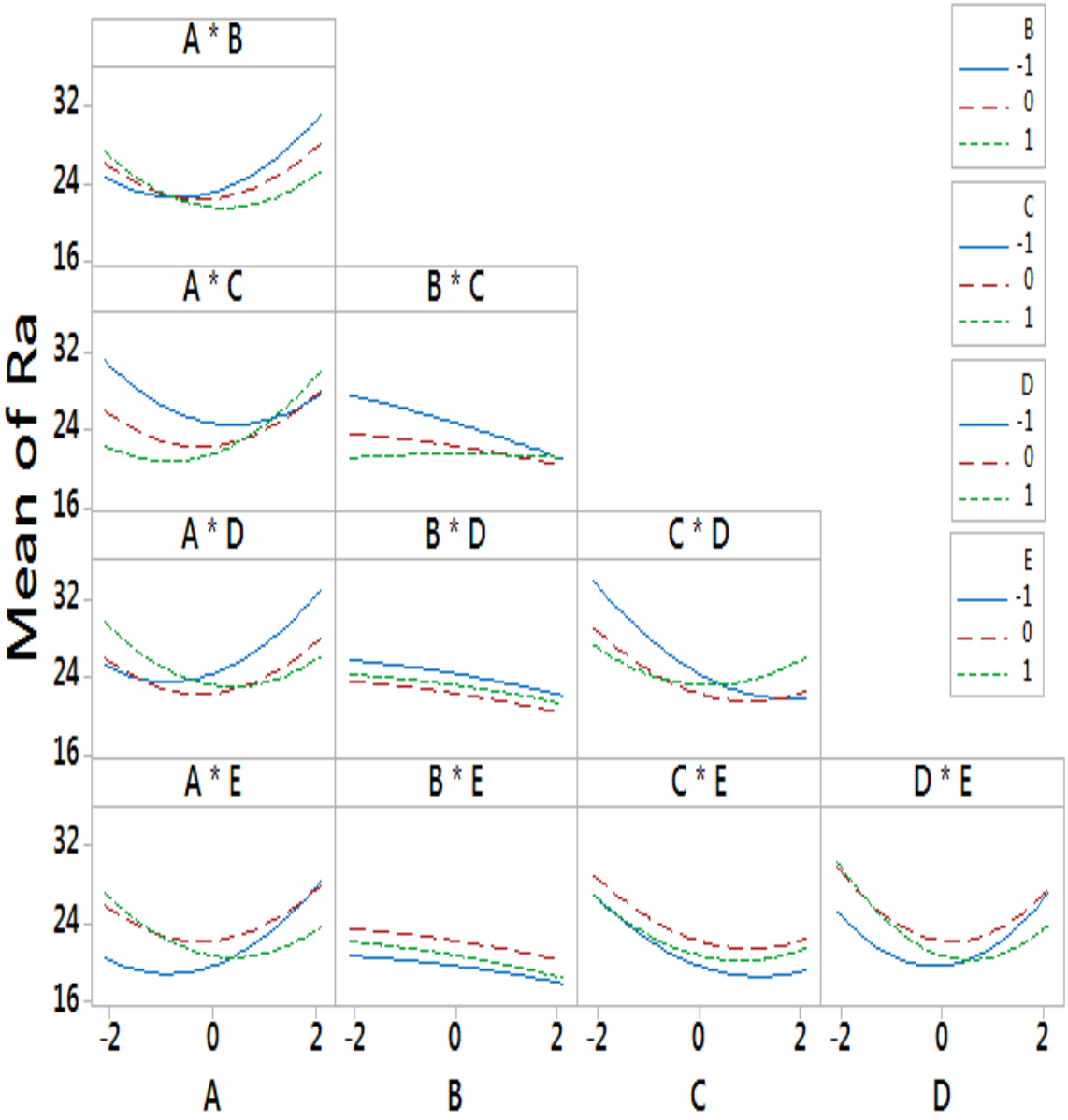


Figure 76. Interaction plot of surface roughness Ra

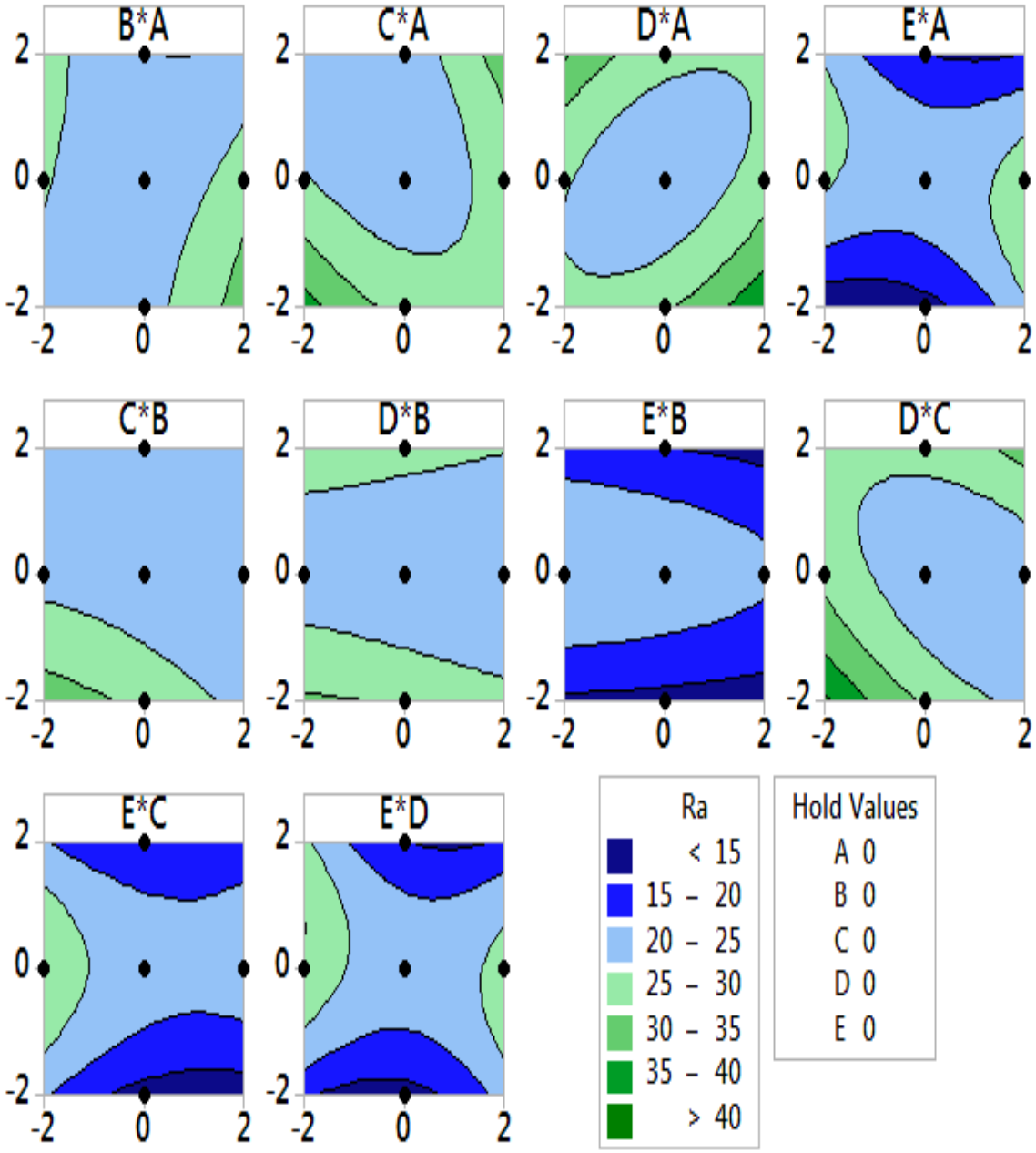


Figure 77. Contour plots of surface roughness Ra

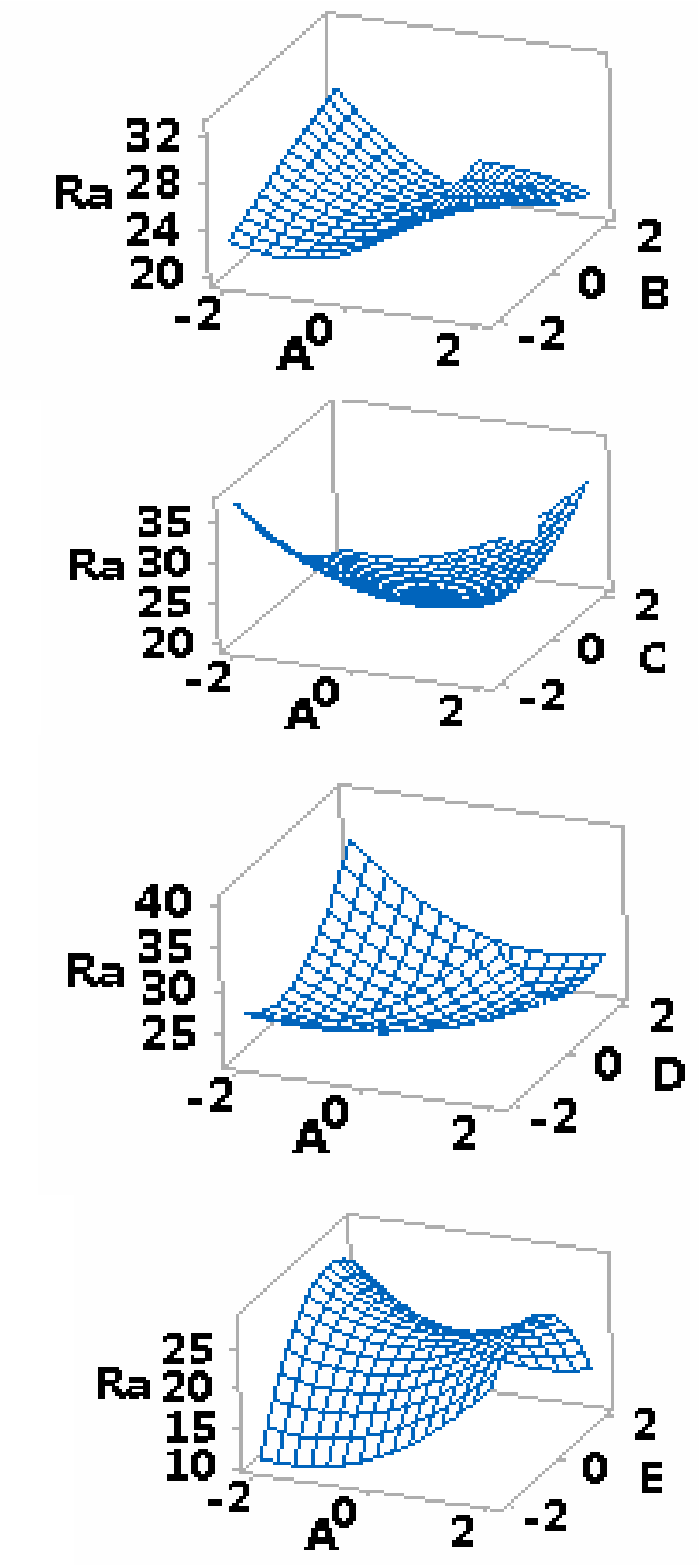


Figure 78. Surface plots of surface roughness Ra for parameter A with other parameters

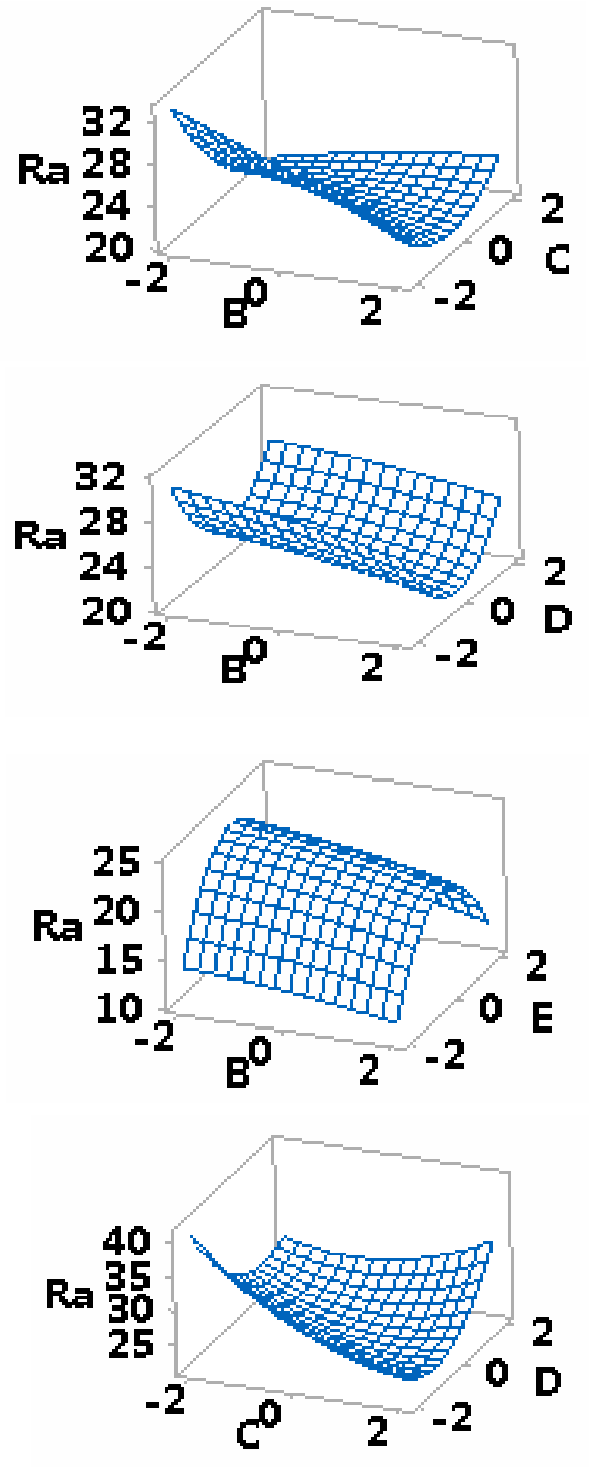


Figure 79. Surface plots of surface roughness Ra for B parameter with other parameters and C parameter with D parameter

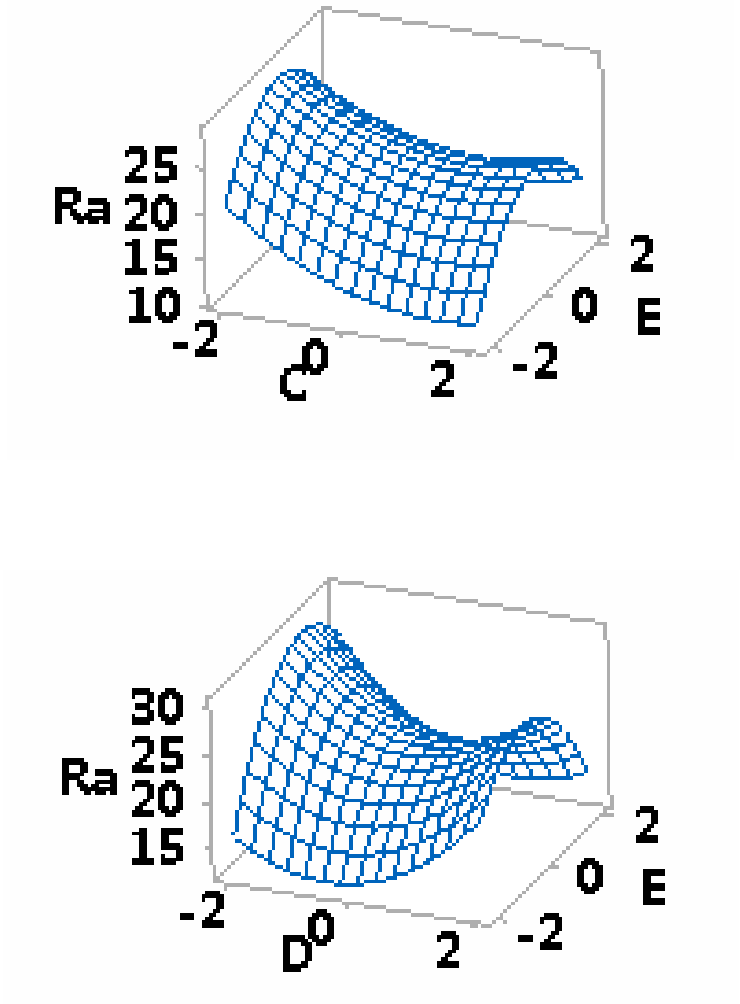


Figure 80. Surface plots of surface roughness Ra for B parameter with other parameters and C parameter with D parameter

### 5.4.2 Genetic Algorithm (GA)

A genetic algorithm (GA) is a method utilized to solve problems of constrained and unconstrained optimization. An optimal solution to the manufacturing process will be determined by depending on the GA procedures. Therefore, Figure 81 shows the flow chart of the GA steps to specify the optimal solution [41].

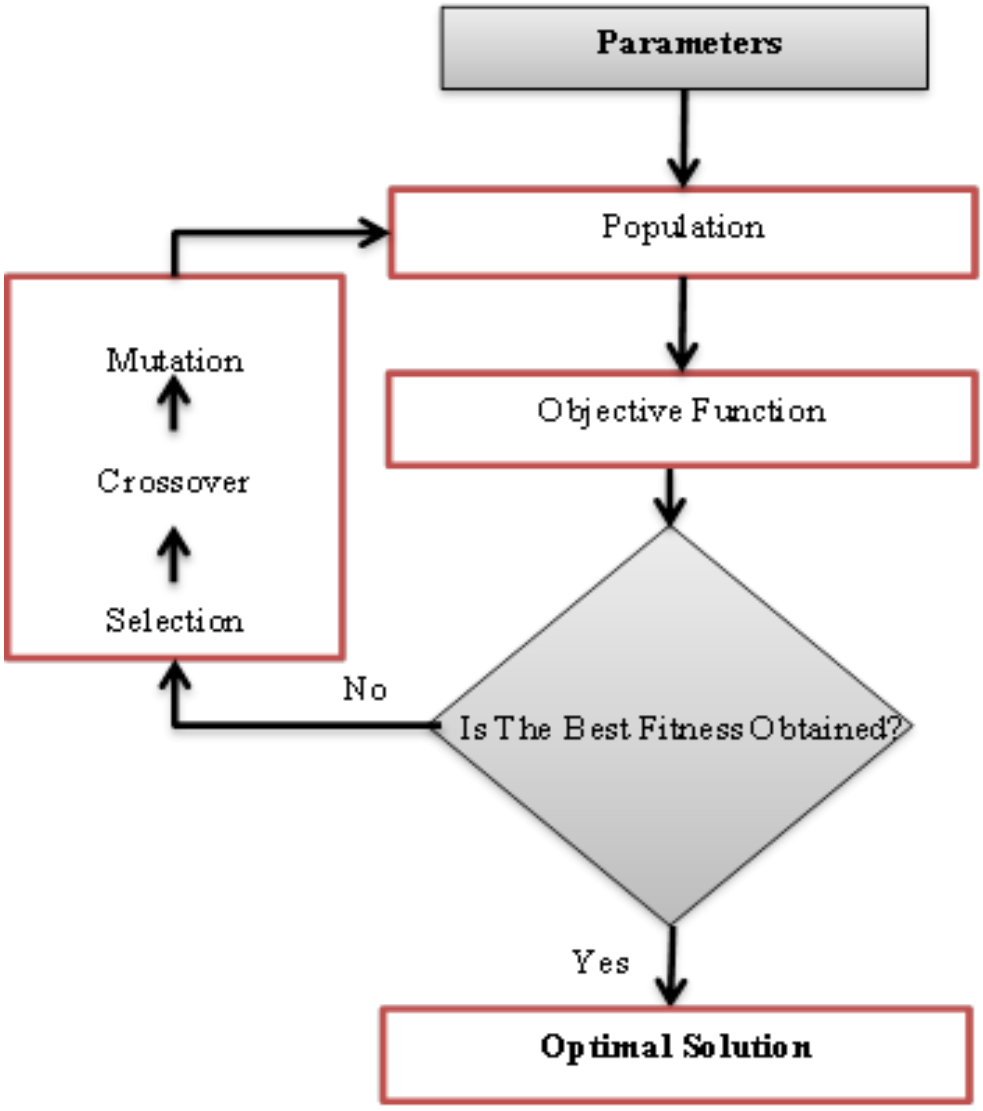


Figure 81. Flowchart for GA used in optimization [41]

The optimization process with GA starts by setting potential solution, called a chromosome. The arrangements of these chromosomes contain populaces which are arbitrarily chosen. The chromosomes develop to produce new generations. New generations known as offspring are produced by using the crossover and mutation methods. Crossover includes the way to split two chromosomes and after that combining one portion of every chromosome with the other. Mutation involves the way of flipping a chromosome. The GA alters a populace of individual arrangements over and over. At every progression, the GA chooses individuals at random from the present population to be parents and utilizes them to create the children for the next step. Over a progressive generation, the populace develops toward an ideal arrangement [41, 73].

The goal of the optimization method in this study is to choose the optimal values of the process parameters (A, B, C, D, and E) that lead to the lowest estimates of crack width and surface roughness. The previously developed models in Equations (5.4) and (5.5) have been taken to portray the change target. The crack width equation and the surface roughness equation are subjected as objective functions. The minimum and maximum process parameters values are shown below:

$$1 \leq A \leq 2$$

$$1 \leq B \leq 2$$

$$150 \leq C \leq 190$$

$$150 \leq D \leq 170$$

$$45 \leq E \leq 65$$

MATLAB R2013a was used to determine the optimal parameters by using the genetic algorithm tool. Before running the program, the GA parameters must be configured. In this work population size was set equal to 100, scaling function equal to "Rank," a selection function equal to "Roulette wheel," crossover function equivalent to "Heuristic," and crossover rate equal to 0.85.

Figure 82 shows the MATLAB window with settings and resulting optimal values of the parameters for crack width. The optimal process parameter values for minimum crack width are also provided in Table 18.

Table 18. Optimal variables to reduce crack width

| Symbol | Parameters | Values |
|---|---|---|
| A | Side Step (mm) | 1 |
| B | Layer Depth (mm) | 1.966 |
| C | Speed (mm/s) | 150 |
| D | Platform Temp ($C^o$) | 150 |
| E | Part Length (mm) | 55.955 |

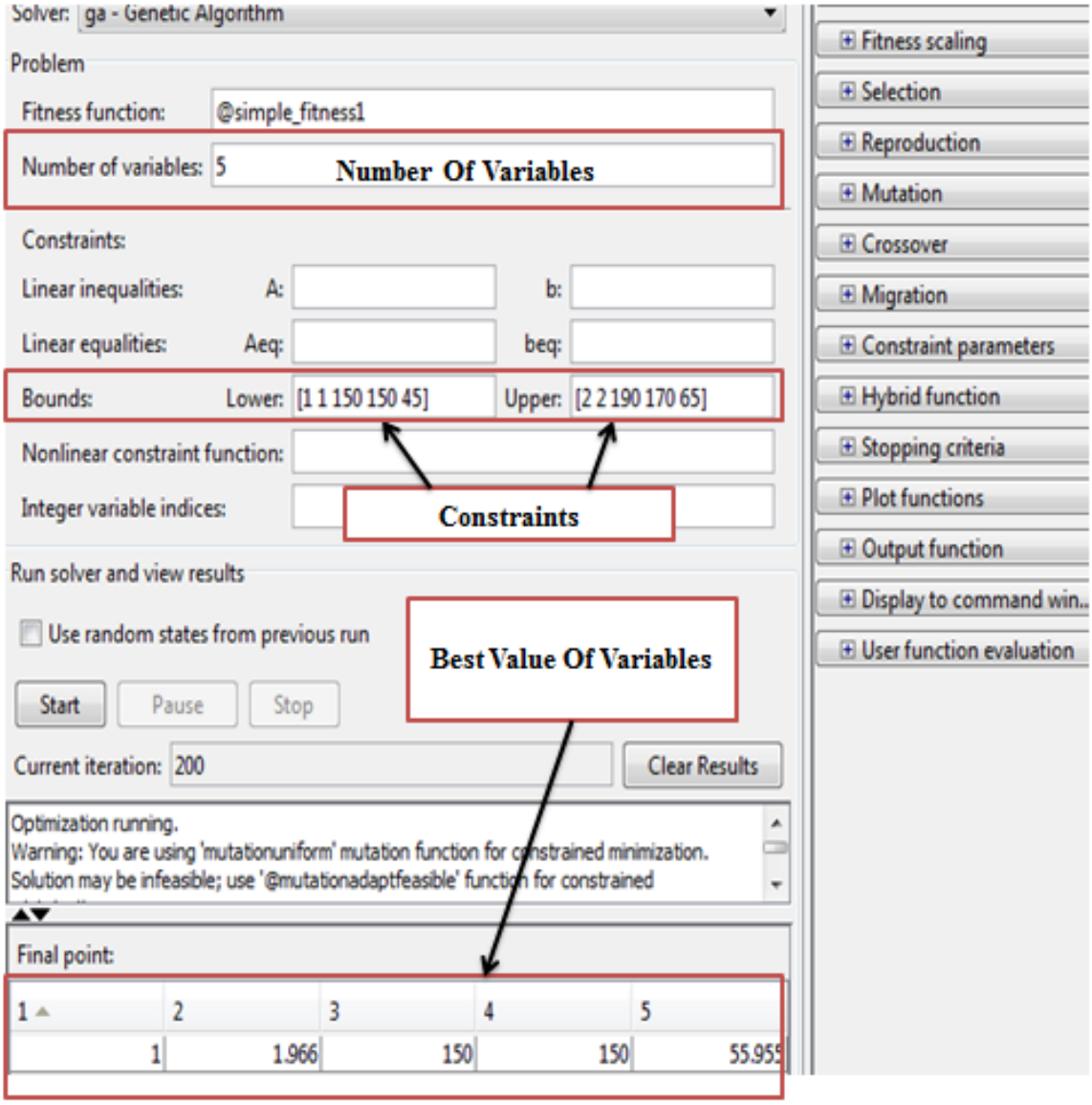


Figure 82. Optimal variables of manufacturing operation of crack width

Figure 83 is to determine the best fitness magnitude by using GA, so after running the program, the best fitness was 810.35, which means the optimal solution happened at this point between 155-165 generations.

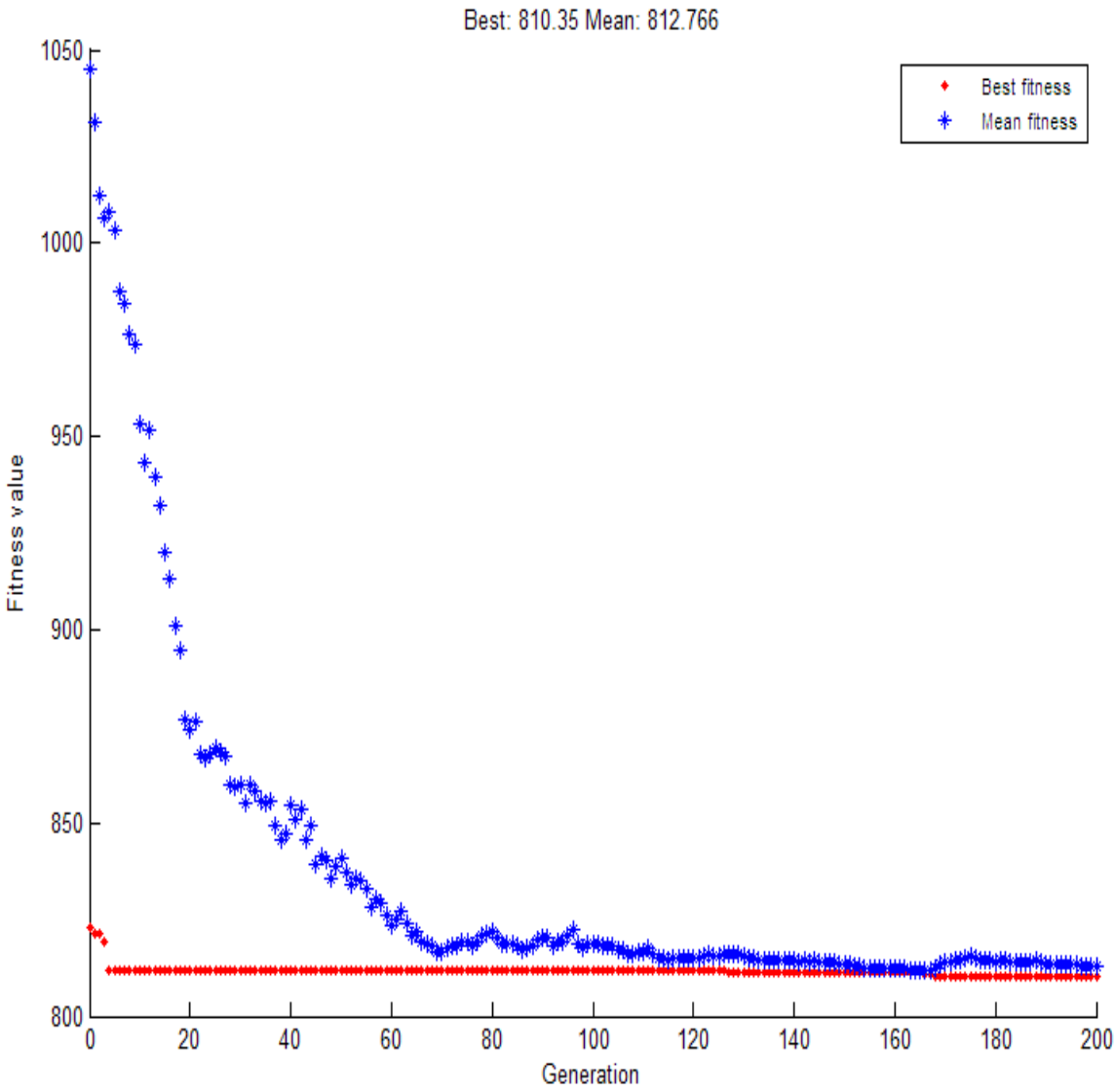


Figure 83. Genetic algorithm fitness plot of the crack width

The GA procedure was repeated for surface roughness with the same minimum and maximum process parameter values and the same GA configuration. The resulting optimal process parameter values for minimum surface roughness are shown in Table 19. Figure 84 shows the fitness magnitude by using GA, so after running the program got 63636.2, which means the optimal solution happened at this point between 130-200 generations.

Table 19. Optimal variables to reduce surface roughness Ra

| Symbol | Parameters | Values |
|---|---|---|
| A | Side Step (mm) | 1.995 |
| B | Layer Depth (mm) | 1.163 |
| C | Speed (mm/s) | 150 |
| D | Platform Temp. ($C^o$) | 150 |
| E | Part Length (mm) | 64.909 |

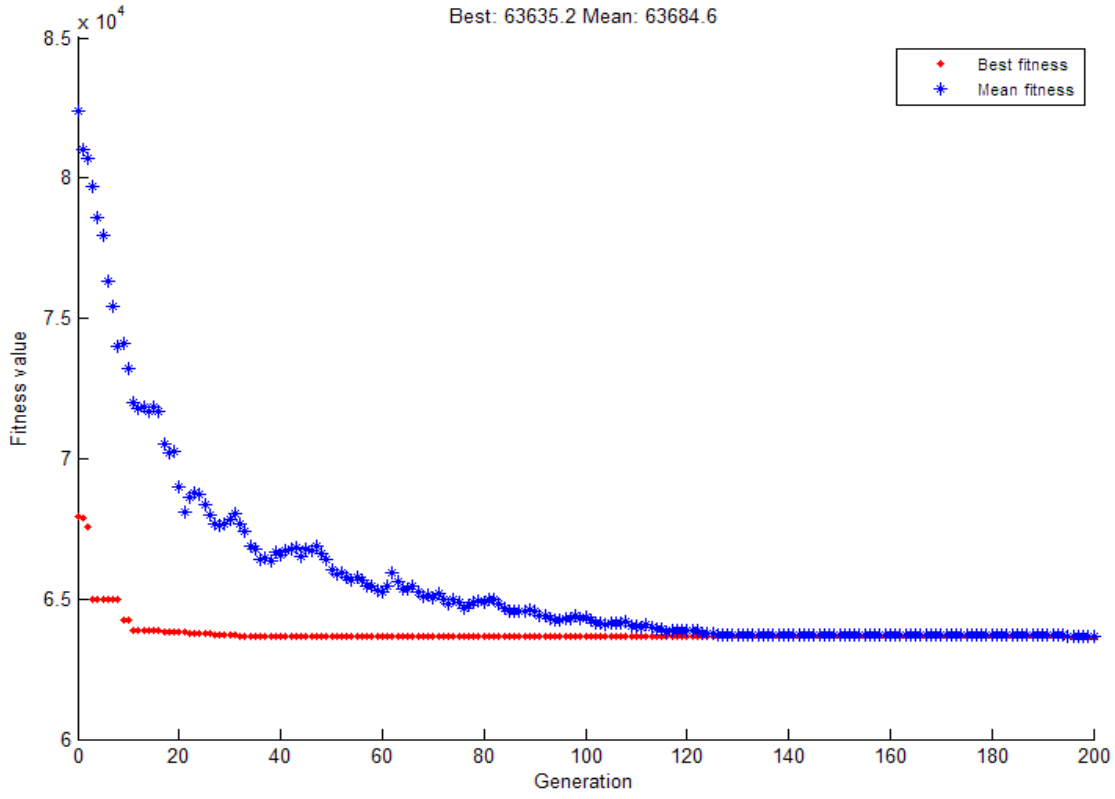


Figure 84. Genetic algorithm fitness plot of the surface roughness

### 5.4.3 Mathematical Model Validation

Equation 5.6 [72] was used to estimate the least squares estimator of β, where y is response crack width/surface roughness and $X = x_{ij}$ is level variable. The reason for determining β is to double check the mathematical models of crack width and surface roughness that were calculated previously by using MINITAB 17. The checking process used MATLAB R2013a to test the mathematical models.

Figure 85 and Figure 86 are results of crack width mathematical model and surface roughness mathematical model. Mathematical models from MATLAB models are the same mathematical model obtained from MINITAB, which means these mathmetical are right and ready to use to get optimal solution.

$$\beta = (X' \times X)^{-1} \times X' \times y \tag{5.6}$$

where

$$y=\begin{bmatrix} y_1 \\ y_2 \\ \vdots \end{bmatrix}, \qquad X = \begin{bmatrix} 1 & x_{11} & \dots \\ 1 & x_{21} & \dots \\ \vdots & \vdots & \vdots \end{bmatrix}, \qquad \beta = \begin{bmatrix} \beta_0 \\ \beta_1 \\ \vdots \end{bmatrix}$$

B =

0.2750
0.0218
-0.0007
-0.0074
0.0001
0.0249
0.0325
0.0375
0.0275
0.0262
0.0400
-0.0102
-0.0202
0.0148
0.0290
-0.0490
0.0060
-0.0423
-0.0115
0.0202
-0.0498

$$\hat{y}_1 = 0.2750 + 0.0218A - 0.0007B - 0.0074C + 0.0001D + 0.0249E + 0.0325A^2 + 0.0375B^2 + 0.0275C^2 + 0.0262D^2 + 0.0400E^2 - 0.0102A \times B - 0.0202A \times C + 0.0148A \times D + 0.0290A \times E - 0.0490B \times C + 0.0060B \times D - 0.0423B \times E - 0.0115C \times D + 0.0202C \times E - 0.0498D \times E$$

Figure 85. MATLAB crack width results of the least squares estimator of β

B =

22.3420
0.5042
-0.7792
-1.5708
-0.5708
0.5292
1.0705
-0.0920
0.7830
1.4580
-2.0295
-0.9937
1.3187
-1.3563
-1.3688
0.7813
0.0812
-0.1063
1.2938
0.2812
-1.0188

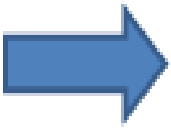

$$\hat{y}_2 = 22.34 + 0.50A - 0.78B - 1.57C - 0.57D + 0.53E$$
$$+1.070A^2 - 0.092B^2 + 0.783C^2 + 1.458D^2$$
$$-2.030E^2 - 0.99A \times B + 1.32A \times C$$
$$-1.36A \times D - 1.37A \times E + 0.78B \times C$$
$$+0.08B \times D - 0.11B \times E + 1.29C \times D$$
$$+0.28C \times E - 1.02D \times E$$

Figure 86. MATLAB surface roughness results of the least squares estimator of β

# 6. CONCLUSIONS

This work presented the design, build, validation, and use of a laboratory scale prototype SLS system for optimization of SLS process parameters. The prototype SLS system was working on four axes with resolution equal to 0.003. Some equipment with some printed parts by using 3D printer were used to build the prototype SLS system. The laser positioning system used a thread bar pitch and motor step angle to determine the minimum step. The total power used to melt 0.42 mm with 9.7 W depended on the powder properties used in the workpiece. The powder consists of carbon steel powder, carbon, wax, resin, and nylon powder (PA 650). Therefore, nylon powder was used as a binder between carbon steel grains. Carbon was used to increase laser absorption during the melting process. Wax was used to reduce the porosity of parts, and the resin was used to minimize shrinkage of parts. The ON/OFF laser was system controlled by using a manufacturing program. Therefore, after assembling the laser with the microprocessor, the manufacturing program has code responsibility for control of the laser and that code is sent to the microprocessor to give signal ON/OFF to the laser. Two guides with a stepper motor was a simple design and easy fix to distribute powder on the powder table. There were three builds of the frames, two of them were wood, and the third one was steel, but the steel frame was used to create the prototype SLS system.

Forward step and sidestep errors of the laser positioning system were checked in X-axis and Y-axis. Maximum tool path error due to vibration when speed was equal to 170 mm/s in X direction was 0.736 μm and Y direction was 0.012 μm when speed was equal to 190 mm/s.

These errors were minimal, less than one step. However, the maximum error due to runout is equal to 0.381 mm in the X direction and 0.762 mm in Y direction, and these errors came from the low-cost components. These errors are considered large relative to the resolution of the system.

The validation process of the laser proved that the laser was 9.7 W ellipse shape with 0.42 mm in the major axis and 0.038 mm in the minor axis. When checking the laser beam shape after removing the lens of the laser system, using SPIRICON model SP620U sensor, the laser beam shape was very close to a triangle. The stepper motor speed was checked by using five different speeds, and there was no deviation between manufacturing program speed and actual stepper motor speed.

This work also optimized five process parameters to minimize crack width and surface roughness. Based on RSM, only 32 experiments were used to build mathematical models of the crack width and surface roughness as functions of the selected process parameters. To improve on these results, the GA method of constrained optimization was applied to determine an optimal set of process parameters for each of the defects. The results proved some variables had interaction between each other and some did not. Also, the contour plot shows the maximum and minimum crack width and surface roughness.

# REFERENCES


[1] D. Gu, *Laser Additive Manufacturing of High-Performance Materials,* Springer, 2015.

[2] I. Gibson, D. W. Rosen and B. Stucker, *Additive Manufacturing Technologies Rapid Prototyping to Direct Digital Manufacturing,* Springer Science and Business Media, 2010.

[3] A. A. Zadpoor, "Design for Additive Bio-Manufacturing: From Patient-Specific Medical Devices to Rationally Designed Meta-Biomaterials," *International Journal of Molecular Sciences,* vol. 18, no. 8, pp. 1-18, 2017.

[4] B. Artley and B. Redwood, "3D Printing in the Automotive Industry," *PrintForm,* 2017.

[5] M. P. Groover, *Fundamentals of Modern-Manufacturing,* John Wiley & Sons, USA, 2010.

[6] P. Ciraud, "Verfahren und vorrichtung zur herstellung beliebiger gegenstande aus beliebigem schmelzbarem material". German Patent DE 2263777, 1973.

[7] R. Housholder, "Molding process". US Patent 4247508, 1981.

[8] T. Wohlers and T. Gornet, "History of additive manufacturing," Wohlers Associates, USA, 2014.

[9] J. P. Kruth, M. Leu and T. Nakagawa, "Progress in Additive Manufacturing and Rapid Prototyping," *CIRP Annals ,* vol. 47, no. 2, pp. 525-540, 1998.

[10] M. Salmi, "Medical applications of additive manufacturing in surgery and dental care," *Ph.D. Dissertation, Aalto University, Department of Engineering Design and Production,* 2013.

[11] S. P. Isanaka and F. Liou, "The Applications of Additive Manufacturing Technologies in Cyber-Enabled Manufacturing Systems," in *23rd Annual International Solid Freeform Fabrication Symposium an Additive Manufacturing Conference*, USA, 2012.

[12] G. Jin, W. D. Li, C. Tsai and L. Wang, "Adaptive tool-path generation of rapid prototyping for complex product models," *Journal of Manufacturing Systems,* vol. 30, no. 3, pp. 154-164, 2011.

[13] H. I. Medellín-Castillo and J. E. Pedraza Torres, "Rapid Prototyping and Manufacturing: A Review of Current Technologies," *Proceedings of the ASME International Mechanical Engineering Congress & Exposition,* 2009.

[14] A. V. Gusarov, I. Yadroitsev, P. Bertrand and I. Smurov, "Model of Radiation and Heat Transfer in Laser-Powder Interaction Zone at Selective Laser Melting," *Journal of Heat Transfer,* vol. 131, no. 7, 2009.

[15] P. Rochus, J.-Y. Plesseria, M. van Elsen, J.-P. Kurth, R. Carrus and T. Dormal, "New applications of rapid prototyping and rapid manufacturing (RP/RM) technologies for space instrumentation," *Acta Astronautica,* vol. 61, no. 1-6, pp. 352-359, 2007.

[16] A. K. Sood, "Study on Parametric Optimization of Fused Deposition Modelling (FDM) Process," *Ph.D. Dissertation, National Institute of Technology,* Rourkela, India, 2011.

[17] B. Evans, "Practical 3D Printers the Science and Art of 3D Printing," *Paul Manning, New York,* 2012.

[18] K. Zeng, "Optimization of support structures for selective laser melting," *Ph.D. Dissertation, University of Louisville,* Kentucky, USA, 2015.

[19] A. Enzi, "Studying Curve Interpolator for CNC System," *Master Thesis, University of Technology,* Baghdad, Iraq, 2008.

[20] G. Jin, W. Li, L. Gao and K. Popplewell, "A hybrid and adaptive tool-path generation approach of rapid prototyping and manufacturing for biomedical models," *Computers in Industry,* vol. 64, no. 3, pp. 336-349, 2013.

[21] J. Zaragoza-Siqueiros and H. I. Medellín-Castillo, "Design For Rapid Prototyping, Manufacturing and Tooling: Guidelines," *Proceedings of the ASME 2014 International Mechanical Engineering Congress and Exposition,* 2014.

[22] C. Zhou, "A Direct Tool Path Planning Algorithm For Line Scanning Based Stereolithography," *Proceedings of the ASME 2014 International Mechanical Engineering Congress and Exposition,* 2014.

[23] L. Lu, J. Fub, A. Nee, E. Kang, T. Miyazawa and C. Cheah, "Origin Of Shrinkage, Distortion, And Fracture Of Photopolymerized Material," *Materials Research Bulletin,* vol. 30, no. 12, pp. 1561-1569, 1995.

[24] D. Ahn, H. Kim and S. Lee, "Fabrication direction optimization to minimize post-machining in layered manufacturing," *International Journal of Machine Tools and Manufacture,* vol. 47, no. 3-4, pp. 593-606, 2007.

[25] Cimetrix, "Surface Roughness," http://leebhardnesstesters.com/reference/surface_roughness.

[26] 3T-RPD-Ltd, "https://www.3trpd.co.uk/wp-content/uploads/2013/03/sls-machine-specifications.pdf," Plastic Additive Manufacturing Machine Specifications. [Online].

[27] Formlabs, "https://formlabs.com/media/upload/Fuse_1_Tech_Specs.pdf," [Online].

[28] P. S. Series, "www.vannasverkstad.se/documents/prox_sls_series.pdf," [Online].

[29] N. Raghunath and P. M. Pandey, "Improving accuracy through shrinkage modelling by using Taguchi method in selective laser sintering," *International Journal of Machine Tools & Manufacture,* vol. 47, no. 6, pp. 985-995, 2007.

[30] Ö. İlkgün, "Effects Of Production Parameters on Porosity and Hole Properties In Laser Sintering Rapid Prototyping Process," *M.Sc. Thesis, Middle East Technical University,* 2005.

[31] A. Chatterjee, S. Kumar, P. Saha, P. Mishra and A. Choudhury, "An experimental design approach to selective laser sintering of low carbon steel," *Journal of Materials Processing Technology,* vol. 136, no. 1–3, pp. 151-157, 2003.

[32] M. Cotteleer, J. Holdowsky, M. Mahto and J. Coykendall, "3D opportunity for aerospace and defense," http://dupress.com/articles/additive-manufacturing-3d-opportunity-in-aerospace/, Deloitte University Press, 2014.

[33] S. Singh, A. Sachdeva and V. S. Sharma, " Investigation of Dimensional Accuracy/Mechanical Properties of Part Produced by Selective Laser Sintering," *International Journal of Applied Science and Engineering ,* vol. 10, pp. 59-68, 2012.

[34] J. P. Kruth, B. Vandenbroucke, J. Van Vaerenbergh and P. Mercelis, "Benchmarking Of Different SLS/SLM Processes As Rapid Manufacturing Techniques," *Conf. Polymers & Moulds Innovations (PMI),* 2005.

[35] R. C. Luo and J. H. Tzou, "Implementation of a New Adaptive Slicing Algorithm for the Rapid Prototyping Manufacturing System," *IEEE/ASME Transactions on Mechatronics,* vol. 9, no. 3, pp. 593-600, 2004.

[36] L. Yang, "Structural Design, Optimization and Application of 3D Re-entrant Auxetic Structures," *Ph.D. dissertation, North Carolina State University,* North Carolina, USA, 2011.

[37] R. Paul and S. Anand, "Process energy analysis and optimization in selective laser sintering," *Journal of Manufacturing Systems,* vol. 31, no. 4, pp. 429-437, 2012.

[38] N. Kumar, H. Kumar and J. S. Khurmi, "Experimental Investigation of process parameters for rapid prototyping technique (Selective Laser Sintering) to enhance the part quality of prototype by Taguchi method," *Procedia Technology,* vol. 23, pp. 352-360, 2016.

[39] H. Chung and S. Das, "Processing and properties of glass bead particulate-filled functionally graded Nylon-11 composites produced by selective laser sintering," *Materials Science and Engineering: A,* vol. 437, no. 2, p. 226–234, 2006.

[40] Z. Khan, B. Prasad and T. Singh, "Machining condition optimization by genetic algorithms and simulated annealing," *Computers & Operations Research,* vol. 24 , no. 7, pp. 647-657, 1997.

[41] A. M. Zain, H. Haron and S. Sharif, "Optimization of process parameters in the abrasive water jet machining using integrated SA–GA," *Applied Soft Computing,* vol. 11, no. 8, pp. 5350-5359, 2011.

[42] A. Afkhamifa, D. Antonelli and P. Chiabert, "Variational analysis for CNC milling process," *Procedia CIRP,* vol. 43, pp. 118-123, 2016.

[43] J. Mao, X. Chen, W. Feng, S. Yuan and R. Du, "A precision CNC turn-mill machining center with gear hobbing capability," *Precision Engineering,* vol. 41, pp. 126-134, 2015.

[44] A. Stwora and G. Skrabalak, "Influence of selected parameters of Selective Laser Sintering process on properties of sintered materials," *Achievements of Materials and Manufacturing Engineering,* vol. 61, no. 2, pp. 375-380, 2013.

[45] K. Shahzad, J. Deckers, S. Boury, B. Neirinck, J.-P. Kruth and J. Vleugels, "Preparation and indirect selective laser sintering of alumina/PA microspheres," *Ceramics International,* vol. 38, no. 2, pp. 1241-1247, 2012.

[46] Y.-A. Song and W. Koenig, "Experimental Study of the Basic Process Mechanism for Direct Selective Laser Sintering of Low-Melting Metallic Powder," *CIRP Annals ,* vol. 46, no. 1, pp. 127-130, 1997.

[47] K. Shahzad, J. Deckers, J.-P. Kruth and J. Vleugels, "Additive manufacturing of alumina parts by indirect selective laser sintering and post processing," *Journal of Materials Processing Technology,* vol. 213, no. 9, pp. 1484-1494, 2013.

[48] A. L. Slaviero, "Implementation Of Carbon Black Nano-Particles Into The Three-Dimensional Printing Binder (Functionally Inks) Aimed At Producing Functionally

Graded Parts," *Ph.D. Dissertation, University of Federal De Santa Catarina Curso De Graduação Em Engenharia De Materials,* 2003.

[49] J. P. Kruth, P. Mercelis, J. Van Vaerenbergh, L. Froyen and M. Rombouts, "Binding Mechanisms in Selective Laser Sintering and Selective Laser Melting," *Rapid Prototyping Journal,* vol. 11, no. 1, pp. 26-36, 2005.

[50] B. Liu, P. Bai and Y. Li, "Post Treatment Process and Selective Laser Sintering Mechanism of Polymer-Coated Mo Powder," *The Open Materials Science Journal,* vol. 5 , pp. 194-198, 2011.

[51] J. Yang, H. Bin, X. Zhang and Z. Liu, "Fractal scanning path generation and control system for selective laser sintering (SLS)," *International Journal of Machine Tools and Manufacture,* vol. 43, no. 3, pp. 293-300, 2003.

[52] Y. Jin, Y. He, G. Fu, A. Zhang and J. Du, "A non-retraction path planning approach for extrusion-based additive manufacturing," *Robotics and Computer–Integrated Manufacturing,* vol. 48, pp. 132-144, 2017.

[53] B. Asiabanpour and B. Khoshnevis, "Machine path generation for the SIS process," *Robotics and Computer-Integrated Manufacturing,* vol. 20, no. 3, pp. 167-175, 2004.

[54] E. C. Santos, M. Shiomi, K. Osakada and T. Laoui, "Rapid manufacturing of metal components by laser forming," *International Journal of Machine Tools and Manufacture,* vol. 46, no. 12-13, pp. 1459-1468, 2006.

[55] J. P. Kruth, G. Levy, F. Klocke and T. Childs, "Consolidation phenomena in laser and powder-bed based layered manufacturing," *CIRP Annals,* vol. 56, no. 2, pp. 730-759, 2007.

[56] K. Murali, A. Chatterjee, P. Saha, R. Palai, S. Kumar, S. Roy, P. Mishra and A. Choudhury, "Direct selective laser sintering of iron–graphite powder mixture," *Journal of Materials Processing Technology,* vol. 136, no. 1-3, pp. 179-185, 2003.

[57] A. Streek, P. Regenfuss and H. Exner, "Fundamentals of Energy Conversion and Dissipation in Powder Layers during Laser Micro Sintering," *Physics Procedia,* vol. 41, pp. 858-869, 2013.

[58] A. Simchi, "Direct laser sintering of metal powders: Mechanism, kinetics, and microstructural features," *Materials Science and Engineering: A,* vol. 428, no. 1-2, pp. 148-158, 2006.

[59] D. Manfredi, F. Calignano, M. Krishnan, R. Canali, E. P. Ambrosio and E. Atzeni, "From Powders to Dense Metal Parts: Characterization of a Commercial AlSiMg Alloy Processed through Direct Metal Laser Sintering," *Materials,* vol. 6, no. 3, pp. 856-869, 2013.

[60] J. P. Davim, *Laser in Manufacturing,* UK & USA: ISTE Ltd and WILY, 2012.

[61] H. Gedda, J. Powell, G. Wahlström, W. Li, H. Engstrom and C. Magnusson, "Energy redistribution during CO2 laser cladding," *Journal of Laser Applications,* vol. 14, no. 2, pp. 78-82, 2002.

[62] H. Carslaw and J. Jaeger, *Conduction of Heat in Solids,* New York: Oxford University, 1959.

[63] K. Ogata, *Modern Control Engineering,* Prentice Hall, 2010.

[64] R. C. Dorf and R. H. Bishop, *Modern Control Systems,* USA: Pearson, 2011.

[65] N. S. Nise, *Control Systems Engineering,* USA: John Wiley & Sons, 2011.

[66] Alm, "Technical Data Sheet of PA650," Advanced Laser Materials, LLC. [Online].

[67] Alm, "PA 650 Material Specifications," RPS. [Online].

[68] P. Plastics, "Thermal Properties of Plastic Materials," [Online].

[69] Autodesk, *Fundamentals of CNC Machining,* USA: Autodesk, 2014.

[70] A. Franco, M. Lanzetta and L. Romoli, "Experimental analysis of selective laser sintering of polyamide powders: an energy perspective," *Journal of Cleaner Production,* vol. 18, no. 16-17, pp. 1722-1730, 2010.

[71] D. C. Montgomery and G. C. Runger, *Applied Statistics and Probability for Engineers,* USA: John Wiley & Sons, 2003.

[72] R. H. Myers, D. C. Montgomery and C. M. Anderson-Cook, *Response Surface Methodology: Process and Product Optimization Using Designed Experiments,* John Wiley & Sons, 2016.

[73] K. Sastry, D. Goldberg and G. Kendall, "Genetic Algorithms," Boston, Springer.

[74] C. W. de Silva, *Mechatronics: A Foundation Course,* UK & USA: CRC Press, 2010.

# 7. APPENDIX A: DATA FOR MATHEMATICAL MODELS

Figure A-1 and Figure A-2 are data used in MATLAB program to get mathematical models for crack width and surface roughness.

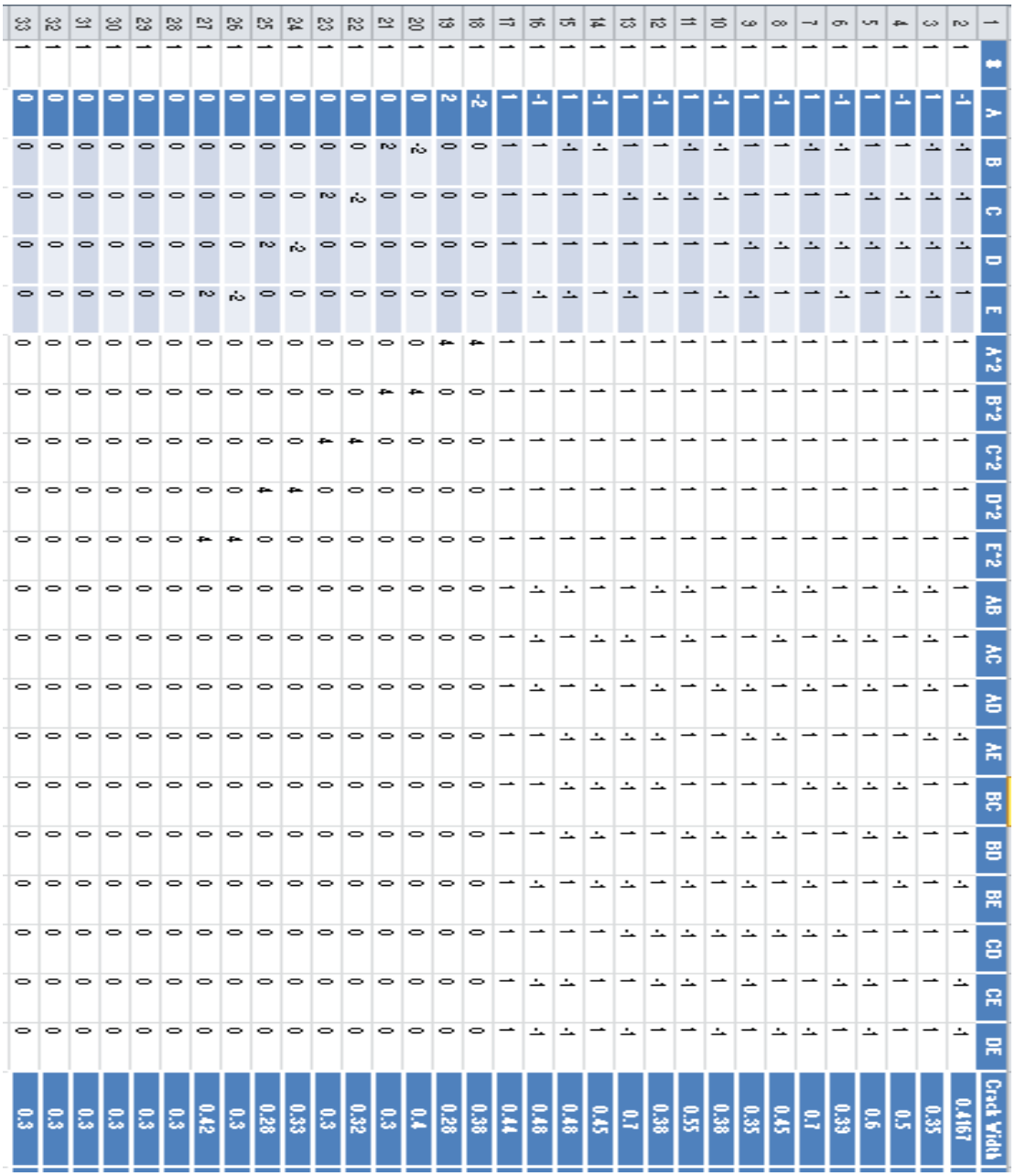

| | # | A | B | C | D | E | A^2 | B^2 | C^2 | D^2 | E^2 | AB | AC | AD | AE | BC | BD | BE | CD | CE | DE | Crack Width |
|---|---|---|---|---|---|---|---|---|---|---|---|---|---|---|---|---|---|---|---|---|---|---|
| 1 | 1 | -1 | -1 | -1 | -1 | 1 | 1 | 1 | 1 | 1 | 1 | 1 | 1 | 1 | -1 | 1 | -1 | -1 | -1 | -1 | 1 | 0.4167 |
| 2 | 1 | -1 | -1 | -1 | -1 | -1 | 1 | 1 | 1 | 1 | 1 | 1 | 1 | 1 | 1 | 1 | 1 | 1 | 1 | 1 | -1 | 0.35 |
| 3 | 1 | -1 | -1 | -1 | 1 | 1 | 1 | 1 | 1 | 1 | 1 | 1 | 1 | -1 | -1 | 1 | 1 | 1 | -1 | -1 | 1 | 0.35 |
| 4 | 1 | -1 | -1 | -1 | 1 | -1 | 1 | 1 | 1 | 1 | 1 | 1 | 1 | -1 | 1 | 1 | -1 | -1 | 1 | 1 | -1 | 0.5 |
| 5 | 1 | 1 | -1 | 1 | -1 | 1 | 1 | 1 | 1 | 1 | 1 | -1 | -1 | 1 | -1 | -1 | 1 | -1 | 1 | -1 | 1 | 0.6 |
| 6 | 1 | -1 | -1 | 1 | -1 | -1 | 1 | 1 | 1 | 1 | 1 | -1 | -1 | 1 | 1 | -1 | 1 | 1 | -1 | 1 | -1 | 0.39 |
| 7 | 1 | 1 | -1 | -1 | 1 | 1 | 1 | 1 | 1 | 1 | 1 | -1 | -1 | -1 | -1 | 1 | 1 | 1 | 1 | -1 | -1 | 0.7 |
| 8 | 1 | -1 | -1 | -1 | 1 | -1 | 1 | 1 | 1 | 1 | 1 | -1 | -1 | -1 | 1 | 1 | -1 | -1 | -1 | 1 | 1 | 0.45 |
| 9 | 1 | 1 | -1 | 1 | -1 | 1 | 1 | 1 | 1 | 1 | 1 | -1 | -1 | 1 | -1 | -1 | 1 | -1 | 1 | -1 | 1 | 0.35 |
| 10 | 1 | -1 | -1 | 1 | -1 | -1 | 1 | 1 | 1 | 1 | 1 | -1 | -1 | 1 | 1 | -1 | 1 | 1 | -1 | 1 | -1 | 0.38 |
| 11 | 1 | 1 | -1 | -1 | 1 | 1 | 1 | 1 | 1 | 1 | 1 | -1 | 1 | -1 | -1 | 1 | 1 | 1 | 1 | -1 | -1 | 0.55 |
| 12 | 1 | -1 | -1 | -1 | 1 | -1 | 1 | 1 | 1 | 1 | 1 | -1 | 1 | -1 | 1 | 1 | -1 | -1 | -1 | 1 | 1 | 0.38 |
| 13 | 1 | 1 | -1 | 1 | -1 | 1 | 1 | 1 | 1 | 1 | 1 | -1 | 1 | 1 | -1 | -1 | 1 | -1 | 1 | -1 | 1 | 0.7 |
| 14 | 1 | -1 | -1 | 1 | -1 | -1 | 1 | 1 | 1 | 1 | 1 | -1 | 1 | 1 | 1 | -1 | 1 | 1 | -1 | 1 | -1 | 0.45 |
| 15 | 1 | 1 | -1 | -1 | 1 | 1 | 1 | 1 | 1 | 1 | 1 | -1 | -1 | -1 | -1 | 1 | 1 | 1 | 1 | -1 | -1 | 0.48 |
| 16 | 1 | -1 | -1 | -1 | 1 | -1 | 1 | 1 | 1 | 1 | 1 | -1 | -1 | -1 | 1 | 1 | -1 | -1 | -1 | 1 | 1 | 0.48 |
| 17 | 1 | 1 | -1 | 1 | -1 | 1 | 1 | 1 | 1 | 1 | 1 | -1 | -1 | 1 | -1 | -1 | 1 | -1 | 1 | -1 | 1 | 0.44 |
| 18 | 1 | -2 | 0 | 0 | 0 | 0 | 4 | 0 | 0 | 0 | 0 | 0 | 0 | 0 | 0 | 0 | 0 | 0 | 0 | 0 | 0 | 0.38 |
| 19 | 1 | 2 | 0 | 0 | 0 | 0 | 4 | 0 | 0 | 0 | 0 | 0 | 0 | 0 | 0 | 0 | 0 | 0 | 0 | 0 | 0 | 0.28 |
| 20 | 1 | 0 | -2 | 0 | 0 | 0 | 0 | 4 | 0 | 0 | 0 | 0 | 0 | 0 | 0 | 0 | 0 | 0 | 0 | 0 | 0 | 0.4 |
| 21 | 1 | 0 | 2 | 0 | 0 | 0 | 0 | 4 | 0 | 0 | 0 | 0 | 0 | 0 | 0 | 0 | 0 | 0 | 0 | 0 | 0 | 0.3 |
| 22 | 1 | 0 | 0 | -2 | 0 | 0 | 0 | 4 | 0 | 0 | 0 | 0 | 0 | 0 | 0 | 0 | 0 | 0 | 0 | 0 | 0 | 0.32 |
| 23 | 1 | 0 | 0 | 2 | 0 | 0 | 0 | 4 | 0 | 0 | 0 | 0 | 0 | 0 | 0 | 0 | 0 | 0 | 0 | 0 | 0 | 0.3 |
| 24 | 1 | 0 | 0 | 0 | -2 | 0 | 0 | 0 | 4 | 0 | 0 | 0 | 0 | 0 | 0 | 0 | 0 | 0 | 0 | 0 | 0 | 0.33 |
| 25 | 1 | 0 | 0 | 0 | 2 | 0 | 0 | 0 | 4 | 0 | 0 | 0 | 0 | 0 | 0 | 0 | 0 | 0 | 0 | 0 | 0 | 0.28 |
| 26 | 1 | 0 | 0 | 0 | 0 | -2 | 0 | 0 | 0 | 4 | 0 | 0 | 0 | 0 | 0 | 0 | 0 | 0 | 0 | 0 | 0 | 0.3 |
| 27 | 1 | 0 | 0 | 0 | 0 | 2 | 0 | 0 | 0 | 4 | 0 | 0 | 0 | 0 | 0 | 0 | 0 | 0 | 0 | 0 | 0 | 0.42 |
| 28 | 1 | 0 | 0 | 0 | 0 | 0 | 0 | 0 | 0 | 0 | 0 | 0 | 0 | 0 | 0 | 0 | 0 | 0 | 0 | 0 | 0 | 0.3 |
| 29 | 1 | 0 | 0 | 0 | 0 | 0 | 0 | 0 | 0 | 0 | 0 | 0 | 0 | 0 | 0 | 0 | 0 | 0 | 0 | 0 | 0 | 0.3 |
| 30 | 1 | 0 | 0 | 0 | 0 | 0 | 0 | 0 | 0 | 0 | 0 | 0 | 0 | 0 | 0 | 0 | 0 | 0 | 0 | 0 | 0 | 0.3 |
| 31 | 1 | 0 | 0 | 0 | 0 | 0 | 0 | 0 | 0 | 0 | 0 | 0 | 0 | 0 | 0 | 0 | 0 | 0 | 0 | 0 | 0 | 0.3 |
| 32 | 1 | 0 | 0 | 0 | 0 | 0 | 0 | 0 | 0 | 0 | 0 | 0 | 0 | 0 | 0 | 0 | 0 | 0 | 0 | 0 | 0 | 0.3 |
| 33 | 1 | 0 | 0 | 0 | 0 | 0 | 0 | 0 | 0 | 0 | 0 | 0 | 0 | 0 | 0 | 0 | 0 | 0 | 0 | 0 | 0 | 0.3 |

Figure A-1. Excel data sheet for crack width that used to double check of mathematical model

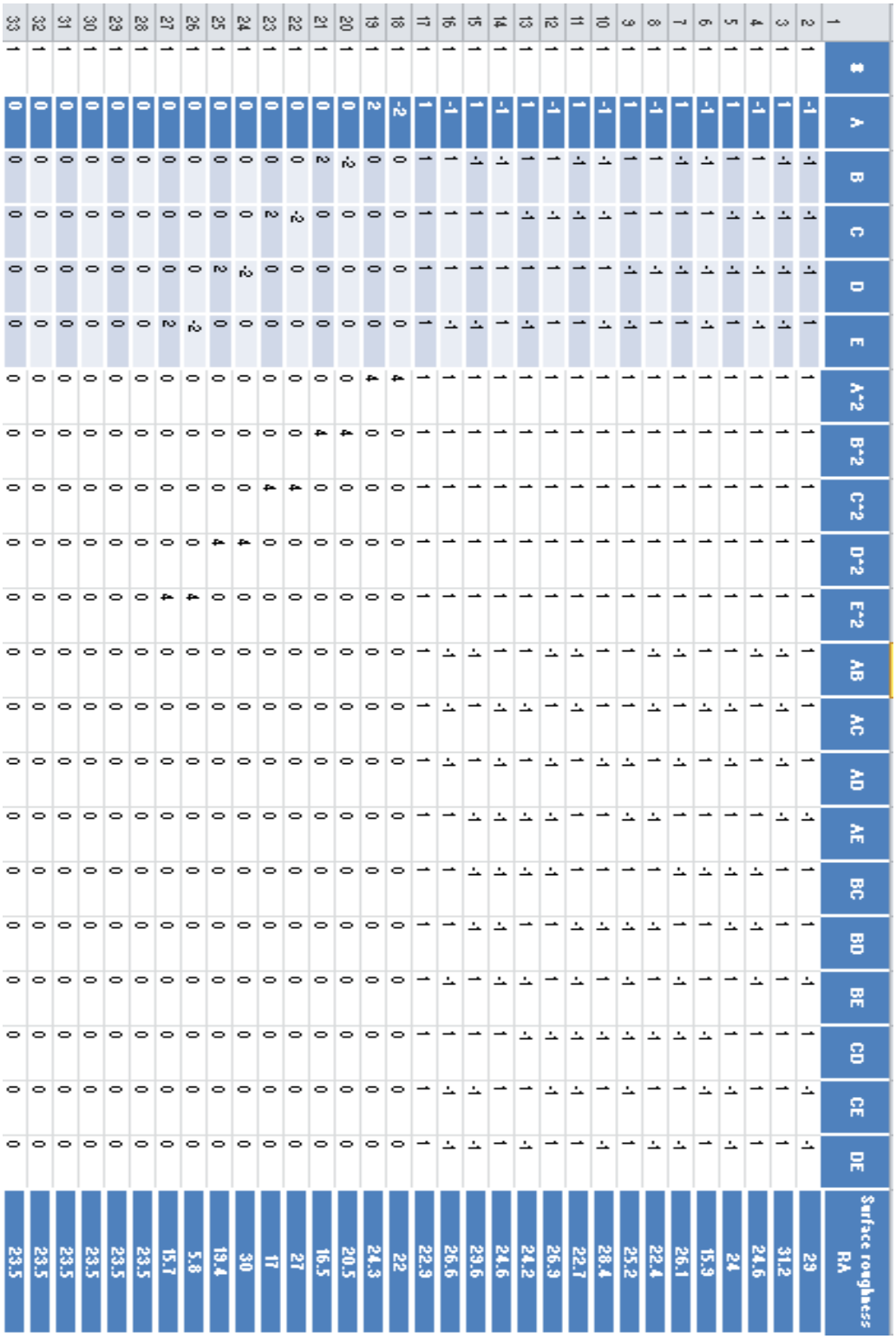

| # | A | B | C | D | E | A^2 | B^2 | C^2 | D^2 | E^2 | AB | AC | AD | AE | BC | BD | BE | CD | CE | DE | Surface roughness RA |
|---|---|---|---|---|---|---|---|---|---|---|---|---|---|---|---|---|---|---|---|---|---|
| 1 | -1 | -1 | -1 | -1 | 1 | 1 | 1 | 1 | 1 | 1 | 1 | 1 | 1 | -1 | 1 | 1 | -1 | 1 | -1 | -1 | 29 |
| 2 | -1 | -1 | -1 | -1 | -1 | 1 | 1 | 1 | 1 | 1 | 1 | 1 | 1 | -1 | 1 | 1 | -1 | 1 | -1 | -1 | 31.2 |
| 3 | -1 | -1 | -1 | -1 | -1 | 1 | 1 | 1 | 1 | 1 | 1 | 1 | 1 | -1 | 1 | 1 | -1 | 1 | -1 | -1 | 24.6 |
| 4 | -1 | -1 | -1 | -1 | -1 | 1 | 1 | 1 | 1 | 1 | 1 | 1 | 1 | -1 | 1 | 1 | -1 | 1 | -1 | -1 | 24 |
| 5 | 1 | 1 | -1 | -1 | 1 | 1 | 1 | 1 | 1 | 1 | 1 | -1 | -1 | -1 | -1 | -1 | -1 | 1 | -1 | -1 | 15.3 |
| 6 | -1 | -1 | 1 | -1 | -1 | 1 | 1 | 1 | 1 | 1 | 1 | -1 | -1 | -1 | -1 | -1 | -1 | 1 | -1 | -1 | 26.1 |
| 7 | 1 | -1 | 1 | -1 | 1 | 1 | 1 | 1 | 1 | 1 | 1 | -1 | -1 | -1 | -1 | -1 | -1 | 1 | -1 | -1 | 22.4 |
| 8 | -1 | 1 | 1 | -1 | 1 | 1 | 1 | 1 | 1 | 1 | 1 | -1 | -1 | -1 | -1 | -1 | -1 | 1 | -1 | -1 | 25.2 |
| 9 | 1 | 1 | -1 | -1 | -1 | 1 | 1 | 1 | 1 | 1 | 1 | -1 | -1 | -1 | -1 | -1 | -1 | 1 | -1 | -1 | 28.4 |
| 10 | -1 | -1 | 1 | -1 | -1 | 1 | 1 | 1 | 1 | 1 | 1 | -1 | -1 | -1 | -1 | -1 | -1 | 1 | -1 | -1 | 22.7 |
| 11 | 1 | -1 | 1 | -1 | 1 | 1 | 1 | 1 | 1 | 1 | 1 | -1 | -1 | -1 | -1 | -1 | -1 | 1 | -1 | -1 | 26.3 |
| 12 | -1 | -1 | -1 | -1 | 1 | 1 | 1 | 1 | 1 | 1 | 1 | -1 | -1 | -1 | -1 | -1 | -1 | 1 | -1 | -1 | 24.2 |
| 13 | 1 | 1 | -1 | -1 | -1 | 1 | 1 | 1 | 1 | 1 | 1 | -1 | -1 | -1 | -1 | -1 | -1 | 1 | -1 | -1 | 24.6 |
| 14 | -1 | -1 | 1 | -1 | -1 | 1 | 1 | 1 | 1 | 1 | 1 | -1 | -1 | -1 | -1 | -1 | -1 | 1 | -1 | -1 | 23.6 |
| 15 | 1 | -1 | 1 | -1 | 1 | 1 | 1 | 1 | 1 | 1 | 1 | -1 | -1 | -1 | -1 | -1 | -1 | 1 | -1 | -1 | 26.6 |
| 16 | -1 | 1 | 1 | -1 | 1 | 1 | 1 | 1 | 1 | 1 | 1 | -1 | -1 | -1 | -1 | -1 | -1 | 1 | -1 | -1 | 22.9 |
| 17 | 1 | 1 | -1 | -1 | -1 | 1 | 1 | 1 | 1 | 1 | 1 | -1 | -1 | -1 | -1 | -1 | -1 | 1 | -1 | -1 | 22 |
| 18 | -2 | 0 | 0 | 0 | 0 | 4 | 0 | 0 | 0 | 0 | 0 | 0 | 0 | 0 | 0 | 0 | 0 | 0 | 0 | 0 | 24.3 |
| 19 | 2 | 0 | 0 | 0 | 0 | 4 | 0 | 0 | 0 | 0 | 0 | 0 | 0 | 0 | 0 | 0 | 0 | 0 | 0 | 0 | 20.5 |
| 20 | 0 | -2 | 0 | 0 | 0 | 4 | 4 | 0 | 0 | 0 | 0 | 0 | 0 | 0 | 0 | 0 | 0 | 0 | 0 | 0 | 16.5 |
| 21 | 0 | 2 | 0 | 0 | 0 | 0 | 4 | 0 | 0 | 0 | 0 | 0 | 0 | 0 | 0 | 0 | 0 | 0 | 0 | 0 | 27 |
| 22 | 0 | 0 | -2 | 0 | 0 | 0 | 4 | 4 | 0 | 0 | 0 | 0 | 0 | 0 | 0 | 0 | 0 | 0 | 0 | 0 | 17 |
| 23 | 0 | 0 | 2 | 0 | 0 | 0 | 0 | 4 | 0 | 0 | 0 | 0 | 0 | 0 | 0 | 0 | 0 | 0 | 0 | 0 | 30 |
| 24 | 0 | 0 | 0 | -2 | 0 | 0 | 0 | 4 | 4 | 0 | 0 | 0 | 0 | 0 | 0 | 0 | 0 | 0 | 0 | 0 | 19.4 |
| 25 | 0 | 0 | 0 | 2 | 0 | 0 | 0 | 0 | 4 | 0 | 0 | 0 | 0 | 0 | 0 | 0 | 0 | 0 | 0 | 0 | 5.8 |
| 26 | 0 | 0 | 0 | 0 | -2 | 0 | 0 | 0 | 0 | 4 | 0 | 0 | 0 | 0 | 0 | 0 | 0 | 0 | 0 | 0 | 15.7 |
| 27 | 0 | 0 | 0 | 0 | 2 | 0 | 0 | 0 | 0 | 4 | 0 | 0 | 0 | 0 | 0 | 0 | 0 | 0 | 0 | 0 | 23.5 |
| 28 | 0 | 0 | 0 | 0 | 0 | 0 | 0 | 0 | 0 | 0 | 0 | 0 | 0 | 0 | 0 | 0 | 0 | 0 | 0 | 0 | 23.5 |
| 29 | 0 | 0 | 0 | 0 | 0 | 0 | 0 | 0 | 0 | 0 | 0 | 0 | 0 | 0 | 0 | 0 | 0 | 0 | 0 | 0 | 23.5 |
| 30 | 0 | 0 | 0 | 0 | 0 | 0 | 0 | 0 | 0 | 0 | 0 | 0 | 0 | 0 | 0 | 0 | 0 | 0 | 0 | 0 | 23.5 |
| 31 | 0 | 0 | 0 | 0 | 0 | 0 | 0 | 0 | 0 | 0 | 0 | 0 | 0 | 0 | 0 | 0 | 0 | 0 | 0 | 0 | 23.5 |
| 32 | 0 | 0 | 0 | 0 | 0 | 0 | 0 | 0 | 0 | 0 | 0 | 0 | 0 | 0 | 0 | 0 | 0 | 0 | 0 | 0 | 23.5 |
| 33 | 0 | 0 | 0 | 0 | 0 | 0 | 0 | 0 | 0 | 0 | 0 | 0 | 0 | 0 | 0 | 0 | 0 | 0 | 0 | 0 | 23.5 |

Figure A-2. Excel data sheet for surface roughness that used to double check of mathematical model